FUNDAMENTAL UNDERSTANDING OF THERMOPHYSICAL PROPERTIES OF MOLTEN SALTS CONTAINING NANOPARTICLES

by

GENG QIAO

A thesis submitted to
The University of Birmingham
for the degree of
DOCTOR OF PHILOSOPHY

School of Chemical Engineering
College of Engineering and Physical Sciences
The University of Birmingham
October 2017

Abstract

Molten salts have been widely used as thermal energy storage (TES) materials as they offer favourable specifications which enable them to be employed in TES applications. Finding a cost-effective method to enhance the energy storage capability of molten salts has caught the attention of many researchers. It was reported that by adding a small amount of nanoparticles, a major enhancement of the specific heat capacity was observed in molten salts. Though different studies argued that the enhancement was not found in other thermal storage materials, the observation of the enhancement was continuously reported. This work studied the thermal properties of molten salt based nanosuspensions synthesized with a novel method modified based on other studies. Molecular dynamics (MD) simulations were employed to study the thermodynamic properties of the nanosuspension systems. By the analysis of the effect on the internal energy of the nanosuspensions I draft general conclusions and explain why molten salt have this specific heat enhancement while other materials (e.g. water) not. I use MD simulation to support, for the first time, a theory that can explain the apparently contradictory behaviour of the experimental data. Moreover, the main impact factor affecting the enhancement was investigated and discussed.

The aim of this study is to provide a conceivable mechanism that can explain the anomalous specific heat capacity enhancement with the support of experimental and MD simulation results. In order to achieve this goal, experiments were conducted to test the thermal properties of the molten salt based nanosuspensions to validate the enhancement and compare the results of nanosuspensions and salts containing micro-particles. Specific latent heat, melting point, thermal conductivity and specific heat capacity of the nanosuspensions were measured to understand the impact of the size and mass fraction of nanoparticles. MD simulations were used to represent the enhancement of specific heat capacity in molten salt based nanosuspensions and study the interactions between salt

and nanoparticle atoms. The mechanism was studied by analysing the interactions and the topographic features of the atoms at the interfacial area of nanoparticle and salt.

The experimental results suggested that the specific heat capacity of the molten salts was affected differently by introducing nanoparticles. The enhancement was not observed in the molten salts containing non-nanoparticles, which proves that the enhancement only occurs in nanosuspensions. Significant impact on specific latent heat and melting point were not observed by the introduction of nanoparticles. In MD simulations a particular salt atom arrangement was observed at the adjacent area of a nanoparticle along with the enhancement of the specific heat capacity. Further simulations validates that the specific heat capacity enhancement only happened when the specific structure appeared. This specific arrangement and the atoms in the area are considered the reason of the enhancement.

ACKNOWLEDGEMENT

I would like to express my great appreciation to Professor Yulong Ding. It is not only for giving me the opportunity and the full support for my PhD study in his group, but also for leading me into the fascinating scientific fields of energy storage. It has been an honour to be his student and have my doctoral training in this lab.

I am very grateful to Dr. Alessio Alexiadis. I have been felt extremely thankful that he always helps and inspires me in my study and cares very much about my work.

With a special mention to Mathieu Lasfagues, Guanghui Leng, Yongliang Li, Helena Navarro, Adriano Sciacovelli, Hui Cao, Chuan Li, Daniel Smith, Lin Cong, Patricia Andreu Cabedo and everyone in BCES. It was fantastic to have the opportunity to undertake the majority of my research with all of you.

I thank my parents for providing me with unfailing support and continuous encouragement throughout my life.

FIGURES

TABLES

CONTENTS

CHAPTER 1

INTRODUCTION

Energy storage provides the ability to store energy at off-peak times when the supply exceeds demands and use it at peak times or whenever it's needed. It eliminates the uncertainty and inconsistency in renewable energy and recovers the waste heat in various industries to solve the space-time mismatch between supply and demand. Energy storage (ES) is accomplished by storing energy in devices or physical media that perform useful operations at a later time. Amongst different TES media, molten salts can be employed in systems with different operating temperatures because they can work from 250 °C to 1680 °C[1]. Molten salts also have excelled in a lot of aspects that they have low vapor pressure, low viscosity, and good chemical stability[2]. At 1% weight concentration, SiO_2 particles were reported for enhancing the specific heat capacity by 14.5% compared with that of the neat chloride salt eutectic[3]. This anomalous enhancement of specific heat capacity has raised the interest level of scientific community for further research. The physical reasons why this happens, however, are not clear yet and data gathered so far show that the classic thermal equilibrium model proposed by Buongiorno [4] cannot be used in this case. Moreover, the results available sometimes clash with each other[5, 6], and do not allow to draw a conclusive theory explaining the specific heat enhancement[3, 7]. None of the existing theories, however, are supported by concrete evidence either experimental or theoretical.

The aim of this work is to investigate the mechanism of the phenomenon with experimental and simulation method and to provide an explanation why molten salts have this specific heat enhancement whereas other materials (e.g. water) do not.

The objectives are as follows:

- To improve an established method to synthesize molten salt based nanosuspensions
- To measure the thermal properties of nanosuspensions and compare them with that of the salts containing non-nanoparticles.
- To study the effect of different nanoparticles on the thermal properties of molten salts

- To study the specific heat capacity enhancement with molecular dynamics (MD) simulations
- To investigate the atom interactions of nanosuspensions in MD simulations
- To study the topographic arrangement and structure observed in both experiments and simulations.
- To explain the mechanism of the enhancement with the support of experimental and simulation data.

In the experiments, the nanoparticles and molten salts ($NaNO_3$, KNO_3 and $LiNO_3$) were mixed in distilled water with the help of a high power ultra sonic probe. The water was evaporated after a stable suspension was formed in the solution and attained the nanosuspensions. Then the thermal properties such as specific heat capacity, latent heat, melting point and thermal conductivity were tested. The properties of nitrate salt based nanosuspensions were measured in MD simulations. The specific heat capacity was calculated based on energy fluctuations from the canonical ensemble[8]. The thermal conductivity was also calculated using RNEMD method[9]. The number density was analysed to study the structural features of the nanosuspensions. Before calculating the properties of salt-nanoparticle system, I calculated the salt and nanoparticle separately. For computing densities of liquid pure salt and nanofluids, simulations were performed in the isothermal-isobaric ensemble using the Nose-Hoover thermostat and barostat[10]. With proper density, simulations were performed using the Nose-Hoover thermostat in the canonical ensemble (NVT)[11].

This thesis consists of 6 chapters. Chapter 2 delivers a summary of the relevant literatures regarding the development of TES technology and the materials employed in TES applications. The importance of enhancing the thermophysical properties and the mechanism of it were also discussed.

Chapter 3 introduces the materials and methods used in this study. It consists of two parts, experiments and simulations. The experimental part includes: the specifica-

tion of the materials used in this study, the nanosuspension synthesis method, and the instruments employed in this research and the principle of them. The simulation part is composed of the model used in the MD simulations, the force field employed, simulation techniques and details of attaining thermophycical data.

Chapter 4 presents the thermophysical property results of salts and salt based materials in experiments.

Chapter 5 provides the details of the MD simulations and investigated the mechanism of the specific heat capacity enhancement observed in both experiments and simulations.

Chapter 6 gives a summary of the conclusions in this study and suggestions for future work.

CHAPTER 2

LITERATURE REVIEW

This chapter contains a summary of the relevant literature regarding the development of TES materials and the methods of enhancing their thermophysical properties. Section 2.1 introduces the state of art of the TES materials, and how the thermophysical properties affect their behaviour. Section 2.2 describes the features of nanomaterials in TES and how this technology is studied. Section 2.3 explains how MD simulations are used in studying nanomaterials and their thermophysical properties, and the development of it.

2.1 Thermal Energy Storage

Thermal energy storage (TES) refers to processes of storing energy in a thermal form and releasing the stored energy in a form depending on the application. Operations of a storage system involves at least three steps: charging, storing, and discharging. Some of the steps may occur simultaneously, and each step can happen more than once in each storage cycle[12]. Though a wide variety of choices of storage media exist depending on operating temperature ranges and applications, several facts are considered as important when designing a TES system[13].

- TES materials should have sufficiently high energy density;
- TES materials should have appropriate thermal conductivity for effective heat transfer;
- TES materials should be physically and chemically stable;
- The materials should have a good reversibility over a large number of cycles;
- TES devices should be safe to operate;
- TES materials should be nontoxic;
- TES materials should be readily available and with a low price.

Mechanistically TES technologies are grouped into three categories of sensible heat storage, latent heat storage and thermochemical heat storage. These are reviewed in the follows sub-sections.

2.1.1 Sensible Heat Storage (SHS)

Sensible heat storage (SHS) refers to the storage of heat in sensible form and is quantified by the heat capacity of storage materials. As a result, materials density and their the specific heats are important factors that determine the energy of SHS. The SHS is

also directly proportional to the operating temperature differences, whereas the rate of charge/discharge of SHS are functions of thermal conductivity and diffusivity of the storage materials and also factors that determine heat transfer in other parts of the system.

Generally, a sensible heat storage system consists of a heat storage medium (SHS material), a container for holding the SHS material and a heat transfer fluid (HTF) (although SHS medium itself acts as the HTF in some cases). The storage medium can be a solid or a liquid. Solid media (e.g. bricks, rocks etc.) are usually used in the form of a packed bed which requires also a HTF to exchange heat with. In such a system, compatibility of HTF and TES materials needs to be considered. Liquid media (such as water, molten salts and oils) in a vessel often have natural thermal stratification due to density difference between hot and cold parts of the media. This liquid media also act as a HTF in many cases.

The stored heat in SHS materials can be calculated as:

$$Q = \int_{T_1}^{T_2} mC_p dT \tag{2.1}$$

where Q is heat stored in a SHS material (J), T_1 is initial temperature of the material (K), T_2 is final temperature of the material (K), m is mass of SHS material (kg), C_P is specific heat capacity (J kg^{-1} K^{-1}) and T is temperature (K).

Solid SHS Materials

Solid SHS materials like concrete, metal, or ceramic have been used as TES materials. These materials are normally chemically stable with no freezing or boiling problems[12, 14]. They also have the advantage of no leakage problems, which increases their reliability[12]. Lovegrove, Luzzi, and Kreetz [15] and Tamme [16] found that concrete and castable ceramics present good characteristics in heat storage. The castable ceramic developed by the German Aerospace Center (DLR) by Tamme [16] is based on a binder containing Al_2O_3. Tamme, Steinmann, and Laing [17] also developed a high tempera-

Table 2.1: Properties of thermal energy storage materials developed at DLR (Stuttgart Germany)

Material	Castable ceramic	Concrete
Density [kg m^{-3}]	3500	2750
Specific heat capacity at 350 °C [J kg^{-1} K^{-1}]	866	916
Thermal conductivity at 350 °C [W m^{-1} K^{-1}]	1.35	1.0
Coeff. of thermal expansion at 350 °C [$10^{-6}K^{-1}$]	11.8	9.3
Material strength	Low	Medium
Crack initiation	Hardly no cracks	Several cracks

ture concrete which has comparable thermal properties to castable ceramic with a much lower price. The properties of castable ceramic and high temperature concrete are shown in Table 2.1. Both materials were tested on the Plataforma Solar de Almeria (PSA) in Spain and are integrated in a parabolic trough test loop and found suitable for solid media sensible heat storage. Stahl [18] conducted a detailed study on the thermal properties of solid thermal storage materials for buildings at ambient temperature. Based on the results, brick, marble, steel slabs and asphalt sheets have good potential for building energy saving. Inorganic salts and metals are mainly for high temperature (120-1400 °C) thermal energy storage applications[19, 20].

Navarro et al. [21] studied the suitability of two slags from the mining and metallurgical industry as TES materials. The thermal properties of the slags and composite materials formulation with the slags and cements were studied as shown in Table 2.2.

Solid materials possess advantages described as above but also have some problems that need to be resolved. While the heat transport fluid flows through pipes to transfer heat from the solid material. If the thermal expansion coefficient of the pipe and storage material is different, separation might occur. The separation leads to poor heat transfer characteristics and might potentially damage the system.

Liquid SHS Materials

Liquid TES materials have also been widely used due to their availability and economic competitiveness. The well-known "water" is one of the best sensible heat storage media at temperatures below ∼100 °C[22, 23], for its high specific heat capacity. It is affordable

Table 2.2: Properties of mining and metallurgical by-products

Sample	Thermal conductivity ($W\ m^{-1}\ K^{-1}$)	Specific heat capacity ($kJ\ kg^{-1}\ K^{-1}$) 100	300	500	Density ($kg\ m^{-3}$)	Media cost (US$ kg^{-1})
Slag P	0.8	0.571	0.683	1.188	3600	0.196
Slag B	1.1	0.648	0.633	0.999	3700	0.196
Phosphate cement/Slag B	1.6	0.703	0.861	1.015	2828	0.196
Phosphate cement/Slag P	1.5	0.655	0.780	1.23	2804	0.196
Aluminous cement/Slag B (25:75)	1.4	0.640	0.730	0.923	3030	0.196
Aluminous cement/Slag P (25:75)	1.4	0.60	0.752	0.985	2947	0.196
Portland cement/Slag P (25:75)	1.4	0.623	0.619	0.971	2785	0.157
Portland cement/Slag B (25:75)	1.8	0.681	0.582	0.829	2859	0.157

and widely available. The most common use of SHS in water is for hot water and space heating [14]. Salty water draws plenty of research efforts as well, for which sodiums and magnesium chlorides are commonly used salts[24]. In the intermediate and high temperature ranges, many fluids with low vapour pressures than water at high temperatures have been tested. Oils are limited to temperatures below $\sim$400 °C due to safety and stability considerations. As a commercial oil product used widely in concentrated solar power generation, Therminal VP-1 has attracted significant attention for its low freezing point and acceptable thermal properties[25]. Mixtures of inorganic molten salts particularly eutectic salts are mostly considered candidates for high temperature applications. Commercial products such as Solar Salt (60% $NaNO_3$, 40% KNO_3), Hitec (7% $NaNO_3$, 53% KNO_3,40% $NaNO_2$), and Hitec XL (48% $Ca(NO_3)_2$, 7% $NaNO_3$,45% KNO_3) are the leading candidates in industries and applications. Dunn, Hearps, and Wright [26] analysed the Solar Two project in the U.S.A. and implied advantages of the molten-salt power tower storage system including elimination of heat transfer oil and associated heat exchangers, a lower salt requirement, higher steam cycle efficiency, and better compatibility with air cooling, etc. These salts are already used in the solar power plants, and chemical and

metallurgical industries. Sodium hydroxide which has a melting point of ∼320 °C and can be used for temperatures up to ∼800 °C. However at a temperature of this level, it is difficult and expensive to contain. Corrosion is also a big issue. Liquid metals are also possible sensible heat storage media. They have good thermal conductivity but a low specific heat capacity, and a high potential for reacting with container walls.

2.1.2 Latent Heat Storage (LHS)

Latent heat storage makes use of latent heat during phase change and therefore normally has a higher energy density compared with SHS for a given temperature range. LHS materials are therefore also called phase change materials (PCMs)[27–30]. Figure 2.1 shows a comparison of heat stored as a function of temperature between SHS and LHS processes. As can be seen, the temperature is constant during phase change, which helps stabilise the operation. In general, LHS materials absorb 5-14 times more heat per unit volume than SHS materials due to the phase change[31].

Heat stored in a PCM can be calculated as:

$$Q = m(\int_{T_1}^{T_m} C_{p,phase1} dT + \Delta H + \int_{T_m}^{T_2} C_{p,phase2} dT) \tag{2.2}$$

where

Q = heat stored in the PCM (J),

T_1 and T_2 = initial and final temperature, respectively(K),

T_m = phase change temperature(K),

ΔH = specific latent heat (J g^{-1}),

m = mass of the PCM (g),

$C_{p,phase1}$ and $C_{p,phase2}$ = specific heat capacity of the PCM at phase 1 and phase 2, respectively (J g^{-1} K^{-1}).

LHS can be achieved through liquid-solid, liquid-gas or solid-gas phase change. Due to the large volume change, gas-liquid and gas-solid have not been applied for TES so

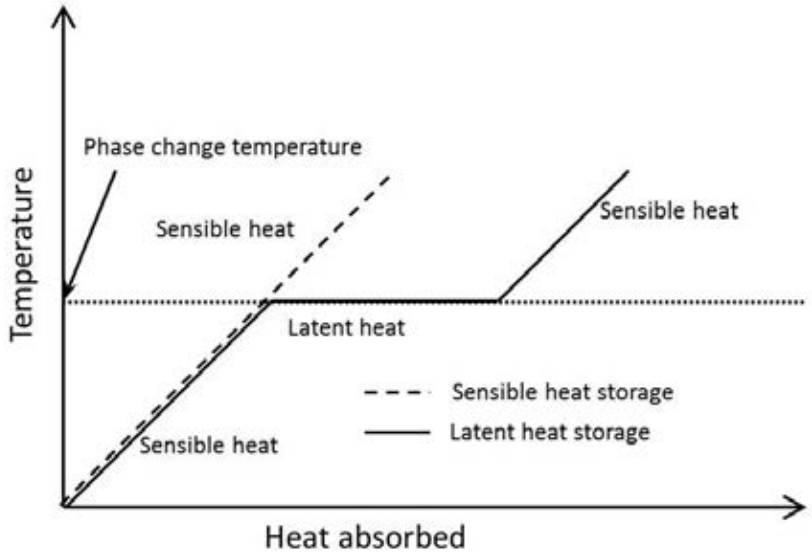

Figure 2.1: Comparison of sensible heat and latent heat storage

far although liquid air (also called cryogenic) energy storage can be arguably to be a special type of gas-liquid phase change technology. Although solid-solid phase change has been proposed[32], solid-liquid phase change is the only one applied industrially for TES. As a result, the following discussion focuses on solid-liquid phase change. Examples of the solid-liquid PCMs include salts, paraffin, fatty acids, and metal alloys, etc. These materials have the level of latent heat needed for competitive performance-price ratio and hence find lots of potential applications. In addition, a PCM should also possess the following thermophysical, kinetic and chemical properties[30, 33, 34]:

- The phase change temperature should match the operation temperature of the relevant applications;
- The phase change process should be congruent to avoid phase separation;
- The phase change process should be reversible;
- Zero or little volume changes occurs during phase change;
- Long cycle life is needed.

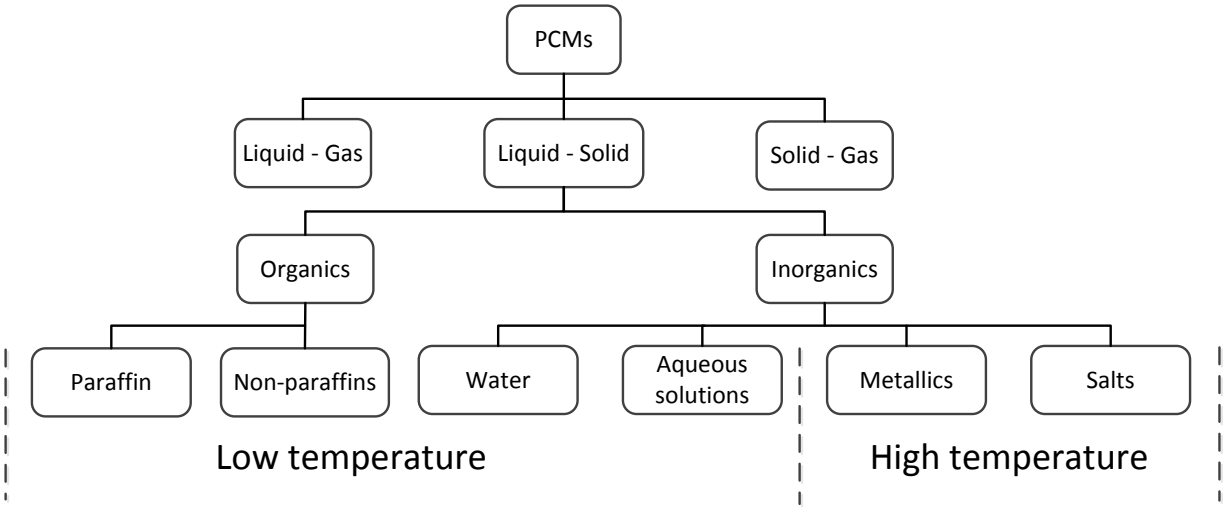

Figure 2.2: Classification of PCMs

There are a large number of substances that can be used as PCMs. These materials can be grouped into two categories of organic and inorganic PCMs as shown in Figure 2.2. Paraffins, fatty acids, and salts can be further divided into compounds and eutectics. A compound material only contains one chemical species, where an eutectic consists of two or more components. Eutectics which melt and freeze congruently at the phase change temperature. Organic PCMs, including water, and aqueous solutions, are generally used for low temperature applications such as Eco-buildings and cold storage. Liquid metals and salts, on the other hand, are used for high temperature applications like concentrated solar thermal power plants and ironmaking processes.

Organic PCMs

Organic materials are divided into paraffins and non-paraffins.

Paraffin consists of a mixture of mostly straight chain n-alkanes. Generally, the melting point, molar specific heat capacity and latent heat of paraffin increase along with the length of the chain. The melting point and latent heat of common alkanes versus increasing number of carbon atoms in their structure are listed in Table 2.3. Since paraffin possesses considerable latent heat that satisfies TES applications and the availability in

a large temperature range, they are applied in industry to an appreciable extent. Besides, paraffin is reliable, chemically inert, non-corrosive, cost effective, which also makes it more favorable. Paraffin waxes are one of the most commonly used commercial organic PCMs in TES systems. However, due to cost consideration, generally only technical grade paraffins are used as PCMs[35]. Table 2.4 shows the thermal properties of some technical grade paraffins which are not refined oil[36] that were developed in Germany or the USA.

A wide selection of organic substances such as esters, alcohols, glycols, and fatty acids comprise non-paraffin organic PCMs. Comparing to paraffin, they have various properties unlike the paraffin group which have similar properties. A further subgroup of materials called fatty acid in the non-paraffin organics are identified as a class of excellent PCMs due to the following properties such as high latent heat, adjustable phase change temperature, negligible super-cooling, non-toxic, no phase segregation and availability[43–45]. Though the non-paraffin organics possess some desirable characteristics they are considered much more expensive than paraffins, which confines the scope of application. The properties of some non paraffins are shown in Table 2.5.

Inorganic PCMs

Inorganic materials are further divided as water, aqueous solutions, salts, and metallics. Comparing to organic PCMs, inorganic PCMs can be selected in a much wider temperature range.

Water is one of the best sensible heat storage materials due to its great specific heat capacity. It can also be used as a PCM for the latent heat it has. Since the required melting point in applications varies, by adding impurities aqueous solutions are developed to adjust the melting point to suit the operation status. Kumano et al. [49] mixed water with propylene glycol (PG), ethylene glycol (EG), ethanol (ET), NaCl, and $NaNO_3$ as aqueous solutions whose thermal properties were measured. Both the melting point and latent heat decrease with the fraction of solutes.

Despite the low specific heat capacity and corrosion activity, metal alloys are still

Table 2.3: Thermodynamic properties of n-alkanes[37–42]

n-Alkanes	No. of C Atoms	Melting Point (°C)	Latent Heat (kJ kg^{-1})	Density at 20 °C (kg m^{-3})	Specific Heat Capacity (kJ kg^{-1} K^{-1}) Solid	Liquid	Boiling Point (°C)
Methane	1	-182.47	58	0.658	-	-	-156.55
Ethane	2	-182.77	95	0.124	-	-	-88.55
Propane	3	-187.68	80	1.834	-	-	-42.05
Butane	4	-138.36	105	2.455	-	-	-0.45
Pentane	5	-129.7	117	621	-	2.32	35.85
Hexane	6	-95.32	152	655	-	2.27	68.75
Heptane	7	-90.6	141	649	-	2.25	98.45
Octane	8	-56.78	181	699	-	2.23	125.65
Nonane	9	-143.5	170	714	-	2.22	150.85
Decane	10	-29.65	202	726	-	2.21	174.15
Undecane	11	-25.6	177	737	-	2.21	195.95
Dodecane	12	-9.6	216	745	-	2.21	216.35
Tridecane	13	-5.4	196	753	-	2.21	235.45
Tetradecane	14	5.8	227	759	-	2.21	253.55
Pentadecane	15	9.9	207	765	-	2.22	270.65
Hexadecane	16	18.1	236	770	-	2.22	286.85
Heptadecane	17	21.9	214	775	-	2.23	302.05
Octadecane	18	28.1	244	779	1.91	2.22	316.35
Nonadecane	19	32	222	782	1.92	2.31	329.95
Eicosane	20	36.6	248	785	1.93	2.33	343.85
Heneicosane	21	40.2	213	788	1.93	2.36	356.55
Docosane	22	44	252	791	1.93	2.38	368.65
Tricosane	23	47.5	234	793	1.93	2.38	380.25
Tetracosane	24	50.6	255	796	1.93	2.38	391.35
Pentacosane	25	53.5	238	798	1.90	2.32	401.95
Hexacosane	26	56.3	250	800	1.85	2.38	412.25
Heptacosane	27	58.8	235	802	1.92	2.44	422.15
Octacosane	28	61.2	254	803	1.91	2.38	431.65
Nonacosane	29	63.2	239	805	1.90	2.45	440.85
Triacontane	30	65.4	252	806	1.90	2.46	449.75
Hentriacontane	31	67.9	242	808	1.89	2.46	458.05
Dotriacontane	32	69.7	266	809	1.93	2.43	467.05
Tritriacontane	33	71.4	256	810	1.88	2.40	475.05
Tetratriacontane	34	73.1	268	811	1.86	2.40	482.05
Pentatriacontane	35	74.7	257	812	1.86	2.46	490.05
Hexatriacontane	36	76.2	269	814	1.85	2.38	497.05
Heptatriacontane	37	77.7	259	815	1.84	2.45	504.05
Octatriacontane	38	79	271	815	1.84	2.44	511.05
Nonatriacontane	39	80.3	271	816	1.83	2.45	518.05
Tetracontane	40	81.5	272	817	1.82	2.51	522.05
Dotetracontane	42	84.17	273	817	1.80	2.43	531.05
Tritetracontane	43	85.5	273	819	1.80	2.43	540.05
Tetratetracontane	44	86.4	274	820	1.78	2.42	545.05
Hextetracontane	46	88.3	276	822	1.76	2.40	556.05
Octatetracontane	48	90.3	276	823	1.75	2.37	565.05
Pentacontane	50	92	276	825	1.73	2.37	575.05
Hexacontane	60	99	279	831	1.64	2.28	615.05
Heptacontane	70	105.5	281	836	1.55	2.17	646.05
Hectane	100	115.25	285	846	1.33	1.85	662.05

Table 2.4: Properties of technical grade paraffins

Paraffin	Melting point (°C)	Latent heat (kJ kg^{-1})
6106 (Germany)	42-44	189
P116 (USA)	45-48	210
5838 (Germany)	48-50	189
6035 (Germany)	58-60	189
6403 (Germany)	62-64	189
6499 (Germany)	66-68	189

Table 2.5: Properties of non-paraffin organic PCMs[30, 46–48]

Compound	Melting point °C	Latent heat (kJ kg^{-1})	Thermal conductivity (W m^{-1} K^{-1})	Density (kg m^{-3})
Propyl palmiate	10	186	-	-
Isopropyl palmiate	11	95-100	-	-
Isopropyl stearate	14-18	140-142	-	-
Caprylic acid	16	148.5	0.149 (liquid, 38.6 °C)	901 (liquid, 30 °C)
Butyl stearate	19	140	-	-
Dimethyl sabacate	21	120-135	-	-
Vinyl stearate	27-29	122	-	-
Capric acid	32	152.7	0.153 (liquid, 38.5 °C)	878 (liquid, 45 °C)
Methyl-12 hydroxy-stearate	42-43	120-126	-	-
Lauric acid	42-44	178	0.147(liquid, 50 °C)	862 (liquid,60 °C)
Myristic acid	49-51	204.5	-	861 (liquid, 55 °C)
Palmitic acid	64	185.4	0.162 (liquid, 68.4 °C)	850 (liquid, 65 °C)
Stearic acid	69	202.5	0.172 (liquid, 70 °C)	848 (liquid, 70 °C)
Polyglycol E400	8	99.6	0.187 (liquid, 25 °C)	1125 (liquid, 25 °C)
Dimethyl-sulfoxide (DMS)	16.5	85.7	-	1009 (solid and liquid)
Polyglycol E600	22	127.2	0.189 (liquid, 38.6 °C)	1126 (liquid, 25 °C)
Polyglycol E6000	66	190	-	1085 (liquid, 70 °C)
Naphthalene	80	147.7	0.132 (liquid, 83.8 °C)	976 (liquid, 84 °C)
Erythritol	118	339.8	0.326 (liquid, 140 °C)	1300 (liquid, 140 °C)
HDPE	100-150	200	-	-
Trans-1,4-polybutadiene (TPB)	145	144	-	-

competent candidates as PCMs in high temperature thermal energy storage applications, particularly when compactness in volume and high thermal conductivity are priorities. Birchenall and Telkes [50] analysed the feasibility of storing thermal energy in metals based PCMs. On the base of the study, a subsequent piece of work was done on the thermal properties of eutectic alloys using a differential-scanning calorimeter (DSC) and differential-thermal analysis (DTA) with a graphite crucible for preventing corrosion (Birchenall and Riechman [51]).

For applications at a temperature range from 250 °C to 1680 °C, inorganic salts are regarded as suitable options[1]. The latent heat of these salts varies from ∼68 to ∼1041 kJ kg^{-1}. Trunin [52] summarized the melting point and heat of fusion data for some salts; see Table 2.6 and Table 2.7.

Salts have been shown to have the following advantages as heat storage media.

- High temperature stability allowing a high energy density; enhancing the thermodynamic cycle efficiency; and as a result lowering the cost of electricity;
- Naturally abundant and low cost compared with the conventional organic TES materials;
- Non-toxic and environmentally friendly[53, 54];
- Very low vapour pressure[2] even at high temperatures allowing storage devices operated of low pressure and hence reduced capital and maintenance costs.

Takahashi, Sakamoto, and Kamimoto [55] measured enthalpies of fusion together with heat capacities in both solid and liquid phases of $LiNO_3$, $NaNO_3$ and KNO_3 with a DSC. Marianowski and Maru [56] and Maru et al. [57] studied and reported various aspects of molten salts at temperatures above ∼450 °C. Bauer et al. [58] investigated thermal properties of $NaNO_3$ with a heat flux type of DSC (Netzsch DSC404) in an Argon flow (100 ml min^{-1}) with a heating rate of 10 K min^{-1}. They found that the specific heat capacity of liquid $NaNO_3$ was ∼1.655J g^{-1} K^{-1} at ∼306-450 °C, and KNO_3 was more

Table 2.6: Melting temperatures of some common salts (°C)[52]

Metal	Fluioride	Chloride	Bromide	Iodide	Sulphate	Nitrate	Carbonate	Chromate	Molybdate	Tungstate
Lithium	849	610	550	469	858	253	732	485	703	740
Sodium	996	801	742	661	884	307	858	794	688	696
Potassium	858	771	734	681	1069	335	900	973	926	923
Rubidium	795	723	692	556	1070	312	873	994	955	952
Cesium	703	645	638	632	1015	409	793	975	935	953
Magnesium	1263	714	711	633	1137	426	990		1230	826
Calsium	1418	772	742	783	1460	560	1330	1000	1449	1580
Strontium	1477	875	657	538	1605	645	1490	1283	1457	1535
Barium	1368	961	857	711	1680	594	1555	1444	1458	1475

Table 2.7: Heat of fusion of some common salts (J g^{-1})[52]

Metal	Fluioride	Chloride	Bromide	Iodide	Sulphate	Nitrate	Carbonate	Chromate	Molybdate	Tungstate
Lithium	1041	416	203		84	373	509	168	281	157
Sodium	794	482	255	158	165	177	165	146	109	107
Potassium	507	353	215	145	212	88	202	41	163	86
Rubidium	248	197	141	104	145	31			140	78
Cesium	143	121	111	96	101	71		94	75	63
Magnesium	938	454	214	93	122		698			
Calcium	381	253	145	142	203	145				
Strontium	226	103	41	57	196	231				
Barium	105	76	108	68	175	209				

chemically stable than $NaNO_3$. However, a considerable amount of nitrite was found in $NaNO_3$ melts at temperature range of ∼450-700 °C, leading to a decrease in the melting point. Hence, the maximum temperature of $NaNO_3$ should be limited to temperatures below ∼450 °C in practical applications.

Pure salts have a fixed melting point. Applications often need materials with melting points that cannot be too expensive to meet with these pure salts. As a result, salt mixtures, particularly, eutectic salt mixtures have been developed, which possess the virtues such as better chemical stability at high temperature[59] and tuneable phase change temperatures. There have been publications studying thermophysical properties of eutectic salt mixtures dating back many decades. Marianowski and Maru [56] and Maru et al. [57] published the properties of various eutectic salt mixtures in the temperature range of ∼455-535 °C. A number of these inorganic salts have been examined for potential use as phase change materials. For example, Birchenall and Riechman [51], as mentioned earlier, summarized thermal properties of some salts and compared them with metal alloy based thermal storage materials.

There have been various studies on binary and ternary fluoride and chloride based

Table 2.8: Fluoride eutectic compositions[56, 60–73]

Salt composition (mol.%)	T_m °C	Latent heat (kJ kg^{-1})
NaF(5)-87$NaNO_3$3-8NaCl	288	224
LiF(7.0)-41.5LiCl-16.4$LiVO_3$-35.1Li_2CrO_4	340	177
LiF(16.2)-42.0LiCl-17.4$LiVO_3$-11.6Li_2SO_4-11.6Li_2SO_4	363	284
LiF(16.2-51.5LiCl-16.2Li_2SO_4-16.2Li_2MoO_4	402	291
LiF(45.7)-1.8BaF_2-41.2KF-11.3NaF	438	332
LiF(42.5-45.5)-(41.0-43.0)KF-(10.7-11.5)NaF-(2.8-3.0)KCl	440-448	682-692
LiF(27.1)-11.9NaF-55.1KF-5.9MgF_2[a]	449	699
LiF(29.2)-11.7NaF-59.1KF[a]	454	414
LiF(46.5)-42KF-11.5NaF	454	325
LiF(33)-67KF[a]	493	458
LiF(35.2)-38.3NaF-26.5CaF_2	615	636
LiF(52)-35NaF-13CaF_2	615	640
LiF(46)-44NaF-10MgF_2	432	858
LiF(60)-40NaF	652	816
LiF(62)-19NaF-19MgF_2	693	690
NaF(65)-23CaF_2-12MgF_2	743	568
LiF(70)-30MgF_2	728	520
LiF(67)-33MgF_2	746	947
LiF(81.5)-19.5CaF_2	769	820
KF(85)-15CaF_2	780	440
KF(85)-15MgF_2	790	520
NaF(64)-20MgF_2-15KF	804	650
NaF(62.5)-22.5MgF_2-15KF	809	543
NaF(68)-32CaF_2	810	600
NaF(75)-25MgF_2	832	627

[a] wt.%

systems stimulated by their high heat of fusion. Tables 2.8 and Table 2.9 shows the results obtained by various researchers. Heidenreich and Parekh [67] studied the use of eutectic salts in an organic Rankine cycle (ORC) solar dynamic power system as thermal energy storage (TES) materials. They studied the thermal properties of these eutectic salts and evaluated the performance of TES units containing different salts. Gubanova, Kondratyuk, and Garkushin [60] analyzed phase diagrams and thermal properties of a series of fluoride eutectic salts. Eichelberger and Gillman [66] discussed the practicality of the use of fluoride as TES materials. In their research, the thermophysical properties, costs, phase behaviour, toxicity, stability, volume changes, corrosion and container materials were examined for 23 fluoride salts, with melting points ranging between ∼400 and ∼1000 °C. Phillips and Stearns [63] discussed the viability of the use of a alkali metal/alkali salt slurry for TES applications. Fluoride eutectic salts were considered as

TES material. They found the use of the fluoride salts were feasible, taking into account the reduction of corrosive effects. Misra and Whittenberger [72] characterized multiple fluoride salt mixtures as phase change TES materials, and obtained their phase diagrams, and the heat of fusion and extent of undercooling of the materials. They also estimated the corrosivity of molten fluoride salts in the absence of water. With a trace amount of water (e.g. 10 mol ppm) fluoride showed a high corrosivity against common alloys.

Table 2.9: Chloride based eutectic salts[56, 57, 63, 64, 74, 75]

Salt composition (mol.%)	T_m °C	Latent heat (kJ kg^{-1})
LiCl(54.2)-6.4$BaCl_2$-39.4KCl	320	170
LiCl(58)-42KCl	348	170
KCl(28.7)-45$MnCl_2$-26.3NaCl	350	215
KCl(45.5)-34.5$MnCl_2$-20NaCl	390	230
KCl(37.7)-37.3$MnCl_2$-25NaC	400	235
NaCl(22.5-26.5)-(18.5-22.5)KCl-(57.0-53.0)$MgCl_2$[a]	385-393	405-410
KCl(21.6)-45.4$MgCl_2$-33NaCl	385	284
KCl(20)-50$MgCl_2$-30NaCl	396	291
KCl(22)-51$MgCl_2$-27NaCl	396	290
NaCl(56.2)-43.8$MgCl_2$	442	325
NaCl(56)-44$MgCl_2$	430	320
KCl(54)-46$ZnCl_2$[a]	432	218
KCl(61)-39$MgCl_2$[a]	435	351
KCl(36)-64$MnCl_2$	448	236
KCl(36)-64$MgCl_(2)$[a]	470	388
NaCl(60)-40$MgCl_2$	450	328
NaCl(48)-52$MgCl_2$[a]	450	430
$CaCl_2$(50)-7.25KCl-42.75NaCl	465	245
$BaCl_2$(8.7)-52.3KCl-18.2$MgCl_2$20.7NaCl	475	248
$BaCl_2$(13.1)-16.9$CaCl_2$-47.3KCL-22.7NaCl	478	208
$BaCl_2$(9.3)-22.2$CaCl_2$-42.7KCl-25.8NaCl	479	217
$CaCl_2$(52.8)-47.2NaCl	500	239
$CaCl_2$(67)-33NaCl[a]	500	281
KCl(25)-27$CaCl_2$-48$MgCl_2$	487	342
$CaCl_2$(66)-5KCl-29NaCl[a]	504	279
KCl(24)-47$BaCl_2$-29$CaCl_2$[a]	551	219
KCl(28)-19NaCl-53$BaCl_2$[a]	542	221
NaCl(52)-48$NiCl_2$	573	558

[a] wt.%

The use of fluorides and chlorides so far is limited because of their strong corrosivity, whereas nitrates, carbonates and other less corrosive salts are mainly used for TES applications. Table 2.10 and 2.11 give a list of some common eutectic mixtures. Among these commonly used salts, nitrate salt mixtures have been regarded as preferred option for solar power plants because they offer a good combination of properties such as specific heat

Table 2.10: Composition and properties of some eutectic nitrate salts[76, 77, 79]

Salt composition (mol.%)	T_m °C	Latent heat (kJ kg^{-1})
$LiNO_3$(29)-17$NaNO_3$-49.4KNO_3-4.6$Sr(NO_3)_2$[a]		
$LiNO_3$(33)-67KNO_3[a]	133	170
$LiNO_3$(31.7)-68.3KNO_3[a]	135	136
KNO_3(53)-40$NaNO_2$-7$NaNO_3$[a]	142	80
$LiNO_3$(57)-43$NaNO_3$[a]	193	248
$LiNO_3$(49)-51$NaNO_3$[a]	194	265
KNO_3(54)-46$NaNO_3$[a]	222	100
$NaNO_3$(54)-46KNO_3	222	117
$LiNO_3$(97.4)-2.6$Ba(NO_3)_2$	253	368

[a] wt.%

capacity (∼1.5 kJ kg^{-1} K^{-1}), chemical reactivity (low), vapour pressure (<0.01 Pa) and cost (<£500/ton). Gasanaliev and Gamataeva [76] used a term called heat-accumulating material (HAM) to refer to TES materials in their study. They examined various properties of the eutectic salts and developed a methodology for choosing TES materials for multi-component systems. The study suggests that in order to select energetically and economically advantageous HAMs, one has to know their thermal characteristics, especially the heat-accumulating properties. Venkatesetty and LeFrois [77] investigated experimentally 9 salt eutectic salt mixtures as PCMs for a TES unit which was integrated with a central receiver of the solar thermal power pilot plant and suggested differential-scanning calorimetry as a reliable method to obtain the thermal capacity properties. Petri, Ong, and Martin [78] discussed the use of eutectic salts based PCMs in a TES unit and showed that molten salt based latent heat storage systems could offer potentially significant performance and cost advantages.

However, no single material can have all the required properties as a PCM for all TES systems. As a result, many methods have been studied to make up shortfall of these materials [1]. For example metallic fins have been used to enhance heat transfer of PCM with a low thermal conductivity, and nucleation agents have used to reduce supercooling of PCMs [80–82].

Table 2.11: Composition and properties of some eutectic carbonate salts[56, 57, 67, 78]

Salt composition (mol.%)	T_m °C	Latent heat (kJ kg^{-1})
Li_2CO_3(32.1)-34.5K_2CO_3-33.4Na_2CO_3	397	276
Li_2CO_3(47)-53K_2CO_3	488	342
Li_2CO_3(44)-56Na_2CO_3	496	370
Li_2CO_3(28)-72K_2CO_3	498	263
Li_2CO_3(44.3)-55.7Na_2CO_3	498	393
Li_2CO_3(35)-65K_2CO_3	505	344
Li_2CO_3(32)-35K_2CO_3-33Na_2CO_3	397	276
Li_2CO_3(20)-60Na_2CO_3-20K_2CO_3	550	283
Li_2CO_3(22)-16Na_2CO_3-62K_2CO_3	550	288
K_2CO_3(47.8)-52.2K_2CO_3	710	176
K_2CO_3(50)-50Na_2CO_3	710	163

[a] wt.%

2.1.3 Chemical Heat Storage

Chemical heat storage refers to a technology whereby energy is stored and released through breaking and/or reforming molecular bonds in a reversible chemical reaction, as illustrated as follows:

$$C + \text{heat} \longleftrightarrow A + B$$

In this reaction, a compound (C) absorbs heat and is converted into A and B; When A and B are combined together in the reverse reaction they give C and release heat; thus realising the charging and discharging processes. Clearly, the heat stored depends on the amount of storage material (C), the endothermic heat of the reaction, and the extent of conversion. While the storage material can be in any state, normally C is in a solid or a liquid state. One of the A and B is often in the same state as C, and the other can be in any state. In terms of industrial applications, gas-solid and liquid-solid systems are regarded as promising due to relatively easy separation of the materials and heat and mass transfer management. The amount of chemical heat can be calculated by:

$$Q = am\Delta h \tag{2.3}$$

where

Q = heat stored in the material (J),

m = mass of the material (g),

Table 2.12: Thermal properties of common heat storage materials [86, 87]

	Material	Specific heat capacity (kJ kg^{-1} K^{-1})	Latent heat (kJ kg^{-1})	Reaction enthalpy (kJ kg^{-1})
Sensible	Rock	0.9	–	–
	Sandstone	0.71	–	–
	Brick	0.84	–	–
	Soil	0.46	–	–
	Concrete	1.13	–	–
Latent	Paraffin wax	2.3	174.4	–
Chemical heat	$CaCl_2 + H_2O \longleftrightarrow CaCl_2 \cdot H_2O$	3.06	–	433.6
	$Zeolite + H_2O \longleftrightarrow Zeolite \cdot 4.5\,H_2O$	1.07	–	1107
	$FeO + CO_2 \longleftrightarrow FeCO_3$	0.48	–	698.3

a = the extent of the conversion,

Δh = enthalpy of reaction.

The advantages of chemical heat storage lie in the fact that they provide high storage energy densities [83], indefinitely long storage duration at near ambient temperature with negligible heat loss [84] (though the storage materials need to be heated/cooled between the reaction temperature and the ambient temperature for charge/discharge), and a wide range of working temperatures (from ∼-50 to over 1000 °C). Moreover, the chemical heat storage methods can also serve as a heat-pump, which have several additional advantages over that of traditional vapour-compression heat pumps [85]. Table 2.12 compares the energy density of three chemical heat storage materials with some common sensible and latent heat storage materials. Note that the reversible reactions discussed above can also be sorption based processes and the sorption can be physical, chemical, or a combined physical and chemical process.

As discussed in Section 2.1.2, over a certain temperature range, PCMs hold a much higher energy density than sensible heat storage materials due to the latent heat of the phase change. According to Table 2.12, the chemical storage materials are some 3 to 8 times higher in terms of energy density compared with PCMs, which have been regarded as one of the most important advantages of the materials[88–90]. Note that although the energy density of chemical storage materials is high, their system based energy density is much lower due to the need to store other reactants involved. This makes them not as promising as claimed, compared with PCMs.

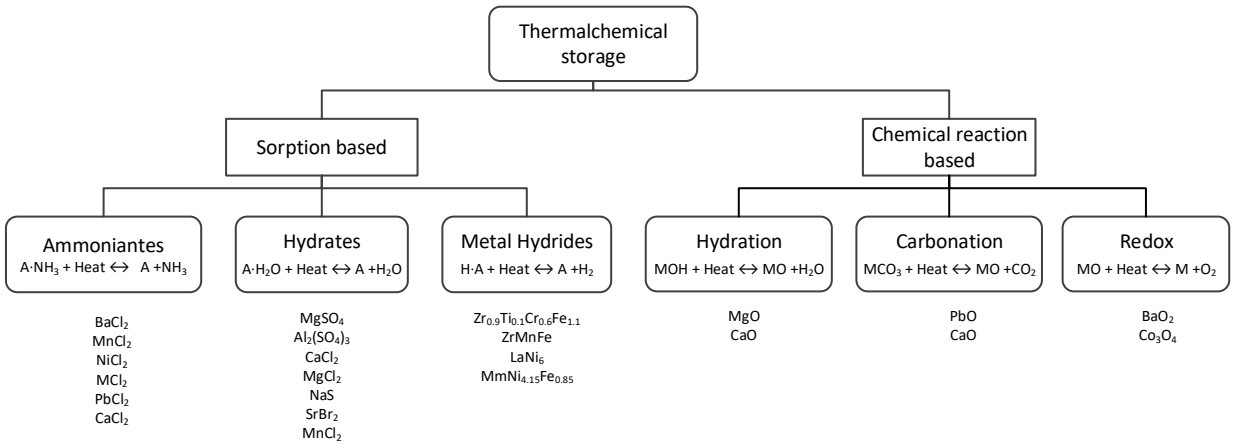

Figure 2.3: Classification of thermochemical storage

Selection of chemical storage materials needs consideration of the following (on top of the others aspects considered above):

- The reaction should be highly reversible and has little degradation over a large numbers of cycles.
- The reaction temperature should be in line with the temperature for the application[88].
- The reaction rate should be fast enough so the charging and discharging can be carried out rapidly.
- The storage materials and reactants should possess properties that can be engineered to give a practical system.

As mentioned above, the thermal chemical storage can be classified into reversible chemical reaction and sorption categories; see Figure 2.3.

Sorption Based Storage Materials

Goetz, Spinner, and Lepinasse [91] investigated a thermochemical cooling system using $BaCl_2$ and $NiCl_2$. Based on the consistency between experimental and simulated results,

the study suggested that the proposed small-scale model can be applied to other reactive systems. Li et al. [92–94] studied a combined double-way chemisorption refrigeration cycle aiming at improving the refrigeration system performance. $BaCl_2$-NH_3 and $MnCl_2$-NH_3 were chosen as the working pairs, with $MnCl_2$ as the high temperature (∼180 °C) medium, and $BaCl_2$ the low temperature medium (∼30 °C). The coefficient of performance (COP) in the system was improved by 60% compared with the resorption cycle. Haije et al. [95] studied a resorption heat transformer based on the ammoniates of $MgCl_2$ and LiCl with the aim of upgrading the waste heat from a temperature between ∼100 to 150 °C to a temperature between ∼180 to 220 °C. The $MgCl_2 \cdot (2 \leftrightarrow 6)\ NH_3$ and LiCl $\cdot (1 \leftrightarrow 3)\ NH_3$ worked successfully for upgrading the heat with a lift of at least 50 °C. The experimental results for the first time provided the feasibility of a high temperature upgrading transformer on the scale of 1kW, driven by a low temperature heat source.

Van Essen et al. [96, 97] studied the $MgSO_4 \cdot 6H_2O$ as potential storage material for compact seasonal heat storage of solar heat. Their experiments indicated that the dehydration of $MgSO_4 \cdot 6H_2O$ has a high energy density. It was revealed that under low-pressure conditions the dehydrated material was able to react with water under practical conditions. Boer et al. [98] worked to develop a prototype of a modular solid-soption cooling system called SWEAT (Salt Water Energy Accumulation and Transformation) for residential and industrial applications. Na_2S was used as the solid sorbent for water vapour. The heat storage capacity in the study was 3.2 kWh with an efficiency of 84 %. The cold storage capacity was 2.1 kWh and the COP was 0.57. Lahmidi, Mauran, and Goetz [99] investigated heat and cold storage by solid-gas sorption in working conditions adapted to a solar thermal system using flat panels. They used solid $SrBr_2$ to react with water and showed promising energy density. Zeolites are considered to be a promising thermochemical storage material for levelling the load within a district heat network by Kato [100] and Hauer [101]. They built a storage system with a heat load of 95 kW for 14 hours a day in a school building in Munich. The storage density of Zeolite 13X reached 124kWh m^{-3} for heating and 100kWh m^{-3} for cooling. Upon impregnation with salts, the

material could store energy at a lower temperature, providing an avenue for applications of common solar collectors.

A metallic pair of $Zr_{0.9}Ti_{0.1}Cr_{0.6}Fe_{1.4}/Zr_{0.9}Ti_{0.1}Ce_{0.9}Fe_{1.1}$ was used in a prototype heat pump for cooling driven by waste heat exhausted from vehicles and industrial plants[102]. The lowest cooling temperature achieved was ∼18 °C with a ∼200 °C heat source at an ambient temperature of ∼30 °C. Willers, Wanner, and Groll [103] investigated a multi-hydride thermal wave device for simultaneous heating and cooling applications. Seven different metal hydrides were used at the high temperature side and two at the low temperature side. Their experimental results with a 60% hydrogen inventory was obtained. The COP for the heating was about 1.4 and 1.1 for the complete cycle.

Reversible Reaction Based Storage

Kato et al. [104] studied a chemical heat pump based on a reversible reaction of $MgO(s) + H_2O(g) \longleftrightarrow Mg(OH)_2(s)$ for the utilization of waste heat. Both modelling and experiment were carried out. They found that the heat output rate of the device was ∼366 W kg^{-1} at ∼373 K, which was much higher than 100 W kg^{-1} for a calcium chloride/lithium bromide/water chemical heat pump system. The average diameter of $Mg(OH)_2$, particular in their work, was 10 μm to minimise mass transfer issues. Kato et al. [105] and Ryu et al. [106] studied chemical heat pumps with mixed hydroxides as heat storage materials. It was found that $Mg(OH)_2$ could not be dehydrated at 200-300 °C, the waste heat temperature, whereas the use of a mixture of $Mg(OH)_2$ and $Ni(OH)_2$ could store heat at the same temperature range. Halstead and Moore [107] studied the dissociation, association and equilibrium of $CaO(s) + H_2O \longleftrightarrow Ca(OH)_2(s)$ in the 1950s. Fujimoto, Bilgen, and Ogura [108] developed a mathematical model for dynamic simulation of a $CaO/Ca(OH)_2$ chemical heat pump system, and the models were validated experimentally in a prototype system. Ogura, Yamamoto, and Kage [109] examined the efficiency of the $CaO/Ca(OH)_2$ chemical heat pump for heat storing and heating/cooling, and found that the chemical heat pump was more efficient than other type of heat pumps under an

appropriate heat source condition. Chemical heat pumps have been successfully shown to upgrade the temperature to a level that could not achieved by a mechanical heat pump. Criado, Alonso, and Abanades [110] studied the reaction kinetics of $CaO/Ca(OH)_2$ under appropriate operation conditions for storage applications involving fluidized beds. They found that the reaction rates they observed in all cases were considerably higher than the existing reports under comparable conditions, which indicated that the resistances in several previous studies were incorrect.

Barker [111] studied the reversible reaction of $CaCO_3 \leftrightarrow CaO + CO_2$ at 866 °C, and found that the decomposition of $CaCO_3$ was always complete while the carbonation of CaO was not. They suggested that the reversibility of the reaction be limited by the surface area of the particles, which could be improved by using particles smaller than 44nm in diameter. Kato et al. [112] developed a CaO/CO_2 and PbO/CO_2 reaction system for utilizing high-temperature waste heat from nuclear reactors and other high temperature heat sources. The heat output by carbonation of CaO was found to be up to 670 W kg^{-1} at temperature of ~870 °C and a pressure up to 1 atm.

Fahim and Ford [113] studied the reaction of BaO_2/BaO in the temperature range of ~650 - 900 °C. Their results indicated that the storage system had a storage capacity of 3.0147×10^9 J m^{-3}. However, the reversibility was not favourable due to large size of BaO_2 particles. They suggested that the reversibility might be improved with particles less than 10 μm in diameter. Bowrey and Jutsen [114] achieved a 93 percent reversibility of the BaO/BaO_2 reaction experimentally and showed potentially practical application of the reaction.

2.2 Thermal Properties of Nanosuspensions

Nanoparticles are defined as particles with at least one dimension smaller than 100 nm. Such materials have been shown to have some unique features such as thermal, optical, catalytic and electrical properties. As a result, numerous studies have been conducted

over past few decades. This section will review the properties of nanoparticle suspensions and composites. Particularly those relates thermal energy storage.

2.2.1 Thermal Conductivity

Numerous experimental, theoretical and modelling studies have been reported on the use of nanoparticles to enhance the thermal conductivity of liquid and solid heat transfer fluids.

Chol [115] was first to use the term nanofluids (NFs) for dilute suspensions of nanoparticles. Xuan and Li [116] mixed Cu nanoparticles with water and transformer oil and measured the thermal conductivity of the resulting nanofluids with different particle fractions. A considerable level of thermal conductivity enhancement was observed. For water based nanofluids, the thermal conductivity was enhanced by 78% at a nanoparticle volumetric loading of 7.5%. For the oil-Cu nanofluid, a 43% thermal conductivity enhancement was found with a particle volume fraction of 7.5%. Eastman et al. [117] dispersed Cu nanoparticles in ethylene glycol (EG) and studied the thermal conductivity of the nanofluids. With a volumetric concentration of 0.3% volume fraction of Cu nanoparticles, the thermal conductivity of the fluid was enhanced by 41%. Efforts have been made to predict thermal conductivity of nanofluids using conventional models such as the following Hamilton and Crosser's model[118]

$$k_e = k_0 \left[\frac{k_m + (n-1)k_0 - (n-1)\alpha(k_0 - k_m)}{k_m + (n-1)k_0 + \alpha(k_0 - k_m)} \right] \tag{2.4}$$

where k_e, k_0, k_m represent the effective, particle and liquid thermal conductivity n is the shape factor, and α is the particle volume fraction.

It was found that direct use of these conventional models failed to predict the experimental results, which could be different by an order of magnitude. Hong, Yang, and Choi [119] used a sonication method to prepare EG based Fe nanofluids, and observed that the Fe nanofluids exhibited a higher effective thermal conductivity enhancement than that of

Cu nanofluids. They also found that the thermal conductivity of Fe based nanofluids increased non-linearly with increasing particle volume fraction. Clustering of nanoparticles in the based liquid was proposed to be responsible for these experimental observations. In a subsequent study, Hong, Hong, and Yang [120] studied the influence of the clustering of Fe nanoparticles on the thermal conductivity of nanofluids. The results indicated that the thermal conductivity was related to the aggregation of nanoparticles, which also explained the non-linear relation between thermal conductivity and particle fraction. Patel et al. [121] studied water-Au and water-Ag nanofluids. A 21% thermal conductivity enhancement was found in the water-Ag nanofluids for water at a particle volume concentration of 0.00026%. Within a volume concentration of 0.011% Au particles, the enhancement was reported to be 14%. The thermal conductivity enhancement was found to be linear with the particle fraction but non-linear with the temperature.

Metal oxides based nanofluids have also been studied extensively, and Al_2O_3 and CuO are most commonly used in those studies as they are inexpensive metal oxide nanoparticles in enhancing thermal conductivity. Eastman et al. [122] dispersed Al_2O_3 and CuO in water and the highest thermal conductivity enhancement was 48% with 4 volume % CuO nanoparticles in water.

Lee et al. [123] studied heat transfer behaviour of nanofluids with 24nm CuO and Al_2O_3 particles in water and EG, respectively. The thermal conductivity was observed to be almost linear with nanoparticle concentration when the concentration was less than 5% by volume. Xie et al. [124] carried out study on the thermal conductivity of SiC based nanofluids and observed similar behaviour, namely the thermal conductivity depended linearly on the particle volume fraction. They also compared their experimental results with the Hamilton and Crosser model. A good agreement was found for the suspensions of large SiC particles, whereas significant deviation occurred for small SiC particles. Das et al. [125] carried out research on the temperature dependence of thermal conductivity enhancement of nanofluids. Aqueous suspensions of Al_2O_3 and CuO nanoparticles were used in the work. They found the thermal conductivity of both nanofluids was posi-

tively related to the increase of temperature. Ding, Wen, and Williams [126] conducted research on the thermal behaviour of TiO_2 nanofluids and observed that the maximum enhancement was about 6% higher than that predicted by Bruggemen model. Their work was followed by Murshed, Leong, and Yang [127] who studied the thermal behaviour of nanofluids containing rod and spherical TiO_2 nanoparticles using the transient hot-wire method, and found that the experimental results were significantly higher than predictions using existing effective thermal conductivity models for solid-liquid mixtures. respectively. Based on the data, Murshed, Leong, and Yang [127] introduced an integrated correlation model for the calculation of thermal conductivity of nanofluids.

Yu and Choi [128] proposed a modified Maxwell model[129] which included the impact on the thermal conductivity of a nanolayer between nanoparticles and base liquid. The modified model was shown to have the potential for up to an eight-fold increase in the thermal conductivity of nanofluids over that predicted by the Maxwell model. The modified model was also compared with experimental results of water-Cu and EG-Cu nanofluids, and reasonably good agreement was achieved. Xue [130] compared 6 traditional models for thermal conductivity of solid-liquid mixtures [118, 129, 131–134] and also developed a model considering the interfacial layering effect. The new model was shown to be in good agreement with the experimental data. A modified Hamilton-Crosser model was also proposed by Yu and Choi [135] to include the effect of interfacial layer on the thermal conductivity by considering a solid particle-in-liquid suspension with monosized ellipsoidal particles of semiaxes. Although the model proposed by Yu and Choi [135] was shown to be in good agreement with the experimental data, it did not predict the nonlinear dependence on particle concentration. Jang and Choi [136] derived a theoretical model based on kinetic theory[137], taking Kapitza resistance[138] and convection into account. This study led to their suggestion that Brownian motion of nanoparticles is one of key mechanisms governing the thermal properties of nanofluids. Although the model was able to predict the particle-size and temperature dependency of thermal conductivity of nanofluids, there was a lack of sound interpretation based on fundamental physics. Gupta

and Kumar [139] studied the thermal conductivity of nanofluids with Brownian dynamics simulations. It was observed in their study that the random "walk" of nanoparticles was a main factor that led to the increased thermal conductivity. The suggested effects of Brownian motion and the Brownian motion induced convection were shown to be minor by a study by Keblinski, Prasher, and Eapen [140]. Such a debate has been going for sometime; see [141–143].

The enhancement of thermal conductivity of nanofluids reported by different researchers is still controversial and not conclusive. 34 institutes[144] conducted one study on the thermal conductivity of aqueous and non-aqueous base fluids with metal and metal oxide nanoparticles. They found that the experimental data was in good agreement with the effective medium theory developed for dispersed particles by Maxwell in 1881[145], suggesting that no anomalous enhancement of thermal conductivity was achieved in the nanofluids. Utomo et al. [146] studied the thermal conductivity, viscosity and heat transfer coefficient of titania and alumina nanofluids. The thermal conductivity of alumina nanofluids was in good agreement with the prediction of Maxwell model, whereas that of titania nanofluids is slightly lower than the model prediction because of the introduction of stabilisers. No anomalously high thermal conductivity enhancement were found in the study, which shows that titania and alumina nanofluids do not enhance the thermal conductivity in water.

2.2.2 Specific Heat Capacity

The thermal conductivity of nanofluids has been extensively studied since it was first observed some 20 years ago. However, the energy storage capacity of a TES material mainly depends on specific heat capacity and latent heat if there is phase change. Any breakthrough in the improvement on the energy density with adequate and cost-effective means is therefore highly sought after. There are reports on the use of nanoparticles for enhancing the specific heat capacity of TES materials which was significantly changed by mixing with nanoparticles. Wang et al. [147] and Wang, Zhou, and Peng [148] observed a

$\sim$25% enhancement on the specific heat capacity of Al_2O_3 nanoparticles compared with the bulk Al_2O_3. Their work indicated that with the extremely large specific surface area, the contribution of surface atoms on the specific heat capacity should not be neglected. In this subsection, relevant work on specific heat capacity enhancement of nanofluids is summarised.

Experimental observations and theoretical analysis

Zhou and Ni [5] studied the specific heat capacity of water-based Al_2O_3 nanofluids. The specific heat capacity was found to decrease with an increase the increase in nanoparticle volume fraction, in good agreement with a classical thermal equilibrium model for mixtures as follows (equation 2.5):

$$C_{p,mixture} = \frac{m_p C_{p,p} + m_f C_{p,f}}{m_p + m_f} \tag{2.5}$$

Where $C_{p,mixture}$,mixture is effective specific heat capacity of mixture, $C_{p,p}$ is the specific heat capacity of particle(s), $C_{p,f}$ is the specific heat capacity of fluid, m_f is the mass of fluid, m_p is the mass of particles, which is used for calculating specific heat capacity of mixtures.

Vajjha and Das [149] measured the specific heat capacity of three nanofluids containing Al_2O_3, ZnO, and SiO_2, and found their specific heat capacity decreased as the volumetric concentration of nanoparticles increased. Their observations are in line with that of Zhou and Ni [5], and hence agree with the conventional model for mixtures.

Zhou et al. [6] measured the specific heat capacity of EG based CuO nanofluids and compared the data with two models for the specific heat capacity of nanofluids. They found that the presence of nanoparticles had a negative influence on the specific heat capacity of the EG-CuO nanofluids. Similar observations were made by Barbés et al. [150] on the specific heat capacity of EG-Al_2O_3 in the temperature range of 303.1 K - 330.4 K.

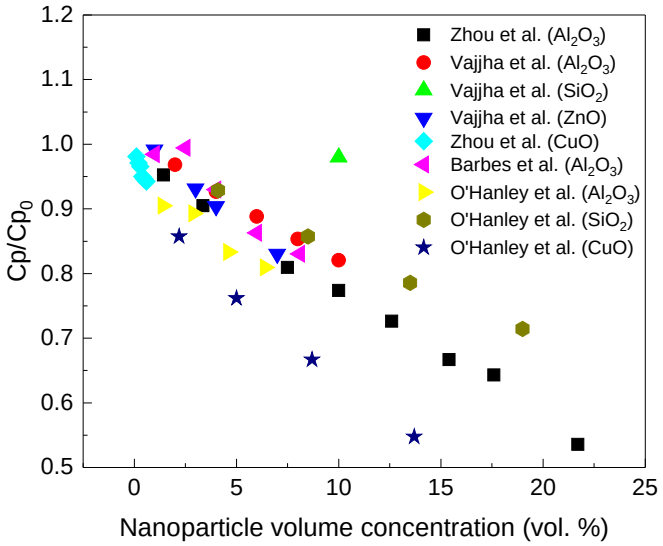

Figure 2.4: The Cp/Cp_0 in water or EG based nanofluids [5, 149–151]

O'Hanley et al. [151] measured the specific heat capacity of water-based SiO_2, Al_2O_3, and CuO nanofluids at various particle concentrations. Their experimental results were compared with two mixture models for the specific heat capacity, and showed that the classical model (Equation 2.5) yields an accurate prediction.

From the above, one could conclude that the specific heat capacity of water or EG based nanofluids agrees well with the classical model prediction. However, molten salt based nanofluids have been shown to disagree with the conventional theory. Shin and Banerjee [3] mixed molten chloride salts with SiO_2 nanoparticles and observed an anomalous specific heat capacity enhancement. They used the following protocol for preparing the nanofluids: Salts and nanoparticles were firstly mixed in water and sonicated by an ultra sonicater. Vaporisation of water was performed to obtain a salt-nanoparticle mixture. The specific heat capacity of the sample was then measured at above 500 °C. With 1 wt% of SiO_2 nanoparticles, the specific heat capacity of the salt based nanofluid was enhanced by 14.5%. Three mechanisms were proposed to explain the experimental observation; see later for more details.

Shin and Banerjee [7] continued their work by adding SiO_2 into carbonate based

salts, with same preparation method as that for the chloride salt. The specific heat capacity of the carbonate salt based nanofluid was seen to increase by ∼24% with 1 wt% of nanoparticles. Clearly these results contradict the predictions by the equilibrium based theory for the specific heat capacity of mixtures (Equation 2.5)[4]. They did SEM analysis of the sample and observed a substructure in the eutectic salt adjacent to nanoparticles. An intercalated network was also observed in the vicinity of the nanoparticles where the eutectic salt seemed to have a higher density. Based on experimental observations, it was hypothesised that the molten salt near nanoparticles were "compressed" due to unknown mechanisms. Such mechanisms might have caused the enhancement of the specific heat capacity.

Based on the above study, Tiznobaik and Shin [152] investigated experimentally the effect of addition of SiO_2 in different sizes on the specific heat capacity of the salt. Four different nominal sizes of SiO_2 (5, 10, 30, and 60 nm) were used in their work. The concentration of the nanoparticles was 1 wt%. The specific heat capacity was found to be enhanced by the addition of nanoparticles by 23–28% regardless of the size of nanoparticles. SEM analysis showed a needle-like structure with an exceptionally large specific surface area compared with the bulk eutectic salt. Through examination of the backscattered electron micrograph, the molar composition of the needle-like structures was found to be different from the bulk salt.

Chieruzzi et al. [153] produced molten salt suspensions of SiO_2, Al_2O_3, TiO_2, and a mix of SiO_2-Al_2O_3 nanoparticles and measured their thermal properties including heat of fusion and specific heat capacity. It was found that different nanoparticles affected the specific heat capacity differently. The best results were obtained with the 1.0 wt.% of SiO_2-Al_2O_3 nanoparticles which enhanced the specific heat capacity of the salt by 22% whereas the addition of TiO_2 to salt gave deterioration.

Nitrate salt containing nanoparticles was studied by Dudda and Shin [154]. They doped with 1 wt% of SiO_2 nanoparticles of nominal sizes 5, 10, 30, and 60 nm, respectively, with the dissolution mixing method. It was found that the nanoparticles with 60 nm in size

gave the best enhancement of 27%, whereas the 5 nm particles only promoted the specific heat capacity by 8%. A layering structure was observed at the vicinity of nanoparticles which agreed with the semi-solid layer phenomenon reported by Xue et al. [155], Li et al. [156], and Oh et al. [157]. The small nanoparticles used in their work were agglomerated in the nanofluids, which decreased the surface area and was proposed to cause the lower enhancement.

Lu and Huang [158] mixed nitrate salt with Al_2O_3 nanoparticles with two sizes of 13 nm and 90 nm and studied the specific heat capacity of the nanofluids. They used the same sample preparation method mentioned above and found a reduction in specific heat capacity. They proposed a nanolayer theory to explain the experimental phenomena.

Andreu-Cabedo et al. [159] studied the specific heat capacity of molten nitrate salt based nanofluids with different weight fractions (0.5 wt%, 1.0 wt%, 1.5 wt%, 2.0 wt%) of SiO_2 nanoparticles. The optimal concentration of nanoparticles was found to be 1.0 wt%,which gave an enhancement of 25% in the specific heat capacity. The available particle surface area of their samples were evaluated by dynamic light scattering (DLS) and SEM. The largest surface area was found to be for the 1 wt% sample. This indicated that the specific surface area was a key parameter in the enhancement of specific heat capacity.

Jo and Banerjee [160] studied the specific heat capacity of carbonate salt based graphite nanofluids. Two different approaches were used to make the nanofluids for comparison purpose. The main difference in the preparation methods was the rate of evaporation process with Method 1 at a much more rapid rate than that in Method 2. The maximum enhancement of specific heat capacity of the eutectic salt was 40% and 57% in the solid and liquid phases, respectively. Method 1 yielded higher enhancement in the specific heat capacity for all of the samples used in this study. A migration of molar composition was observed in the experiment, which was connected to the extent of the enhancement of the specific heat capacity. MD simulations were performed to explore the salt atom distribution in the adjacent area of a nanoparticle. It was observed that with

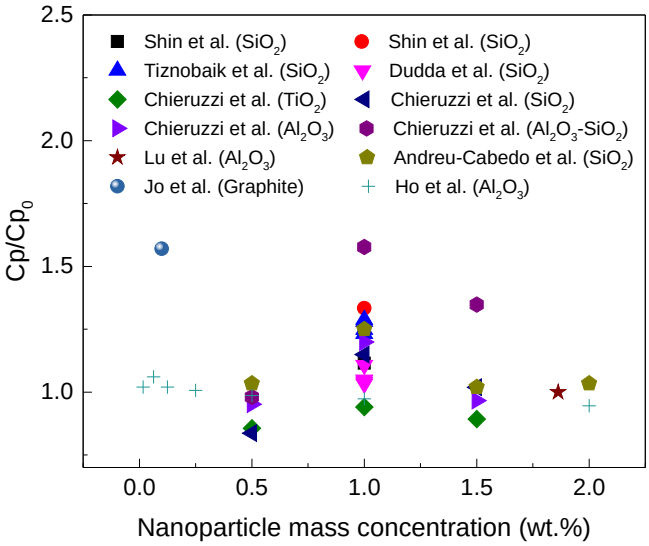

Figure 2.5: The Cp/Cp_0 in molten salt based nanofluids [152–154, 158–162]

different molar composition of the molten salt, the atoms distributed differently. However, the results were inclusive in terms of the mechanism of the enhancement.

Ho and Pan [161] studied the specific heat capacity of molten salt based nanofluids containing Al_2O_3 nanoparticles. They used a different preparation methods by mixing the nanoparticles with salt while the salt was melted in a container on a hot plate with the salt stirred. The optimal nanoparticle concentration of 0.063 wt% was found which increased the specific heat capacity by 19.9%. Agglomeration of nanoparticles were found to occur, which was not negligible when the concentration of nanoparticle exceeded 0.016 wt.%. The enhancement of specific heat capacity was suggested to become negative when the agglomeration reduced the surface area of nanoparticles.

Mechanisms of Specific Heat Capacity Enhancement

Shin and Banerjee [3] proposed three independent competing inter-molecular interaction mechanismsas Mode I, II and III respectively. Mode I suggested that the higher specific heat capacity of nanofluids be attributed to the higher specific heat capacity of nanoparticles which have a higher surface energy[147]. They suggested that the surface atoms of

the nanoparticles are less constrained due to the less number of bonds, leading to the atom vibrations at a lower natural frequency and higher amplitudes, and hence higher surface energy and higher specific heat capacity. Mode II assumes that the interfacial thermal resistance between the nanoparticles and base fluids provides extra thermal storage capability[155, 163]. This resistance is normally negligible at the macroscopic scale but is amplified to an extent that significantly affects the thermal storage in nanofluids due to the high interfacial surface area. Mode III suggested that a "semi-solid" layer be formed adjacent to the surface of nanoparticles[156, 157]. This "semi-solid" layer contributes to the enhancement of the specific heat capacity of the nanofluid.

Based on the experimental and simulations results, Jo and Banerjee [160] suggested that the introduction of nanoparticles may have changed the local molar composition of the salt based fluid, owing to the formation of a compressed liquid layer adjacent to the surface of nanoparticles. The changed composition of the fluids gives a higher specific heat capacity.

As shown earlier that the water or EG based nanofluids have a specific heat capacity that agrees with the classic mixing model, which is very different from that of the salt based nanofluids. These literature results are summarized in Figure 2.4 [5, 149–151] and Figure 2.5 [152–154, 158–162] . All data in Figure 2.4 have shown a decrease with the addition of nanoparticles, whereas Figure 2.5 gives an increase tendency. This contradicting sets of results suggests that the mechanisms of the specific heat capacity change due to nanoparticles cannot be simply explained by existing models or theories. Although there are several theories proposed in the literature, none of them have been validated by either experiment or by simulation. Further, none of these theories provides a reasonable explanation to satisfy all the experimental observations.

2.3 MD Simulations of Thermal Properties

The MD simulation allows the direct simulation of the motions and interactions of particles (atoms or molecules). It has increasingly been used to study various thermal problems in recent years[164–168]. Analysing the interactions between and trajectory of atoms or molecules, physical phenomena at a scale are difficult to observe using current tools and methodologies. MD simulations can also be used to test the validity of a theoretical model or refine the model since they provide a molecular level insight into the theory. In this section, MD modelling work related to thermal energy storage is reviewed.

2.3.1 MD Simulation Studies of TES Materials

Molten salts have been studied and applied as TES materials. Within this category of TES materials, alkali halides have been studied extensively using MD simulations. Fumi and Tosi [169] and Tosi and Fumi [170] developed intermolecular interaction parameters for alkali halides in 1964, leading to the Tosi-Fumi potentials, which are still used widely nowadays. For example, Anwar, Frenkel, and Noro [171] and Eike, Brennecke, and Maginn [172] computed the melting point of sodium chloride using the Tosi-Fumi potential; Galamba, Castro, and Ely [173] and Galamba, Castro, and Ely [174] calculated the viscosity and thermal conductivity of molten alkali halides.

Nitrate salts are widely used in the heat storage applications particularly in solar thermal power generation. However, little has been done on the use of MD simulations to such salts. Yamaguchi et al. [175] used a rigid nitrate model in which simple Coulomb pair potentials with Born-type repulsions were adopted to simulate the liquid phase properties of lithium and rubidium nitrates at 550 and 600 K, respectively, and they further compared their results against X-ray and neutron diffraction experiments. Structure functions derived from the X-ray and neutron experiments were well reproduced by the simulations.

Adya et al. [176] carried out MD simulation for the molten $NaNO_3$, $NaNO_2$ and their eutectic mixture. Those simulated structure successfully reproduce the X-ray diffraction

results. Parameters determined for the component salts were employed during the simulation. The simulation results were used to calculate the diffusion coefficients of the component ions. Adya and Neilson [177] measured partial pair radial distribution function of different alkali nitrate salts and compared the experimental results with their MD simulation results published earlier[175, 176] and found the results in good agreement.

Katō et al. [178] introduced a flexible model for nitrate ions in their MD simulation works. Coulomb pair potentials with Born-type repulsion was adopted for the interionic interaction. In their study, cation dependence of the ionic dynamics was studied by MD simulations of molten $LiNO_3$, $NaNO_3$ and $RbNO_3$. The force field they used reproduced reasonably well the translational, charge transport and orientation behaviour. However, several disagreements between the simulation and experimental results were observed, which suggested that change of electron cloud by neighbouring ions may have considerable influenced the ionic dynamics in the molten nitrates.

Vöhringer and Richter [179] performed MD simulations for pure molten $LiNO_3$, $NaNO_3$, KNO_3, and $RbNO_3$ salts with a focus on the interaction potential, calculation of pressure for comparison with real values. They also employed Coulomb pair potentials and Born-type repulsion in their simulation, and like others, improvement was made by them to introduce a short-range-attraction term to meet the real behavior of the liquid. In their study, the self-diffusion coefficients were compared with experimental data from nuclear magnetic resonance spin echo method, and the improved model was shown to yield better agreement.

Ribeiro [180] developed a polarizable potential model, the fluctuating charge model (FCM), in MD simulations of alkali nitrate salts. They found that a single potential model for (M_1, M_2)NO_3 mixtures gave the correct composition dependence of M_1 and M_2. Urahata and Ribeiro [181] extend the FCM[180] for the NO_3^- anions by considering the flexibility and polarization effects in their MD simulations. Comparisons between equilibrium and dynamical properties of $LiNO_3$ simulated with rigid ion model (RIM) including flexibility (RIM-FLEX), FCM, FCM with flexibility (FCM-FLEX) were discussed.

The overall outcome of their study was that the inclusion of polarization is more relevant to the properties of the simulated system than the inclusion of flexibility.

Jayaraman et al. [182] used a Buckingham potential to simulate $NaNO_3$, KNO_3, and $LiNO_3$. Flexibility of the model was added by introducing harmonic terms. A Nose-Hoover temperature thermostat was used to perform the simulation in the canonical ensemble. Liquid phase densities, viscosities, thermal conductivities, heat capacities, and melting points were calculated for each salt. A reversible non-equilibrium molecular dynamics algorithm (RNEMD) method was used to calculate viscosities and the results showed a 1% deviation from experiments for $LiNO_3$, but deviations of approximately 30% and 20%, respectively, for $NaNO_3$ and KNO_3. Thermal conductivities were also calculated by using the RNEMD method and the simulation results captured the trends of the experimental data. The computed melting point of 591 ± 18 K for $NaNO_3$ was close to the experimental result of 578K, while that of $LiNO_3$ and KNO_3 deviated from the experimental values by around 70 and 90K, respectively. It was noted that the simulations showed that the melting point was extremely sensitive to small differences in the free energy between the crystal and liquid phase. This suggests that extremely accurate energies were needed to obtain an accurate melting point to within 10K or so. This is challenging with either ab initio or empirical potentials. The computed heat capacity of $LiNO_3$ was equal to the experimental value within computed uncertainties. For $NaNO_3$ and KNO_3, the computed heat capacities were higher than the measurements by about 12-25% (0.2-0.3 cal g^{-1} K^{-1}). It was also found that melting points were extremely sensitive to the force field accuracy, which should be used in future work on salt force field validation studies.

As is discussed, it is clear that MD simulations are playing an increasing role in helping develop an understanding of properties of molten salts. However, MD simulation of nitrate salts are still evolving and no completely straightforward method is currently available. Coulomb pair potentials with Born-type repulsion has been a popular force field for simulating nitrate molten salts. In order to increase the accuracy, flexibility and polarization have been introduced into MD simulations. Furthermore, attempts have

been made to introduce more force fields into MD simulations for nitrate salts, such as Buckingham potential. In summary, MD modelling of molten nitrate salts has shown some promising results. However, there is a significant amount of work that needs to be done before the method provides reliable predicting capabilities with accuracy.

2.3.2 MD Simulation Studies of Nanofluids

As reviewed earlier in this chapter, thermal properties of TES materials could be enhanced by adding nanoparticles. However, controversies occur and mechanisms are unclear. Although more experiments could help obtain more useful data, the mechanistic understanding of experimental observation is limited and can be speculative in many cases. By using MD simulation methods the interactions between and energy fluctuations of atoms could be observed and thermophysical properties of different materials under various conditions could be estimated.

Since the MD simulation allows the direct simulation of the motion and interactions of particles (atoms or molecules), it has increasingly been used to study various thermal transport problems in the recent years [164]. MD simulation has been successfully employed to calculate the thermal conductivity of a wide variety of liquids [183] and solids [9] with varying degrees of success. More recently, it had been used to calculate thermal conductivity of nanofluids (a suspension of particles with at least one dimension smaller than $\sim$100nm), which can be regard as a solid-liquid composite system [184].

Sarkar and Selvam [184] used the equilibrium molecular dynamics (EMD) method to calculate the thermal conductivity of an argon based copper nanofluid. They also attempted to correlate the enhancement of thermal conductivity to that of diffusion coefficients in nanofluids, and concluded that the main mechanism for the enhanced thermal conductivity is due to the highly enhanced fast liquid atom motion which helps to transport heat quickly in nanofluids.

Li et al. [156] investigated the effect of molecular layering at the liquid-solid interface on the thermal conductivity of the nanofluid by using MD simulation. Liquid argon

based copper nanofluids were used in their study. By tracking the movement of copper nanoparticles, they found a solid-like thin liquid layer of ∼0.5nm at the liquid-nanoparticle interface. This layer was attributed to the significant enhancement of the thermal conductivity.

Cui et al. [185] studied argon based nanofluids containing copper, ferric, and silver nanoparticles. They examined conductivity and radial distribution function (RDF) of these nanofluids, and suggested that the combination of changed microstructure of nanofluids and micromotions of nanoparticles be the main mechanism for the anomalous increase of thermal conductivity.

From above, one can see that most MD simulation studies on nanofluids have been focused on the thermal conductivity. Although reasonable results have been obtained, the dominant mechanism for the enhancement of specific heat capacity in nanofluids is still under debate.

2.4 Summary

By summarizing the literature surrounding the research of thermal energy storage materials, molten salts are one of the most favourable ones for high temperature energy storage applications. It was observed in many studies that the thermophysical properties of materials were changed by adding nanoparticles. However the results are sometimes contradictory and the mechanism for such phenomenon is still not conclusive.

This PhD study is therefore concentrated on modelling and validating the enhancement of thermal properties of molten salts, particularly specific heat capacity.

CHAPTER 3

EXPERIMENTAL AND MODELLING METHODS

This chapter explains the MD modelling method as well as experimental method for the validation of the modelling results.

3.1 Experiment

3.1.1 Instruments

The instruments employed in this PhD study are listed in Table 3.1. These devices were well calibrated before testing. More details of these devices and calibration methods will be given in Section 3.1.4.

Table 3.1: Instruments employed in this work

Name	Purpose	Manufacturer
Differential Scanning Calorimetry (DSC)	Specific heat capacity, melting point, latent heat	Mettler Toledo
Simultaneous Thermal Analyzer (STA)	Thermal stability	Netzsch
Quadrupole Mass Spectrometer (MS)	Chemical reaction	Netzsch
Laser Flash Apparatus (LFA)	Thermal conductivity	Netzsch
Zetasizer	Size of nanoparticles	Malvern
Scanning Electron Microscope (SEM)	Surface structure	Hitachi
Energy Dispersive Spectroscopy (EDS)	Element distribution	Hitachi
X-ray diffraction (XRD)	Crystal structure	Siemens

3.1.2 Materials

Inorganic salts were used in this study, which, as discussed in Section 2.1, for high temperature TES applications, these salts are among the most favourable candidates due to the virtues of their thermophysical properties and stability. Another reason for studying these salts is the enhancement of their specific heat capacity triggered by the addition of nanoparticles, which has only been found in salt based nanofluids so far.

In this PhD study, rather than using eutectic salt mixtures or the nanofluids based on these mixtures, single salt based nanofluids were examined, with the aim of simplifying the system and eliminating interference factors that may affect the observation of the underlying physics. Two main types of materials were used in the work, nitrate salts and silicon dioxide nanoparticles.

The salts used in the experiment were lithium nitrate, sodium nitrate and potassium nitrate, all in their anhydrous form, purchased from Sigma-Aldrich. The purity of the

salts were over 99.0%. They were used without further purification.

SiO_2 was chosen as the nanoparticles in the work which has been found to be able to enhance the specific heat capacity of the salts as inllustrated in the literature review. SiO_2 nanoparticles with different sizes and morphologies were used to investigate the mechanisms of the enhancement.

SiO_2 was chosen to be the suitable nanoparticle for enhancing the specific heat capacity in the molten salt. In the aim of investigating the mechanism behind the phenomena, I used SiO_2 nanoparticles with different particle sizes and morphology.

Silicon oxide (15-20nm):

Vendor: US Research Nanomaterials, Inc.

- Purity: 99.5%
- Average particle size (APS): 15-20nm
- True Density: 2.4g cm^{-3}
- Morphology: nearly spherical
- Crystal Phase: amorphous

Silicon oxide (20-30nm):

Vendor: US Research Nanomaterials, Inc.

- Purity: 99.5%
- APS: 20-30nm
- True Density: 2.4g cm^{-3}
- Morphology: nearly spherical
- Crystal Phase: amorphous

Silicon oxide (60-70nm):

Vendor: US Research Nanomaterials, Inc.

- Purity: 99.5%
- APS: 60-70nm
- True Density: 2.4g cm^{-3}
- Morphology: nearly spherical
- Crystal Phase: amorphous

Silicon oxide (micro-particle):

Vendor: Sigma-Aldrich

- Purity: 99.0%
- APS: 1-5μm
- True Density: 2.4g cm^{-3}
- Morphology: nearly spherical
- Crystal Phase: amorphous

Those particles were dispersed in the based liquid to make nanofluids containing 0.5, 1.0, 2.0, and 4.0% nanoparticles by mass.

3.1.3 Sample Preparation

Figure 3.1 illustrates the process of sample preparation for the salts with particles well dispersed within. Salt and nanoparticles were weighed first with an analytical balance with $\pm 0.1\mu$g precision (Mettler Toledo, type XP6U). The nanoparticles were then dispersed in distilled water (typically 20ml) in a beaker and mixed by a high power ultra-sonicator

(Fisher scientific, CL –334) for 5 minutes. The salt was then added to the aqueous based suspensions, and the resulting mixture was subjected to sonication for a further 5 minutes. The beaker was subsequently placed on a hot plate set at 130 °C to evaporate the water. This process gave a well dispersed salt-particle mixture. This method is similar to that used by Shin and Banerjee [3]. However, instead of employing an ultra-sonic bath and mixing the sample for 2 and 3 hours, a 500 W ultra-sonicator was used in this work and the mixing time was 5 minutes. This was because after subjecting the aqueous suspension to the sonication for 5 minutes, the size of particles showed little change with longer sonication. Except for the 5μ particles, , all other mixture showed that the average particle size was around 400nm in water. Pure salts without nanoparticles were also prepared using the method to serve as the benchmark sample for results comparison.

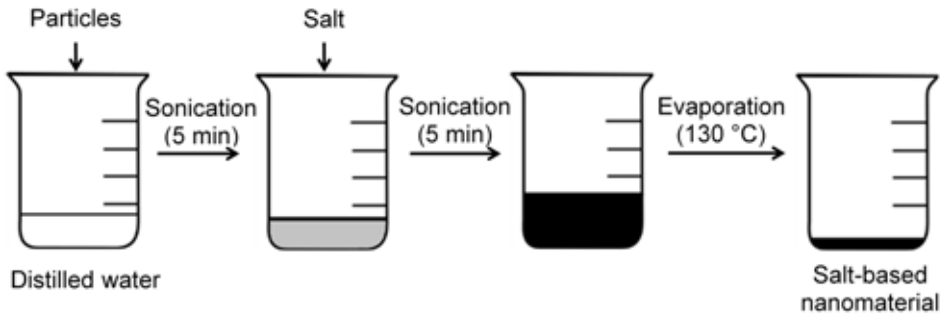

Figure 3.1: Sonication mixing procedure of preparing sample

3.1.4 Sample Characterisation

The samples were characterised by using a number of analytical devices. They are described in the following.

A scanning electronic microscope (SEM, TM 3030, JSM 7000 F) was used to observe the morphology, particle distribution and aggregation. The SEM is equipped with energy dispersion spectroscopy (EDS), which is used to map element distribution. A schematic configuration of the SEM is shown in Figure 3.2. An electron beam from A is focused via B on a sample surface held in C, generating a variety of signals due to beam-sample

surface interactions. This leads to high resolution information such as sample surface morphology, and chemical composition after processing in E. Sample are often coated with a platinum layer of 5 nm thick before analysis to enhance resolution.

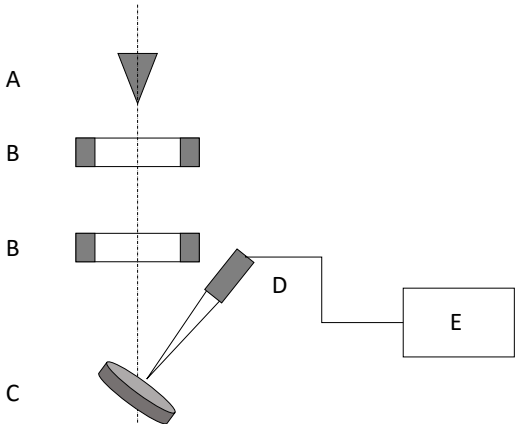

Figure 3.2: A schematic diagram of a SEM

A. Electron source (gun); B. Electron lenses; C. Sample stage; D. Detectors; E. Data output devices

An X-ray diffractometer (XRD) technique was used to analyse chemical compound and crystal structure of the samples. Arrays of atoms scatter X-ray on the sample surface through interactions with the surface atoms's electrons to produce secondary spherical waves emanating from the electrons. By measure the array of spherical waves, the arrangement of the atom array can be obtained.

A mass spectrometry (MS) was used to map possible molecules in the samples. Such a device works on the basis of mass to charge ratio.

In a typical mass spectrometric analysis, the sample is firstly turned into gas phase ions by electron ionization. Each primary product ion derived from the molecular ion undergoes fragmentation. The ions are then separated in the mass spectrometer according to their mass to charge ratio, and are detected in proportion to their abundance. Figure 3.3 shows a schematic diagram of a mass spectrometer.

A differential scanning calorimetry (DSC) was used to analyse various thermophysical properties of the samples including melting point, latent heat, and specific heat capacity. In a typical measurement, a sample and a reference are placed in their holders simultaneously, followed by raising their temperature at the same rate throughout the experiment.

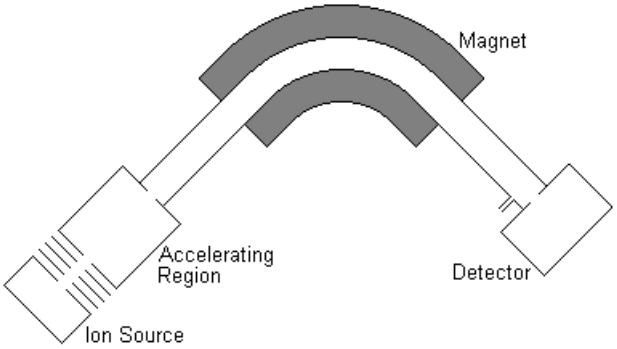

Figure 3.3: The essential components of a mass spectrometer

Heat flows to the sample and a reference are recorded as a function of temperature or time, which are used to evaluate the thermal properties of the sample. The reference is often an empty container, which is the same for holding.

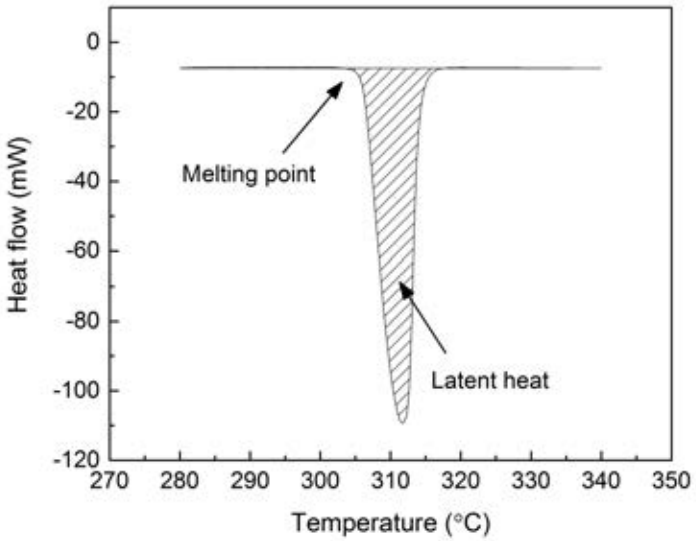

Figure 3.4: An example of a phase change process recorded by a DSC

Figure 3.4 illustrates how heat flow changes during a phase change process recorded by a typical DSC. When the sample is undergoing a phase transition, depending on whether the process is exothermic or endothermic, more or less heat will flow to the sample than that to the reference to maintain both at the same temperature. By detecting this heat flow difference, the device will be able to work out the amount of heat absorbed or released during the phase change and hence the latent heat of the phase change by integrating the

heat flow difference with respect to time. The onset of the heat flow variation is defined as the phase change temperature.

The specific heat capacity is a thermophysical property of substance that indicates the amount of heat required to change the temperature of a unit mass of the material by 1 degree Celsius or Kelvin degree. The most commonly used method for specific heat capacity measurements are to hold the substance either at a constant pressure or at a constant volume to give constant pressure heat capacity, C_p, or constant volume heat capacity, C_v, respectively. These two heat capacities are related. In this study, the measured specific heat capacity data are for C_p unless otherwise stated. The ASTM E1269-05 standard[186] was adopted in the work whereby a synthetic sapphire disk (α-aluminium oxide; alumina) was used as a heat flow calibration standard. The specific heat capacity of synthetic sapphire is given in Appendix A, and the specific heat capacity of a sample is calculated by using the following formula:

$$C_{p(sample)} = C_{p(standard)} \cdot \frac{HF_{(sample)} \cdot m_{(standard)}}{HF_{(standard)} \cdot m_{(sample)}} \tag{3.1}$$

where:

$C_{p(sample)}$ = specific heat capacity of the sample, kJ g^{-1} K^{-1},

$C_{p(standard)}$ = specific heat capacity of the sapphire standard, kJ g^{-1} K^{-1},

$HF_{(sample)}$ = corrected heat flows of the sample, mW,

$HF_{(standard)}$ = corrected heat flows of the standard sapphire, mW,

$m_{(sample)}$ = mass of the sample, mg,

$m_{(standard)}$ = mass of the standard sapphire, mg.

A laser flash analysis (LFA) was employed to measure the thermal diffusivity and thermal conductivity of the samples. The LFA technique was developed by Parker et al. [187] in 1961, and its working principle is shown in Figure 3.5. A laser pulse is used to momentarily heat the bottom side of a sample with 12.5 - 14 mm diameter and 0.5 - 4mm thickness. The temperature of the sample on the top side is measured with a radiation thermometer as a function of time. The thermal diffusivity can then be calculated by:

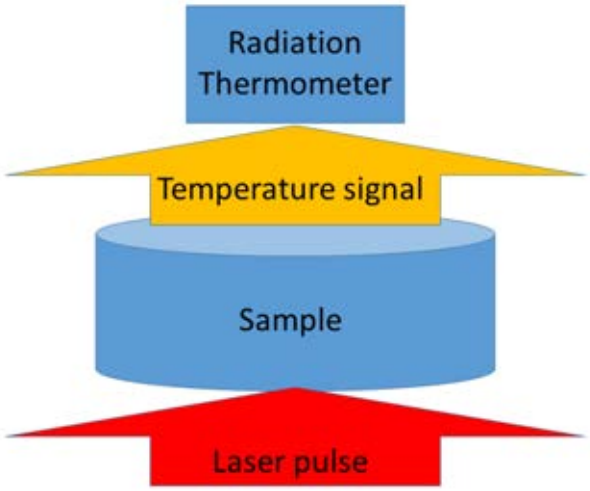

Figure 3.5: The measurement principle of LFA

$$\alpha = 0.1388 \cdot l^2 / t_{\frac{1}{2}} \tag{3.2}$$

where:

l = the thickness of the sample, mm,

$t_{\frac{1}{2}}$ = the time difference between the initiation of the pulse and the top side temperature when it reaches one-half of the maximum value, ms.

Equation 3.2 is from theoretical derivation [187].

The thermal conductivity then can be related to the thermal diffusivity, α by:

$$\lambda = \alpha C_p \rho \tag{3.3}$$

where:

λ = thermal conductivity of the sample, W m^{-1} K^{-1},

C_p = specific heat capacity of the sample, kJ g^{-1} K^{-1},

ρ = density of the sample, g cm^{-3}.

A thermal gravitational analyzer (TGA) was used to measure the change of mass of a sample as a function of temperature or time in a controlled atmosphere; see Figure

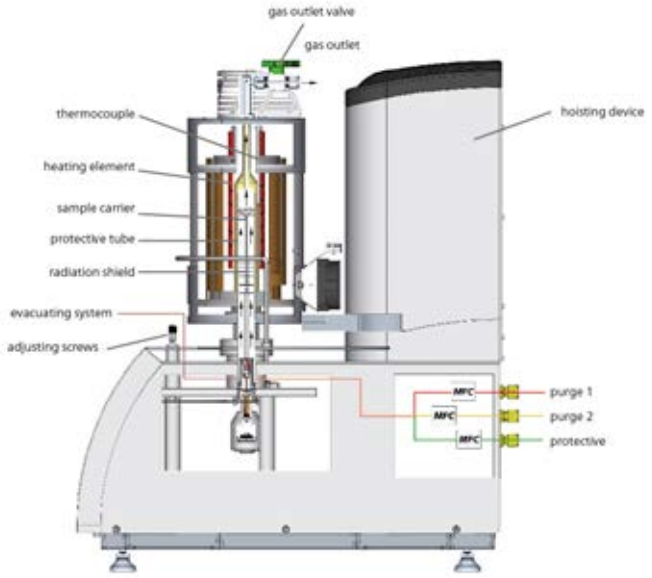

Figure 3.6: A schematic diagram of a TGA device

3.6 for a schematic diagram. The mass changes due to physical or chemical origins such as evaporation, sublimation, absorption, adsorption, reduction, and oxidation, can be detected by the TGA. The TGA can be interfaced to a MS to analyse the exhaust has composition from the TGA, and to decide if chemical reactions such as decomposition have taken place; see figure 3.7.

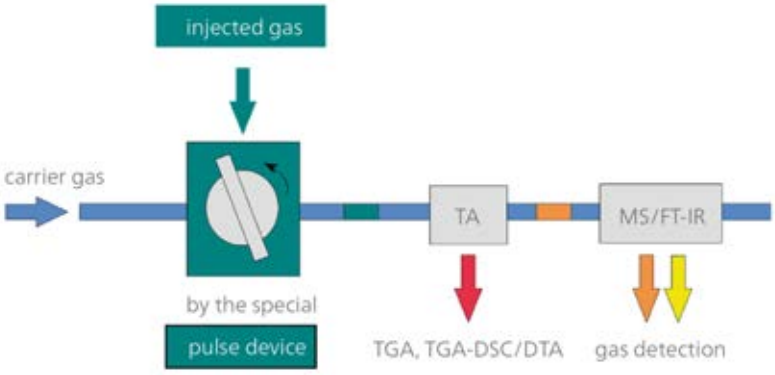

Figure 3.7: Interface between a TGA device and a MS

A Malvern Nano zetasizer was used to measure the particle size distribution of the samples. Such a device is based on the dynamic light scattering (DLS). The principle

of DLS is shown in Figure 3.8, whereby the intensity of light scattered by a particle is proportional to the particle size[188] and the particle size and the laser beam angle have an inversely proportional relationship[189]. The intensity of the scattering at a certain angle will fluctuate with time, and is detected by a photodetector. By analysing the intensity changes with a digital autocorrelator, the particle size distribution of the sample is obtained.

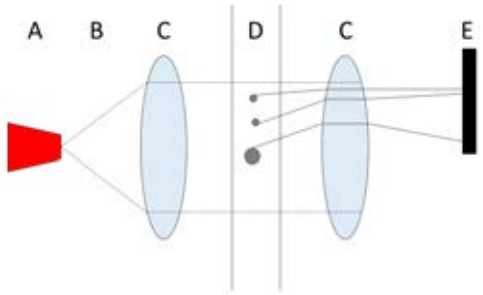

Figure 3.8: The measurement principle of zetasizer

A: Laser, B: Laser Beam, C: Focusing Optics, D: Particle Stream, E: Photodetector

3.2 MD Simulations

In this study, MD simulations were carried to compute the thermophysical properties of salt-particle mixtures. The MD simulations use the classical Newtonian mechanics, rather than the Quantum mechanics. This section explains the MD method and associated data analyses. First, the molecular structures of nitrate salts and the simulation cases are introduced. The reasons for the selection of the simulation cases are explained. The force fields that define the interactions between atoms are then explained. Finally, the software package its settings as well as the methods to calculate the thermophysical properties are given.

To perform a MD simulation, a simulation domain called simulation box needs to be defined to contain atoms of consideration, which interact with each other driven by the force field. A force field is a mathematical expression describing the dependence of the

energy of a system on the coordinates of its particles. It consists of an analytical form of the interatomic potential energy[190]. MD can be used to estimate both equilibrium and non-equilibrium properties of the system and observe molecular trajectoris according to statistic thermodynamics to be detailed in Section 3.2.4 and Section 3.2.5.

3.2.1 Geometry

Three nitrate salts were considered in the simulation study: Sodium nitrate, potassium nitrate and lithium nitrate. Water was also used to form water based nanofluids. To study the mechanism of the specific heat capacity enhancement of the salt based nanofluids, potassium chloride was investigated using MD simulation. Silicon dioxide (SiO_2) was used in the simulations as the nanoparticles.

The initial simulation box domain for pure $NaNO_3$, KNO_3 and $LiNO_3$ salts is cubic shaped (5 nm length). 3645 atoms are in the simulation boxes, respectively. Pure potassium chloride has 1728 atoms in a $4 \times 4 \times 4$ nm simulation box. The simulation box of water is $3.6 \times 3.6 \times 3.6$ nm and contains 2814 atoms. For measuring the thermal properties of bulk SiO_2, 1944 atoms in a amorphous configuration was built for simulations and the simulation box has sides of 5.3 nm each. SiO_2 nanoparticles in this study contained 39 atoms.

In a MD simulation, a salt with the different nanoparticle loadings were studied:

- 1 nanoparticle, with particle diameter of 1nm,
- 2 nanoparticles, with particle diameter of 1nm,
- 4 nanoparticles, with particle diameter of 1nm,
- 8 nanoparticles, with particle diameter of 1nm.

For water based nanofluids, the particle loadings are the same as above.

The nanoparticles were built by inserting them in a certain position of an equilibrated pure salt or water geometry without changing the size of the simulation box. Before the

insertion, a group of salt/water atoms were removed to give space for the nanoparticle. Salt/water atoms were further removed or added to keep the integrity of molecules and the charge of the system neutral. By replacing the process to insert multiple nanoparticles, the mass fraction of nanoparticles is increased accordingly. Also, the mass ratio of nanoparticle in a system is modified by changing the size of nanoparticle and keeping the simulation box unchanged. For instance, in a $NaNO_3$ based system, different configurations are obtained as shown in Figure 3.9.

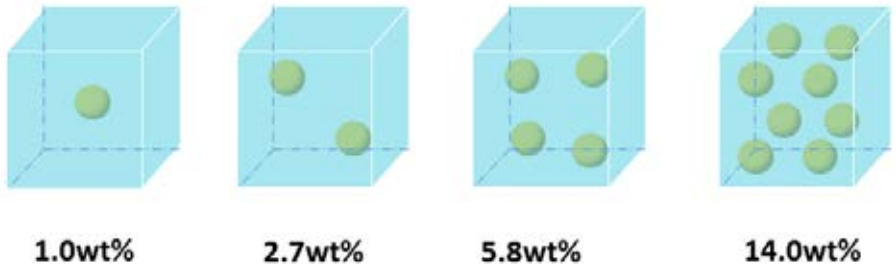

Figure 3.9: Simulation boxes for $NaNO_3$ based systems

The diameter of nanoparticles in the system containing multiple nanoparticles was 1 nm whereas the real size of nanoparticles is too big for the scale of MD simulation. As a result, a compromise has to be made for the MD simulations. As discussed before, small particles have a high specific surface area and hence more interactions between the particle atoms and salt atoms. This mismatch between MD simulations are experiments remain discussion on this will be made later on.

3.2.2 The Force Fields

Force fields relate to the intermolecular potentials. These will be discussed in this subsection. The so-called "First principles" Car-Parrinello molecular dynamics (CPMD) simulation method was been used to investigate amorphous silicon dioxide and showed to give good agreement with experimental data[191].

Buckingham potentials that were parametrized from CPMD have been shown to de-

scribe various static and dynamic properties of amorphous silica fairly reliably[192, 193]. The effective Buckingham potential used in this study is given in equation 3.4, with the parameters listed in Table 3.2. Long-range Coulombic forces are also taken into account in the study.

$$U = A_{ij}e^{-r_{ij}/\rho_{ij}} - \frac{C_{ij}}{r^6} \tag{3.4}$$

where U is the interaction energy, r is the distance between site i and j, q is the charge of the atom at site i or j, A, ρ, C are constants.

Table 3.2: Intermolecular Parameters for silicon oxide used in this study[192, 193]

Atom	q (e)	A (kcal mol^{-1})	ρ (Å)	C (kcal mol^{-1} Å^6)
O (In SiO_2)	-0.955209	15170.70	0.386	617.24
Si	1.910418	72460.64	0.351	14415.29
Si-O	-	621676.66	0.194	3406.28

There are several force field models and associated parameter sets published in the past[194, 195]. Lennard-Jones model is among the earliest, which, although popular, has not been able to reproduce the experimental crystal densities with good accuracy. The Buckingham potential with an effective parameter set was used in this study for modelling mitrate salts; see Table 3.3 and 3.4 for the parameter sets.

Lorentz-Berthelot rules[196, 197] were applied in the parameter set. The cross terms in the Buckingham potential were computed using the following mixing rules: $A_{ij} = (A_{ii}A_{jj})^{1/2}$, $C_{ij} = (C_{ii}C_{jj})^{1/2}$, and $1/\rho_{ij} = (1/\rho_{ii} + 1/\rho_{jj})/2$. The flexible nitrate intramolecular parameters were described by $V_b = k_b(r-r_0)^2$, for bonds and $V_\theta = k_\theta(\theta-\theta_0)^2$ for angles. An improper angle function of the form $V_\psi = k_\psi(\psi - \psi_0)^2$ were used to keep the nitrate species planar. Lorentz-Berthelot rules were also applied to the interactions between silicon dioxide and salt/water atoms.

Alkali halides have been investigated extensively using MD simulation methods because they are extremely corrosive at high temperatures and difficult to study experimentally. Born and Lande [198] developed a numerical model to estimate the energy of an

Table 3.3: Intermolecular Parameters for alkali nitrate salt in this study[182]

Atom	q (e)	A (kcal mol^{-1})	ρ (Å)	C (kcal mol^{-1} Å^6)
N	0.95	33652.75	0.2646	259.1
Na	1	9778.06	0.3170	24.18
K	1	35833.47	0.3370	349.9
Li	1	1149.00	0.342	1.051
O	-0.65	62142.9	0.2392	259.4

Table 3.4: Intramolecular parameters for nitrate salt in this study[b][182]

Atoms		
N-O	k_b (kcal mol^{-1} Å $^{-2}$) = 525.0	r_0 (Å) = 1.2676
O-N-O	k_θ (kcal mol^{-1} rad $^{-2}$) = 105.0	θ_0 (deg) = 120
O-N-O-O	k_ψ (kcal mol^{-1} rad $^{-2}$) = 60.0	ψ (deg) = 0.0

ionic crystal. Mayer [199] and Huggins and Mayer [200] proposed a new model based on Born and Lande's work, which considers the role of polarizability and dispersive forces on alkali halides. Fumi and Tosi [169] and Tosi and Fumi [170] proposed an empirical potential parameterizing the repulsive part of alkali halide interactions, which is called Tosi-Fumi, or TF model. The TF model was shown to give good prediction to the densities and lattice energies. The TF model has the following form with the parameter set given in Table 3.5. The TF model considers the long-range Coulombic forces.

$$U = A_{ij}e^{-r_{ij}/\rho_{ij}} - \frac{C_{ij}}{r^6} - \frac{D_{ij}}{r^8} \tag{3.5}$$

where U is the interaction energy, r is the distance between site i and j, q is the charge of the atom at site i or j, ρ, C, D are constants.

Table 3.5: Intermolecular Parameters for alkali halide salt in this study[169, 170]

Atom	q (e)	A (kcal mol^{-1})	ρ (Å)	C (kcal mol^{-1} Å^6)	D (kcal mol^{-1} Å^8)
K	1	36020.28	0.337	351.12	346.87
Cl	-1	44580.31	0.337	1799.38	3613.2
K-Cl	-	41386.58	0.337	693.74	1055.09

The simple point charge (SPC) model were used to model water molecules. Such a model is commonly used for water molecules with Coulombic interations. See equation3.6 with the parameter set given in Table3.6. In one water molecule, the OH distance and

the H-O-H angle are set rigidly as 1.0Å and 109.47 °C, respectively.

$$U = 4\varepsilon\left[\left(\frac{\sigma_{ij}}{r_{ij}}\right)^{12} - \left(\frac{\sigma_{ij}}{r_{ij}}\right)^{6}\right] \tag{3.6}$$

where U is the interaction energy, ε is the well depth and a measure of how strongly the two particles attract each other, σ_{ij} is the finite distance at which the inter-particle potential is zero, r is the distance between site i and j.

Table 3.6: Intermolecular Parameters for water in this study[201]

Atom	q (e)	ε (kcal mol^{-1})	σ (Å)
O	-0.820	0.1553	3.166
H	0.410	0	0

Because the water and silicon dioxide force fields are in different forms, Lorentz-Berthelot rules cannot be applied to water based nanofluids directly. Allen and Tildesley [202] investigated the aforementioned force field and obtained a set of parameters in the form of Lennard-Jones force field. Pham, Barisik, and Kim [203] improved the force field by changing the binding energy of oxygen and silicon to match the experimental data[204]. These parameters are listed in Table 3.7.

Table 3.7: Intermolecular Parameters between water and silica in this study[204]

Atom	ε (kcal mol^{-1})	σ (Å)
O (In water)–O (In silica)	0.1553	3.166
O (In water) –Si	0.345	2.633

3.2.3 Simulation Techniques

The well known Large-scale Atomic/Molecular Massively Parallel Simulator (LAMMPS) was used to perform all the modelling work in this study. All simulations were carried out on a high-performance-computing system, BlueBEAR II in University of Birmingham, UK.

Four dual-processors each with 8-core (16 core/node) 64-bit 2.2GHz Intel Sandy Bridge

E5-2660 were used for the simulation. NPT simulations were performed in the isothermal-isobaric ensemble using the Nosé-Hoover thermostat and barostat[10]. Simulations in the canonical ensemble were performed using the Nosé-Hoover thermostat[11]. Particle-particle-particle-mesh (pppm)[205] was used for coulombic interactions with an accuracy of 10^{-4}. The timestep was set to 1.0 femtoseconds (fs).

Initial and Boundary Conditions

The cutoff distance for the simulations were 9Å and the neighbour skin distance was set as 2.0Å. All atom pairs within a distance equal to their force cutoff plus the skin distance were stored in the pairwise neighbour list. Given a specific temperature, the initial velocities were generated in a uniform distribution. Periodic boundary conditions were applied in this study so that particles could interact across the boundary, exiting from one end of the box and re-entering from the other end.

Integration Scheme

Throughout this work the integration algorithms were based on Velocity-Verlet (VV) integrator[206], which is both simple and time reversible[202]. The VV algorithm consists of two stages: VV1 and VV2. The first stage is to advance the velocities to $t + (1/2)\Delta t$ by integration of the force. Then the positions are advanced to a full step $t + \Delta t$ using the new half-step velocities. Position ($\vec{r}$), velocity ($\vec{v}$) and acceleration ($\vec{a}$) at time (t) are required at the first stage are as follows:

$$\vec{v}\big(t + \frac{1}{2}\Delta t\big) = \vec{v} + \frac{1}{2}\vec{a}(t)\Delta t \tag{3.7}$$

$$\vec{x}\big(t + \Delta t\big) = \vec{x}(t) + \vec{v}\big(t + \frac{1}{2}\Delta t\big)\Delta t \tag{3.8}$$

Between VV1 and VV2, the acceleration at time $t + \Delta t$ is derived from the interaction potential using $\vec{x}(t + \Delta t)$.

$$a(t+\Delta t) \longleftarrow \vec{x}(t+\Delta t) \tag{3.9}$$

The second stage is to calculate a full step velocity using the new acceleration and half-step velocities.

$$\vec{v}(t+\Delta t) = \vec{v}(t+\frac{1}{2}\Delta t) + \frac{1}{2}\vec{a}(t+\Delta t)\Delta t \tag{3.10}$$

Energy Minimization and Equilibration

Energy minimization is a process of finding an arrangement in the system where, according to a given set of force field, the net potential force on each atom is at its minimum value. This is for avoiding un-physical states such as overlapping atoms to occur. The Polak-Ribiere version of the conjugate gradient (CG) algorithm was used in this work for the energy minimisation. Figure 3.10 shows schematically the procedure, which includes an initial guess and interations.

The conjugate gradient method methioned above is an algorithm whereby a particle moves towards $\vec{v}_k$ is derived from the gradient at point k and $\vec{v}_{k-1}$:

$$\vec{v}_k = -\vec{g}_k + \gamma_k \vec{v}_{k-1} \tag{3.11}$$

where γ is a scalar given by:

$$\gamma_k = \frac{\vec{g}_k \cdot \vec{g}_k}{\vec{g}_{k-1} \cdot \vec{g}_{k-1}} \tag{3.12}$$

The following conditions must be satisfied during the calculation:

$$\begin{aligned} \vec{g}_i \cdot \vec{g}_j &= 0 \\ \vec{v}_i \cdot U''_{ij} \cdot \vec{v}_j &= 0 \\ \vec{g}_i \cdot \vec{v}_j &= 0 \end{aligned} \tag{3.13}$$

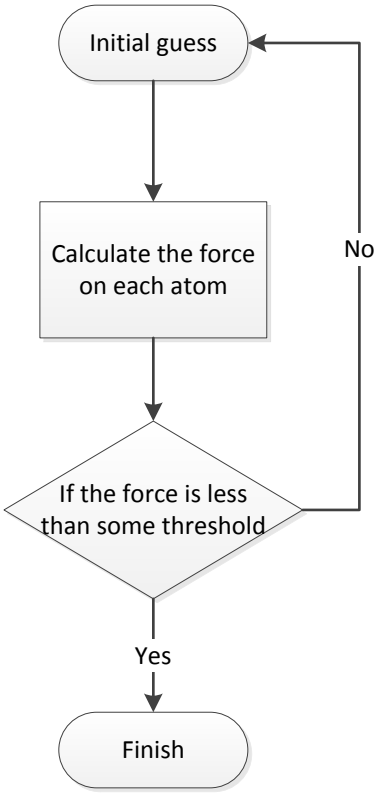

Figure 3.10: Procedure of energy minimization

The simulation system was equilibrated in a series of steps in advance of the simulation to ensure the physical properties remain as statistically invariant as possible. An appropriate configuration of system a is brought to equilibrium by letting the system relax for at least 100 ps. The equilibration is terminated when the internal energy, temperature, pressure are observed to fluctuate about a stationary average value in a NVT simulation and when the internal energy, temperature, pressure and volume are varying within a certain range in a NPT simulation.

3.2.4 Equilibrium Properties

In this subsection, equilibrium properties are defined and methods of their caculations are given.

Density

The density in this work was obtained by dividing the mass of all the atoms in the system by the volume of the simulation box in a equilibrated NPT simulation.

Radial Distribution Function and Number Density

The physical meaning of the radial distribution function (RDF) is shown in Figure 3.11. The grey dot is one particle (atom) called "reference particle". The number of particles in the space from the diameter of r to r + d_r is dN. RDF is then defined as:

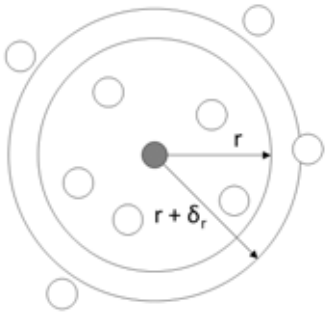

Figure 3.11: Schematic diagram of RDF

$$\rho g(r) 4\pi r^2 = dN \tag{3.14}$$

where ρ is the number density of the system, $g(r)$ is the radius distribution function. Equation 3.14 can be rearranged as:

$$g(r) = \frac{dN}{\rho 4\pi r^2 dr} \tag{3.15}$$

The RDF represents the difference between local density and bulk density. The density near the reference particle is different from the average density and the RDF fluctuates along the radial direction. The RDF will be close to 1 at the distance far away from the reference particle. In this work, the RDF is calculated using the following equation.

$$g(r) = \frac{1}{\rho 4\pi r^2 \delta_r} \frac{\sum_{t=1}^{T} \sum_{j=1}^{N} \Delta N(r \to r + \delta r)}{N \times T} \tag{3.16}$$

where

N = total number of particles,

T = total time(steps) during the simulation,

The RDF is used mainly for two reasons. First, it is useful to study the structure of the system and check the state of phase of the substance. Second, it is related to many thermodynamic properties. Figure 3.12 illustrates the RDF for different states of matters [207, 208].

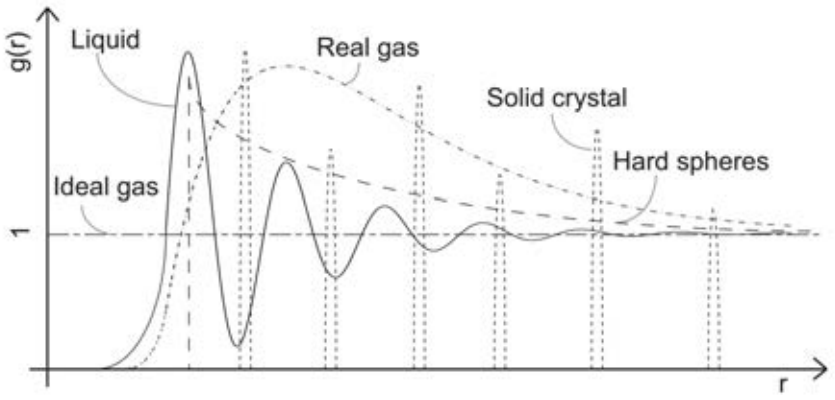

Figure 3.12: RDF of different states of matter

The packing information adjacent to a nanoparticle is of specific interset in this study. As a consequence, the number density and the specific particle number per unit volume around the centre of a nanoparticle is calculated. The specific number density was computed in the domain between two spherical shells:

$$n = \frac{\Delta N}{\Delta V} \tag{3.17}$$

From the number density, the normalised number density can be obtained, which is defined as the relative number density of one atom (n) over the number density of the atom at a very long distance

Specific Heat Capacity

The specific heat capacity was calculated by examining the change to the internal energy due to a change to temperature[8]:

$$C = \left(\frac{\partial E}{\partial T}\right)_V = \frac{1}{k_B T^2}\langle(\delta\varepsilon)^2\rangle \tag{3.18}$$

where

$\langle(\delta\varepsilon)^2\rangle = \langle\varepsilon^2\rangle - \langle\varepsilon\rangle^2$

E is the internal energy,

T is the temperature,

V is the volume,

k_B is the Boltzmann constant.

3.2.5 Dynamical Properties

Dynamical properties such as thermal conductivity for nitrate salt and the nanofluids based on it are discussed in this work. The numerical evaluation of transport coefficients of fluids by MD can proceed in various ways. Early calculations were based, for the most part, on Green-Kubo (GK) relations at equilibrium molecular dynamics (EMD)[209–211]. With this method any transport coefficient μ is obtained from an appropriate time-correlation function $\rho_\mu(t)$.

$$\mu = c_\mu \int_0^\infty dt \rho_\mu(t) \tag{3.19}$$

where the GK method calculates the decay of fluctuations near equilibrium in properties of the material and it depends on the evaluation of the microscopic current at a time t subsequent to an initial time 0. The EMD methods have a high strong system-size dependence and suffer from a weak signal-to-noise ratio. Non-equilibrium molecular dynamics (NEMD) was developed to overcome the problems. At first it was to mimic laboratory

experiments using the computer to impose non-equilibrium boundary conditions on a system[212–214]. Müller-Plathe [9, 215] developed a reverse non-equilibrium molecular dynamics (RNEMD) method and thermal conductivity computing. In this method, the total energy as well as the total linear momentum can be conserved, so simulations can be performed in a microcanonical ensemble without an additional thermostat. Moreover, it is simple to implement and generate intermediate data which is robust and easy to analyse. In this work, the RNEMD method was used to calculate thermal conductivity.

The thermal conductivity (λ) macroscopically is defined byMüller-Plathe [9]:

$$J = -\lambda \nabla T \tag{3.20}$$

where ∇T is the gradient of the temperature, T, J is the resulting heat flux vector. Instead of interchanging the momentum, the velocities in all three (x, y and z) directions are swapped between atoms with the minimum (cold) and maximum (hot) kinetic energy to create a temperature difference in the system. A physical heat flux is imposed to balance the temperature difference between y=0 and y=l/2. When the steady state is reached, the thermal conductivity is calculated as

$$\lambda = -\frac{\sum\limits_{transfers} \frac{m}{2}(v_h^2 - v_c^2)}{2tL_xL_z\langle \partial T/\partial y \rangle} \tag{3.21}$$

where t is the simulation time. h and c refer to the hot and cold particle of identical mass m whose velocities are swapped. Temperature T in a certain bin is given by

$$T_k = \frac{1}{3n_k k_b} \sum_{i \in k}^{n_k} m_i v_i^2 \tag{3.22}$$

where n_k refers to atom number in bin k. m and v are masses and velocities. k_b is Boltzmann's constant.

CHAPTER 4

RESULTS AND DISCUSSION: THERMOPHYSICAL PROPERTIES OF SALT BASED NANOSUSPENSIONS

This chapter discusses the thermophysical properties observed in simulation and experiments.

Section 4.1 shows the thermophysical properties of pure salts in experiments and simulations. 4.2 discusses the specific heat capacity of nano-suspensions observed. 4.3 exhibits the changes of melting point and latent heat introduced by adding nanoparticles. 4.4 provides the conductivity data of nano-suspensions.

4.1 Nitrate Salt Characterisation

4.1.1 Experimental results

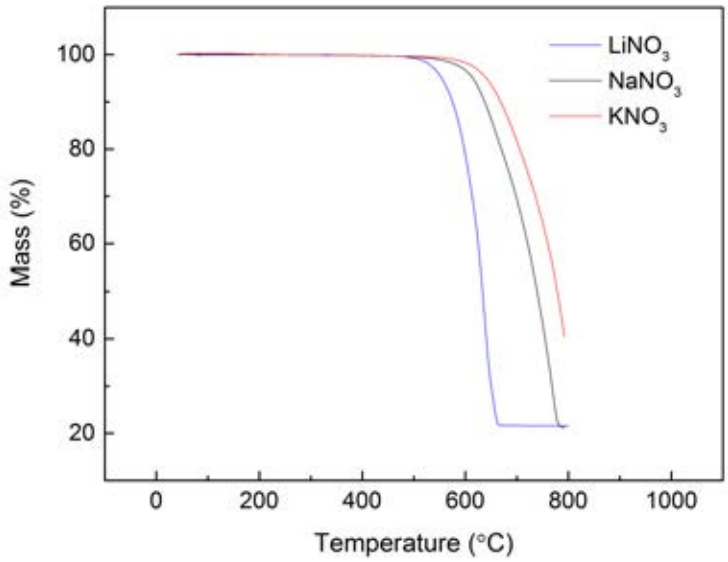

Figure 4.1: Thermogravimetric analysis of three nitrate salts

All three nitrate salts decomposed at high temperature and the exhaust gas was analysed. As is shown in Figure 4.1, the salts were heated to 800 °C in the atmosphere of helium. Significant mass loss was occurred in $LiNO_3$ at 557 °C, which indicated the beginning of the decomposition. Considerable mass loss of $NaNO_3$ was observed at 607 °C. At 649 °C, mass decrement was observed in KNO_3. In order to avoid the decomposition and insure the repeatability of our experiments, the temperatures in the corresponding tests in this work were set much lower than the decomposition temperature obtained. By analysing the exhaust gas during the decomposing process using the quadrupole mass spectrometer, oxygen, nitrogen, nitrogen oxide and nitrogen dioxide were detected. It indicates the following reactions during the decomposition.

$$2\,MNO_3 \longrightarrow 2\,MNO_2 + O_2$$

$$2\,MNO_3 \longrightarrow 2\,MO + N_2 + \tfrac{5}{2}\,O_2$$

$$2\,MNO_2 \longrightarrow M_2O + NO + NO_2$$

As is shown in Figure 4.2, the specific heat capacity of $NaNO_3$, KNO_3 and $LiNO_3$ were measured in the liquid form. The salts were tested while melted and not decomposed in the temperature range which was based on the results obtained in Section 4.1. In the temperature range from 320 to 360 °C, the specific heat capacity of $NaNO_3$ was around 1.62 J K^{-1} g^{-1} with the standard deviation obtained below 4%. The specific heat capacity of $LiNO_3$ increased from 1.86 J K^{-1} g^{-1} at 275 °C to 1.94 J K^{-1} g^{-1} at 300 °C with the standard deviation below 4%. The specific heat capacity value of KNO_3 was observed around 1.31 J K^{-1} g^{-1} with the standard deviation 4% from 345 °C to 370 °C. These values obtained are in good agreement with the published results[2, 55, 216], which indicates that the method of measurement and the calibration of the equipment are correctly done.

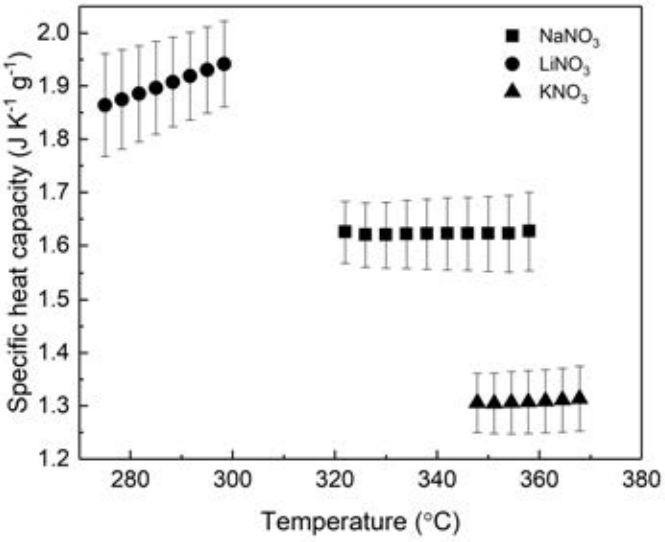

Figure 4.2: Specific heat capacity of pure salts

The melting point and latent heat of the salts are shown in Figure 4.3. The results are in good agreement with the published literature[55].

4.1.2 MD Simulation Results

Table 4.1 compares computed and experimental density values and reasonable predictions for the densities were achieved.

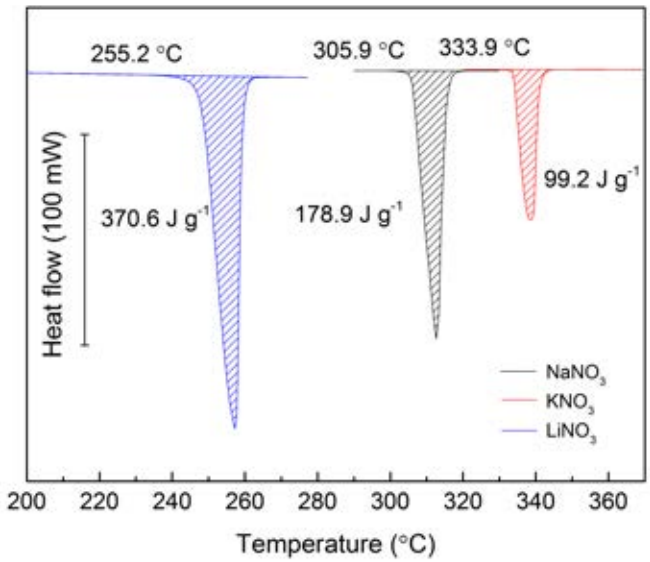

Figure 4.3: Melting point and latent heat of three nitrate salts

Table 4.1: Comparison of experimental and simulated density results (g cm^{-3})

	Experimental	Simulation
$NaNO_3$ at 700K	1.81[217]	1.78
$LiNO_3$ at 700K	1.66[218]	1.73
KNO_3 at 700K	1.75[218]	1.70
SiO_2 at 300K	2.19	1.66
Water at 353K	0.97	0.92

In our simulations, the simulation and experimental specific heat capacity results of salt are shown in Table 4.2 and it indicated that favourable specific heat capacity results were obtained in the simulation.

Table 4.2: Comparison of experimental and simulated specific heat capacity results (J K^{-1} g^{-1})

	Literature	Simulation
$NaNO_3$ at 700K	1.67[55]	1.52
$LiNO_3$ at 700K	2.06[55]	2.13
KNO_3 at 700K	1.38[55]	1.32
SiO_2 at 300K	0.85	1.01
Water at 353K	4.39	4.18

4.2 Specific Heat Capacity of Nanosuspensions

4.2.1 Anomalous Specific Heat Capacity Enhancement in the MD Simulation Results

Experimental results of the enhancement of specific heat capacity in molten salt has been widely reported while the simulation data is lacking. In this work MD simulations of nitrate salt based nanofluids containing different concentrations of nanoparticles were performed. The specific heat capacity of these suspension were obtained and analysed.

As mentioned before, nanoparticles with 1nm diameter were used, which are much smaller than the particles used in the experiments. This is due to two main reasons. First, particles used in the experiments are far too large for MD simulation using the computing resources available. Second, the use of 1 nm particles gives a very large specific surface area between nanoparticles and the base liquid, which is believed to be one of the reasons that gives enhancement of the thermophysical properties of salt based nanofluids. In addition, the use of 1nm nanoparticles in experiments is unrealistic due to aggregation of the particles, as a result of strong interparticle attraction forces. One may ask why 1nm rather than 2 nm particles. The choice is indeed a bit arbitrary, and this is not the most important as the aim of this part of work is to demonstrate potential enhancement, and then explore the underlying mechanism of the enhancement.

Although the experimental work was performed over a temperature range, the simulation of work was carried out at 700K at which all the salts studied were in the liquid state. This is mainly due to computing reasons.

As mentioned above, the goal of the MD simulation was to understand the behaviour of nanoparticles in the salt. The simulations were done with much smaller particles, but also at higher concentrations than normally used in nanofluids.

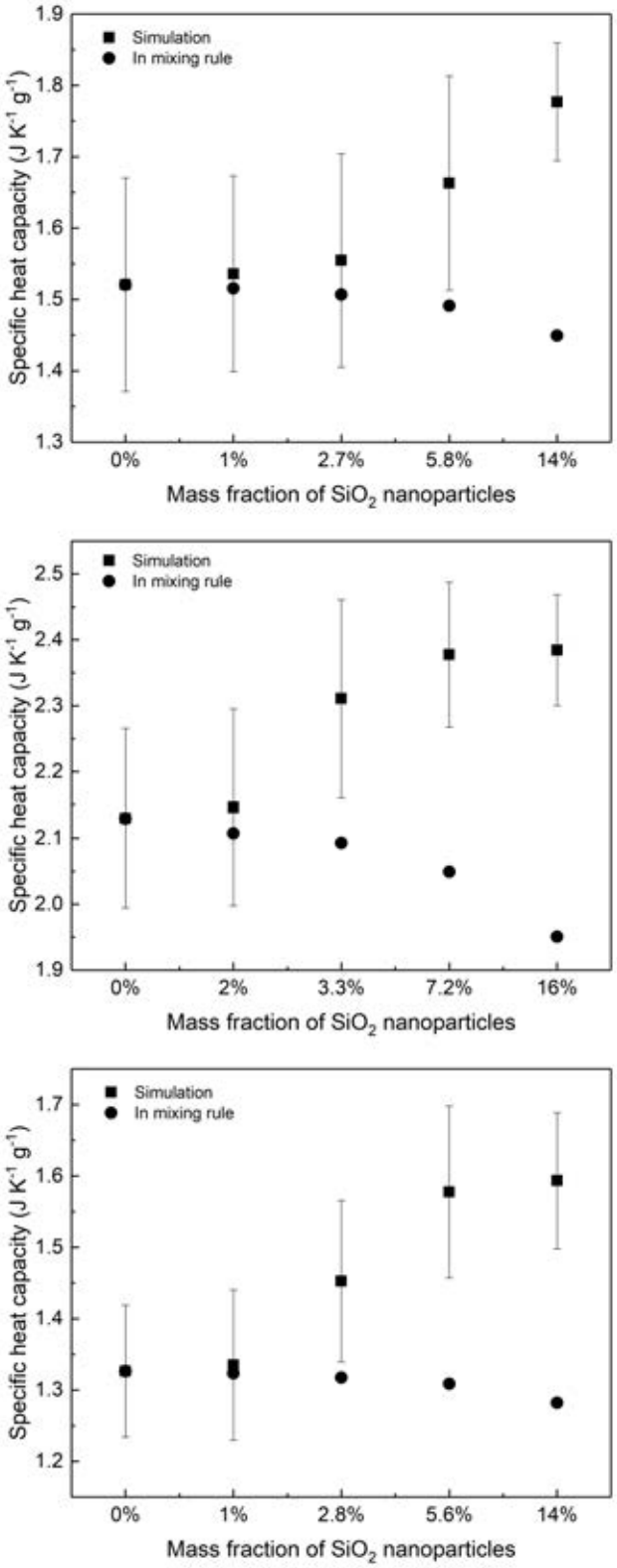

Figure 4.4: Specific heat capacity of nitrate salts based nanofluids at 700K in simulations and comparison with the mixing rule

A: $NaNO_3$ based nanofluids; B: $LiNO_3$ based nanofluids; C: KNO_3 based nanofluids. The theoretical value was calculated from the thermal equilibrium model (the mixing rule)[4]

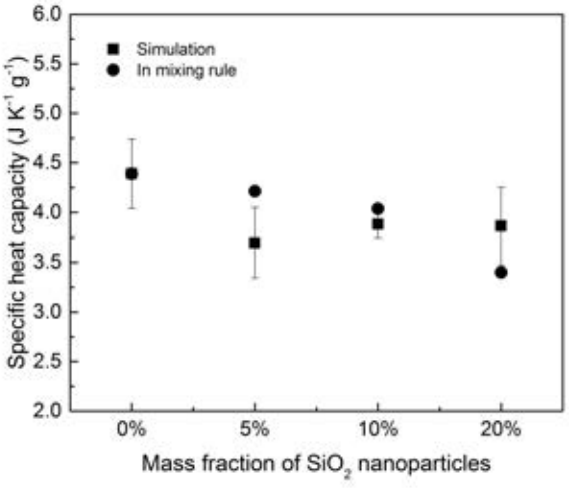

Figure 4.5: Specific heat of water based nanofluids from simulations and comparison with the mixing rule

Figure 4.4 shows the results for comparison purposes, specific heat capacities calculated from the thermal equilibrium model (the mixing rule)[4] are also included in the figure. One can see that the thermal equilibrium model predicts that the specific heat capacities of all the three salts based nanofluids decrease with increasing SiO_2 concentration. This is because the specific heat capacity of SiO_2 is lower than that of the salts. The simulation results, however, show contradiction to the equilibrium model. A significant enhancement of the specific heat capacity is observed in nanofluids due to the introduction of the SiO_2 nanoparticles for all three salts and the enhancement is particle concentration related. For $NaNO_3$ salts, an addition of 1% SiO_2 gives a 3% enhancement whereas the specific heat capacity increases by 18% (from 1.51 to 1.79 J K^{-1} g^{-1}) while 14% SiO_2 nanoparticles. Similar results are observed for KNO_3 and $LiNO_3$ based nanofluids and a maximum enhancement of 22.1% and 11.6% was observed, respectively. For KNO_3 nanofluids, the specific heat capacity increases by 20% for a SiO_2 concentration of 6%. The modelling results are consistant with reported experimental results in [4, 7, 152, 153, 158, 160, 162]. But, as mentioned above, disagree with equilibrium theory (Equation 2.5).

Although enhancement in the specific heat capacity has been observed for nitrate salts due to addition of SiO_2 nanoparticles, this does not happen to water based nanofluids

as illustrate in Figure 4.5. The specific heat capacity of water decreases with increasing SiO_2 concentration. This agrees with the equilibrium mixing theory. These results also agree with the experimental data (see in Section 4.2.2). For the above, one could conclude that the effect of nanoparticles on the specific heat capacities depends on the base fluid properties. An explanation of these seemingly contradicting results will be discussed further in Chapter 5.

4.2.2 Experimental Results of Specific Heat Capacity of Nanofluids

$NaNO_3$ based nanofluids

The specific heat capacity of $NaNO_3$ based nanofluids was studied with different sized SiO_2 particles.

Figure 4.6 A shows the results for the 15-20nm SiO_2 at 360 °C (633K). One can see enhancement occurs at all particle concentrations and the concentration dependence is non-monotonous. At low SiO_2 concentrations, the specific heat capacity increase with increasing particle concentration. The enhancement peaks at a particle concentration of $\sim$1%, beyond which, a decrease in the enhancement is seen with a further increase in SiO_2 concentration. Temperature has been found to give a relatively weak effect on the specific heat capacity enhancement as illustrated in Figure 4.6 B.

Figure 4.7 A demonstrates the specific heat capacities results with 20-30nm SiO_2 particles at 360 °C. With 0.5% nanoparticles in the salt, the specific heat capacity reached 1.73 J K^{-1} g^{-1}, giving an enhancement of 6% with respect to the pure salt. A decreasing tendency occurs with further increase in the SiO_2 nanoparticles concentration. This is similar to the results shown in Figure 4.6 A for the 15-20nm SiO_2 particles except that the peak specific heat capacity occurs at 0.5% SiO_2 concentration. The temperature appears to have little effect on the enhancement as shown in Figure 4.7 B, again, similar to the results shown in Figure 4.6 B for the 15-20nm particles.

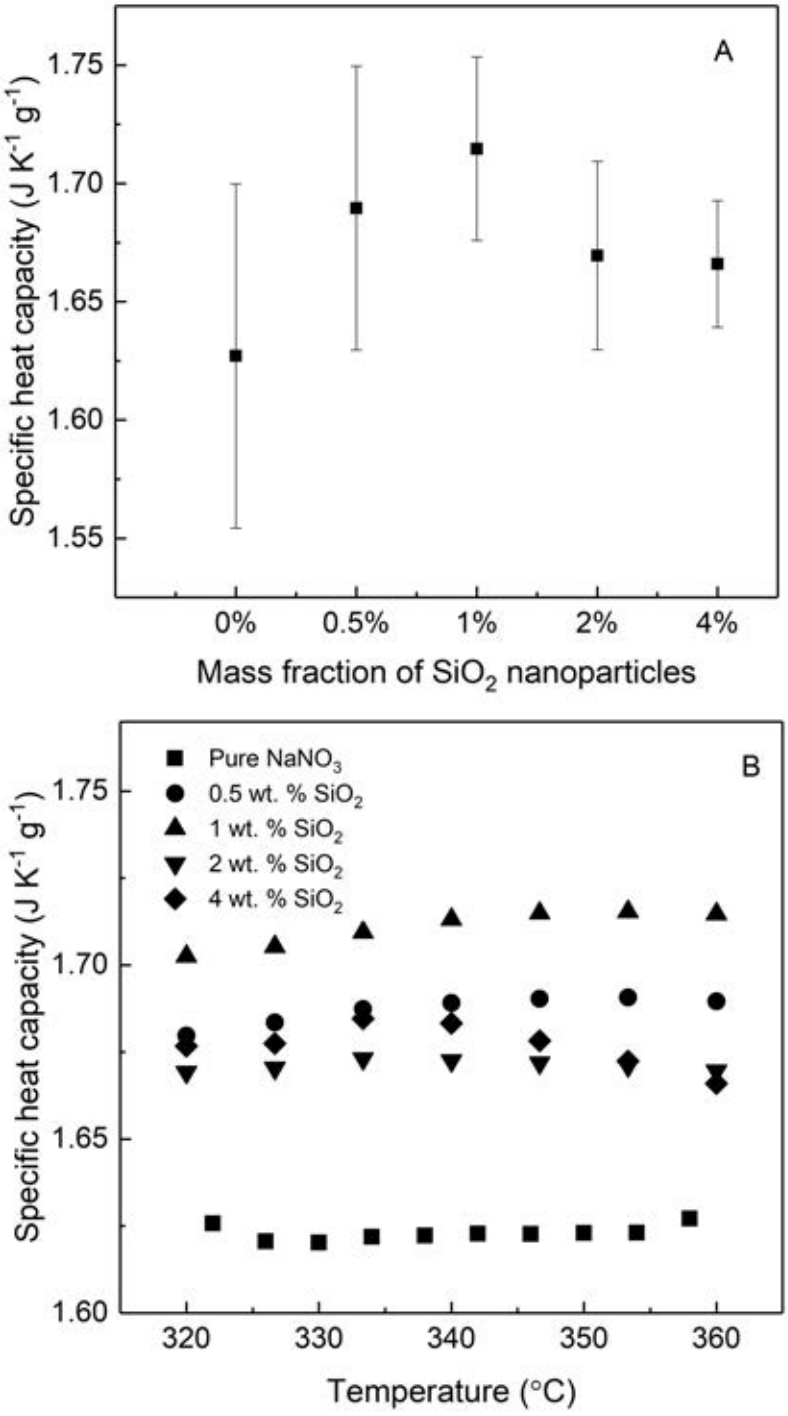

Figure 4.6: Specific heat of $NaNO_3$ based nanosuspensions with 15-20nm SiO_2 nanoparticles

A Specific heat capacity of nanosuspensions at 360 °C; B Specific heat capacity against temperature of nanosuspensions with different fraction of nanoparticles

A significant enhancement of specific heat capacities was observed at 360 °C for nanofluids containing 60-70 nm nanoparticles as shown in Figure 4.8 A. The enhancement is sig-

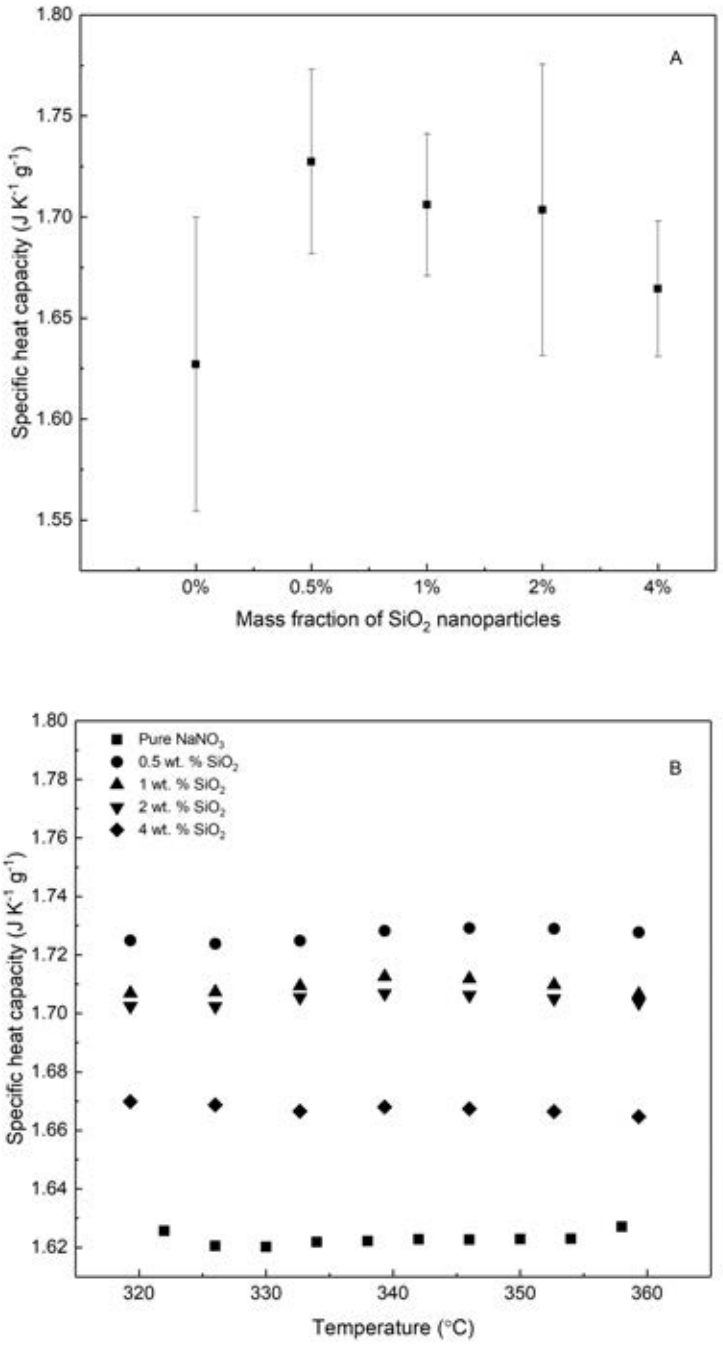

Figure 4.7: Specific heat of $NaNO_3$ based nanosuspensions with 20-30nm SiO_2 nanoparticles

A: Specific heat capacity of nanosuspensions at 360 °C; B: Specific heat capacity against temperature of nanosuspensions with different fraction of nanoparticles

nificant under all concentrations. However, the peak enhancement observed for 15-20nm and 20-30nm particles did not occur and the exact reason requires further investigation.

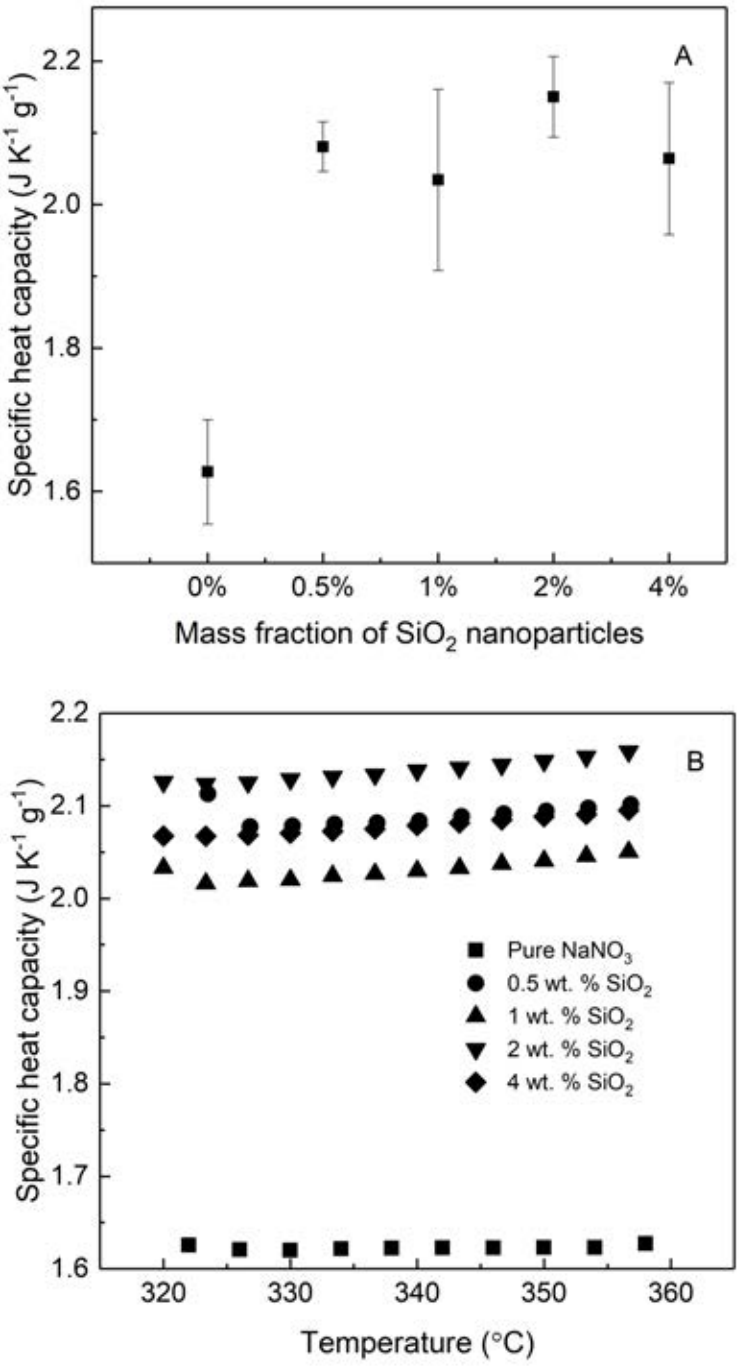

Figure 4.8: Specific heat of $NaNO_3$ based nanofluids with 60-70nm SiO_2 nanoparticles

A: Specific heat capacity of nanofluids at 360 °C; B: Specific heat capacity against temperature of nanofluids with different fraction of nanoparticles

A comparison of Figure 4.8 A with Figure 4.6 A and 4.7 A suggests that the enhancement due to the addition of 60-70nm SiO_2 particles is significantly higher than the

other two cases and particles concentration give little effect considering the error bars. Figure 4.8 B shows the temperature dependence of the specific heat capacity for different particle concentrations. A weak temperature dependence is apparent from the figure and particle concentration does not seem to have much effect on the temperature dependence, in agreement with the above analysis.

The results for the 1-5 μm particles are shown in Figure 4.9 A. One can see that the specific heat capacity of the salt containing micron sized particles is only slightly enhanced at low concentrations of 0.5% or 1%. A further increase in the particle concentration shows a decreasing trend at 4% the specific heat capacity is even lower than that of the pure salt. Figure 4.9 B demonstrates the temperature dependence of the specific heat capacity over a temperature range at 320 °C - 360 °C.

A fairly strong temperature dependence is apparent compared with the case shown in Figure 4.8 B, 4.7 B and 4.8 B for nanosized SiO_2 particles. Again, the exact reasons for this requires further investigation.

$LiNO_3$ based nanofluids

Figure 4.10 A displays the specific heat capacities of the nanofluids containing 15-20nm SiO_2 as a function of particle concentration at 300 °C, whereas the temperature dependence is shown in Figure 4.10 B. One can see that the addition of 0.5% 15-20nm SiO_2 gives the highest specific heat capacity (2.10 J K^{-1} g^{-1}, Figure 4.10 A). This is equivalent to an enhancement of around 8%. With an increase in the nanoparticle concentration, the specific heat capacity decreases.

Temperature has a stronger effect on the specific heat capacity of the $LiNO_3$ salt than that of $NaNO_3$ salts (comparing Figure 4.6 B, 4.7 B, 4.8 B and 4.9 B with Figure 4.10 B), and the addition of nanoparticles reduces the temperature dependence.

The specific heat capacity data of $LiNO_3$ based nanofluids with 20-30nm nanoparticles are shown in 4.11. A significant enhancement can be observed for nanofluids containing 0.5%, 1% and 2% 20-30nm SiO_2 particles and particle concentration does not seen to give

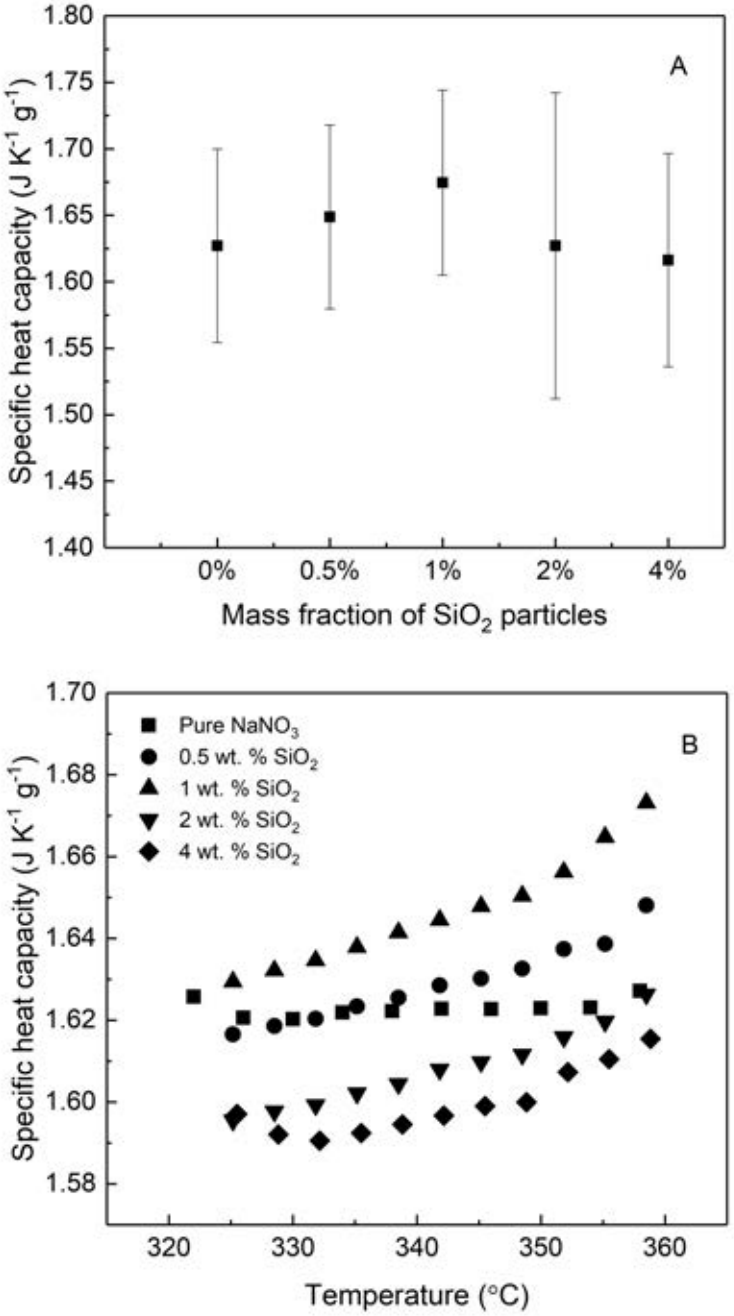

Figure 4.9: Specific heat of $NaNO_3$ based suspensions with 1-5μm SiO_2 particles

A: Specific heat capacity of suspensions at 360 °C; B: Specific heat capacity against temperature of mixtures with different fraction of particles

much influence. The highest specific heat capacity is ~2.14 J K^{-1} g^{-1} at 0.5% particle concentration. At 4% particle concentration, the specific heat capacity was measured to

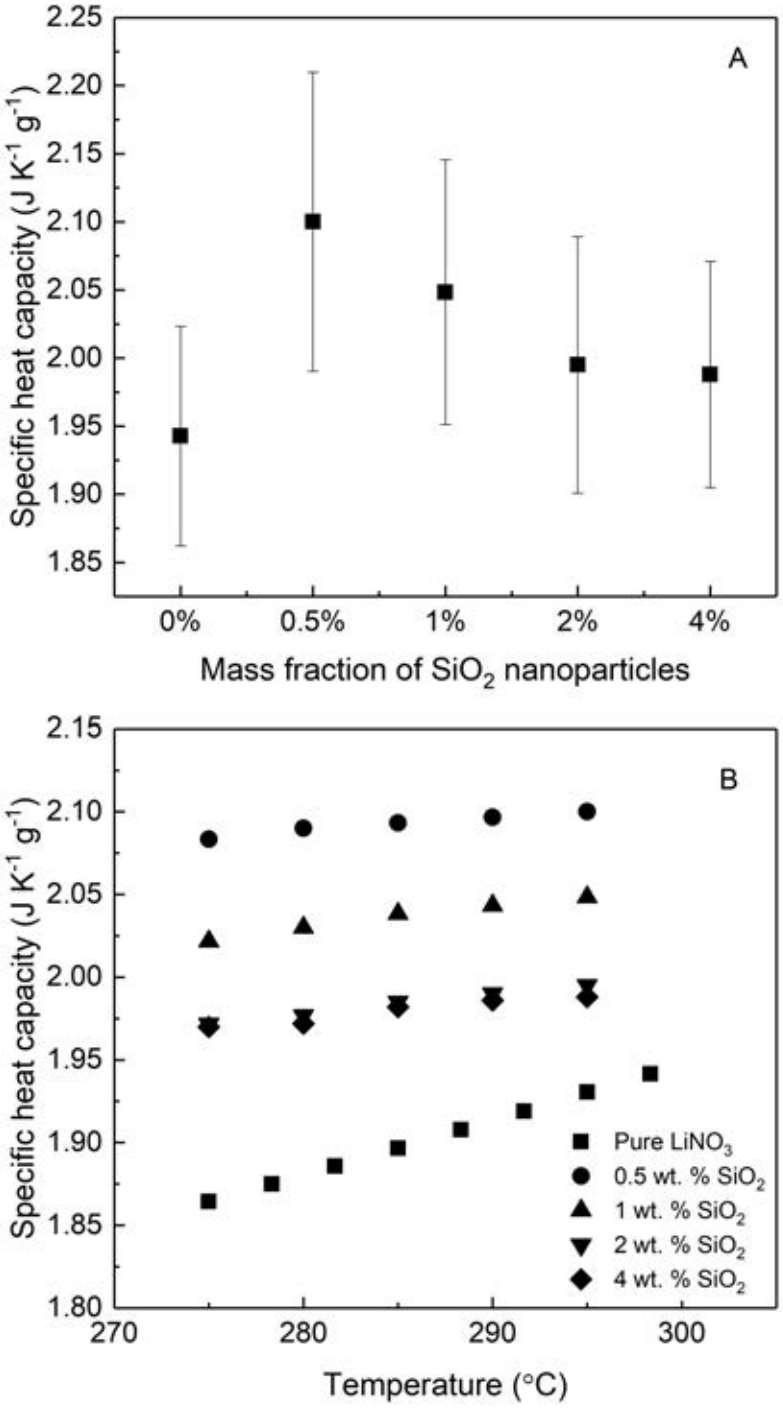

Figure 4.10: Specific heat of $LiNO_3$ based nanofluids with 15-20nm SiO_2 nanoparticles

A: Specific heat capacity of nanofluids at 300 °C; B: Specific heat capacity against temperature of nanosuspensions with different fraction of nanoparticles

be 1.96 J K^{-1} g^{-1}, which suggests no enhancement compared with the pure $LiNO_3$. The temperature dependence for this range of particle size is similar to that for the 15-20nm

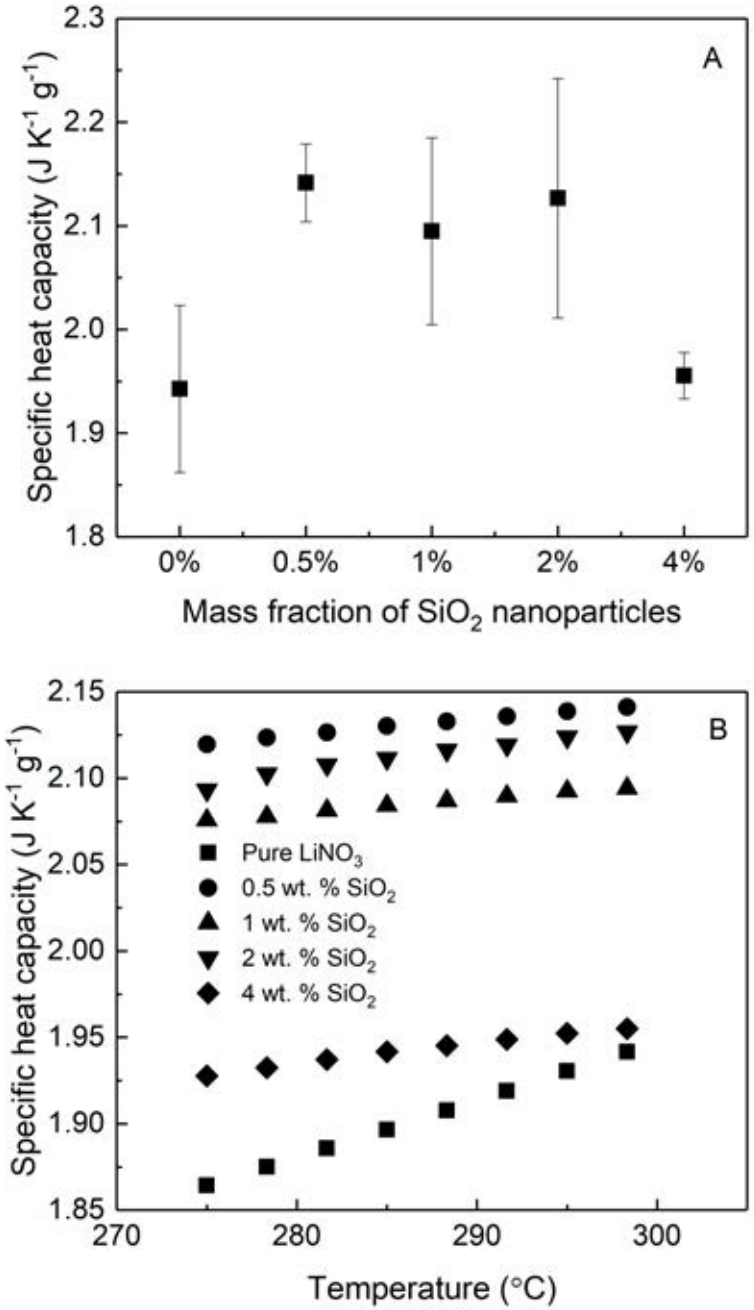

Figure 4.11: Specific heat of $LiNO_3$ based nanofluids with 20-30nm SiO_2 nanoparticles

A: Specific heat capacity of nanofluids at 300 °C; B: Specific heat capacity against temperature of nanosuspensions with different fraction of nanoparticles

particles as shown in Figure 4.11 B.

Figure 4.12 A presents the specific heat capacity of nanofluids with 60-70nm nanopar-

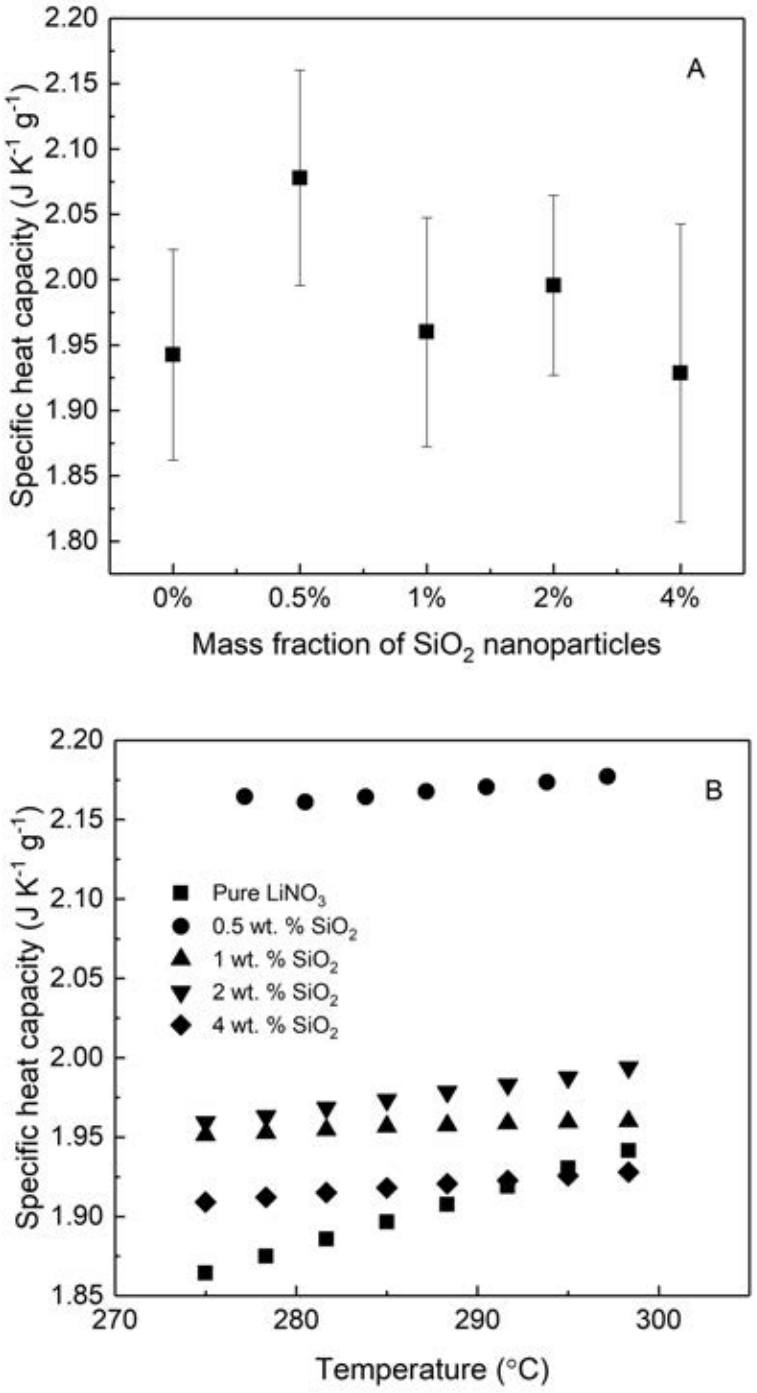

Figure 4.12: Specific heat of $LiNO_3$ based nanofluids with 60-70nm SiO_2 nanoparticles

A: Specific heat capacity of nanofluids at 300 °C; B: Specific heat capacity against temperature of nanofluids with different fraction of nanoparticles

ticles at 300 °C. An addition of 0.5% SiO_2 gives an enhancement of the specific heat capacity by 7.2% compared with the pure salt at 300 °C; an addition of 2% nanoparticles

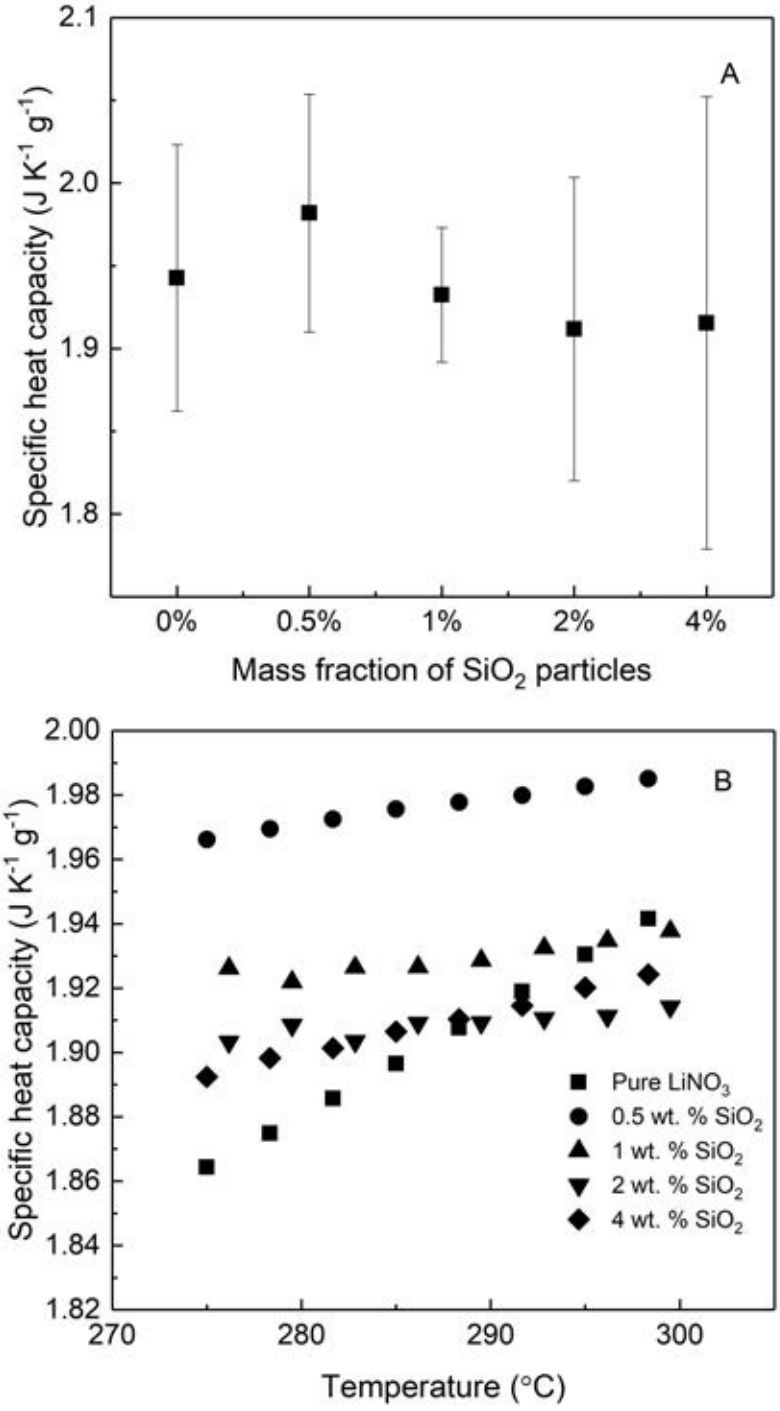

Figure 4.13: Specific heat of $LiNO_3$ based mixtures A with 1-5μm SiO_2 particles

A: Specific heat capacity of mixtures at 300 °C; B: Specific heat capacity against temperature of mixtures with different fraction of particles

leads to 0.05 J K^{-1} g^{-1}; whereas the sample with 1% and 4% nanoparticles show no enhancement, and the specific heat capacity of the 4% nanofluid is even slightly lower than

than of the pure salt. Considering the error bars, except the 0.5% sample, enhancement in the specific heat capacity is not apparent for the rest of the samples a 300 °C. The temperature dependence of the specific heat capacity of the nanofluids containing 60-70nm nanoparticles is shown in Figure 4.12 B. Enhancement of the heat capacity is seen at all particle concentrations at temperature below ∼290 °C. At temperatures above ∼290 °C, the 4% nanofluid does not give any enhancement. An inspection of Figure 4.12 B also suggests that the addition of nanoparticles, reduces the temperature dependence of the heat capacity as demonstrated by the slope of the data.

Figure 4.13 A presents the specific heat capacity data of $LiNO_3$ salt containing 1-5μm SiO_2 particles at 300 °C. At such a temperature, only the 0.5% sample gives an enhancement although the error bar is significant, whereas samples with 1-4% SiO_2 particles show no or even negative enhancement.

Figure 4.13 B displays the temperature dependence of the specific heat capacity. One can see that at temperature lower than ∼275 °C, the specific heat capacities of all suspensions are higher than that of the pure salt suggesting an enhancement. At temperature over ∼275 °C, except for 0.5% suspension, the remaining samples show little or even negative enhancement in the specific heat capacity. The above data also suggests that the addition of particles reduces the temperature dependence of the specific heat.

KNO_3 based suspensions

Specific heat capacity of nanosuspensions is shown in Fig. 5. With the introduction of nanoparticles, all nanosuspensions show a higher specific heat that compared to the pure KNO_3. I compared the specific heat capacity of different samples at 360 °C (Fig. 5A) to demonstrate the impact of nanoparticle fraction on the specific heat capacity. The specific heat capacity of KNO_3 pure salt was obtained as 1.40 J K^{-1} g^{-1}. By introducing 0.5 wt% SiO_2 nanoparticles, the specific heat capacity was observed to be enhanced to about 1.5 J K^{-1} g^{-1}. With 1 wt% SiO_2, the specific heat capacity of the nanosuspension was enhanced to 1.62 J K^{-1} g^{-1}, which reintroduces the phenomenon observed in the

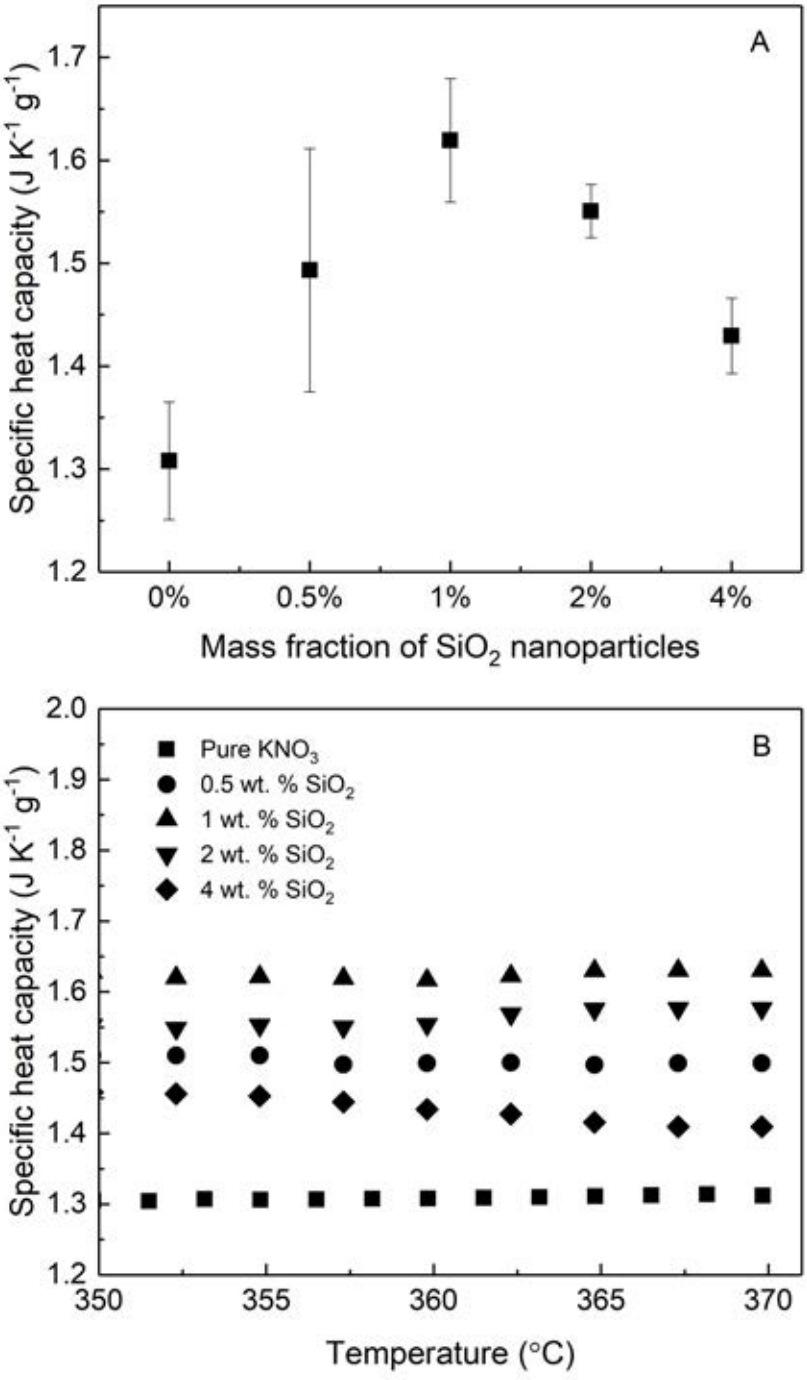

Figure 4.14: Specific heat of KNO_3 based nanosuspensions with 15-20nm SiO_2 nanoparticles

A: Specific heat capacity of nanosuspensions at 360 °C; B: Specific heat capacity against temperature of nanosuspensions with different fraction of nanoparticles

simulations. However, when the nanoparticle fraction increases more, the specific heat capacity decreases, which did not happen in the simulation. While nanoparticle fractions

increased to 2 wt%, the specific heat capacity becomes 1.56 which is lower than that of the 1 wt% sample. Keep increasing the nanoparticle fraction to 4wt% decreases the specific heat capacity to 1.43 J K^{-1} g^{-1}. The specific heat capacity of KNO_3 and nanosuspensions based on it along the temperature range from 350 to 370 are shown in Fig. 5B. The specific heat capacity of the pure salt, 0.5 wt%, and 1 wt% nanosuspensions are stable along the temperature range. The nanosuspension with 2 wt% nanoparticles shows an increasing tendency in specific heat capacity while the temperature increases. The specific heat capacity is 1.58 J K^{-1} g^{-1} and 1.55 J K^{-1} g^{-1} at 366 °C and 352 °C, respectively. The specific heat capacity of the nanosuspension with 4 wt% SiO_2 nanoparticles shows a downward tendency through the temperature range and at 366 °C reaches 1.41 J K^{-1} g^{-1} which is 0.4 J K^{-1} g^{-1} lower than that at 352 °C.

The data for 20-30nm nanoparticles are presented in Figure 4.15. For suspensions with 0.5% 20-30nm nanoparticles, the specific heat capacity of KNO_3 increases by 6.11% compared with the pure salt at 360 °C. An increase in the nanoparticle concentration to 2% does not change the specific heat capacity considerably considering the error bars. With 4% nanoparticles, the specific heat capacity is seen to decrease to 1.34 J K^{-1} g^{-1}, suggesting a decreasing found with increasing particle concentration at 360 °C.

The temperature effect on the specific heat capacity is shown in Figure 4.15 B for a temperature range from 345 to 360 °C. One can see approximately parallel curves for all samples, indicating a similar temperature dependence and little effect on the dependence from the addition of particles.

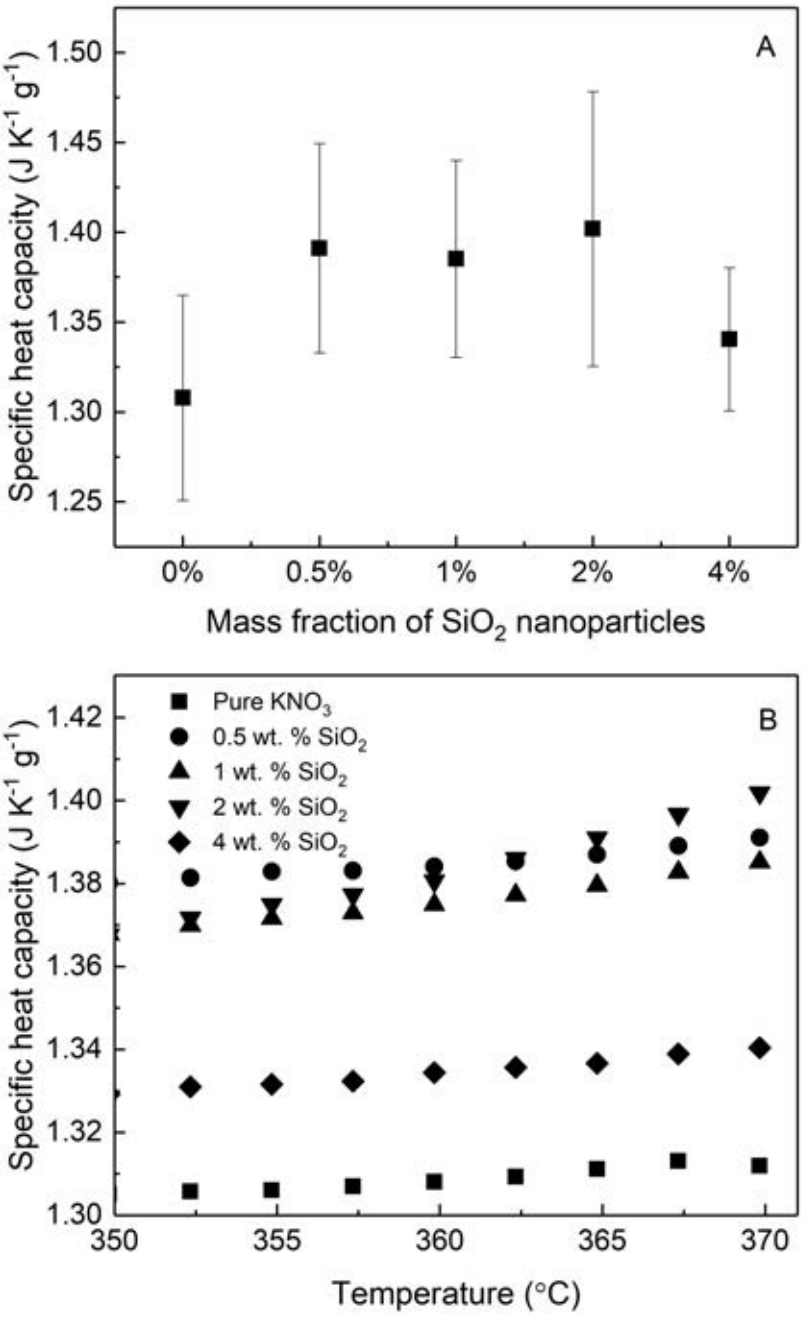

Figure 4.15: Specific heat of KNO_3 based suspensions with 20-30nm SiO_2 nanoparticles

A: Specific heat capacity of suspensions at 360 °C; B: Specific heat capacity against temperature of nanosuspensions with different fraction of nanoparticles

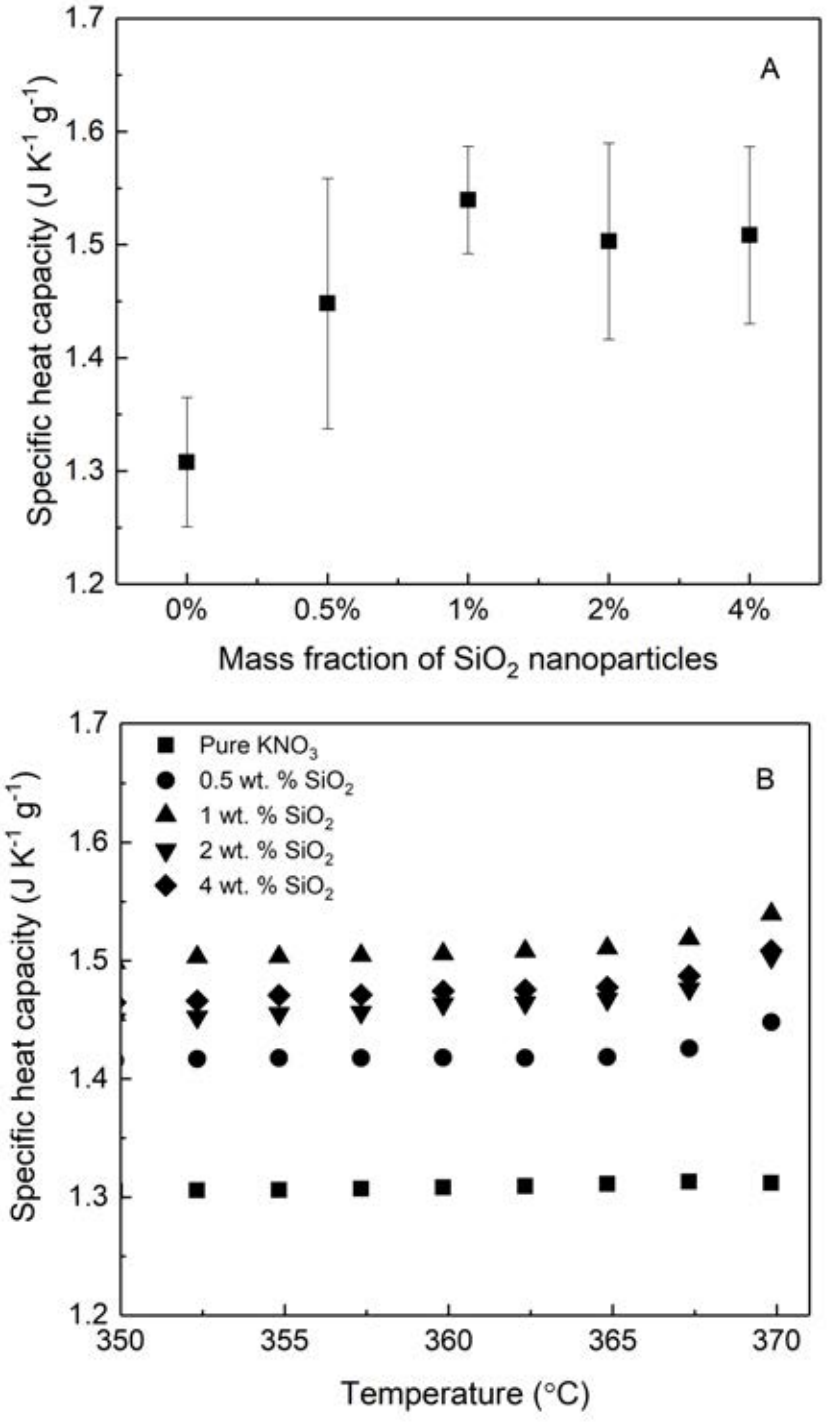

Figure 4.16: Specific heat of KNO_3 based nanosuspensions with 60-70nm SiO_2 nanoparticles

A: Specific heat capacity of nanosuspensions at 360 °C; B: Specific heat capacity against temperature of nanosuspensions with different fraction of nanoparticles

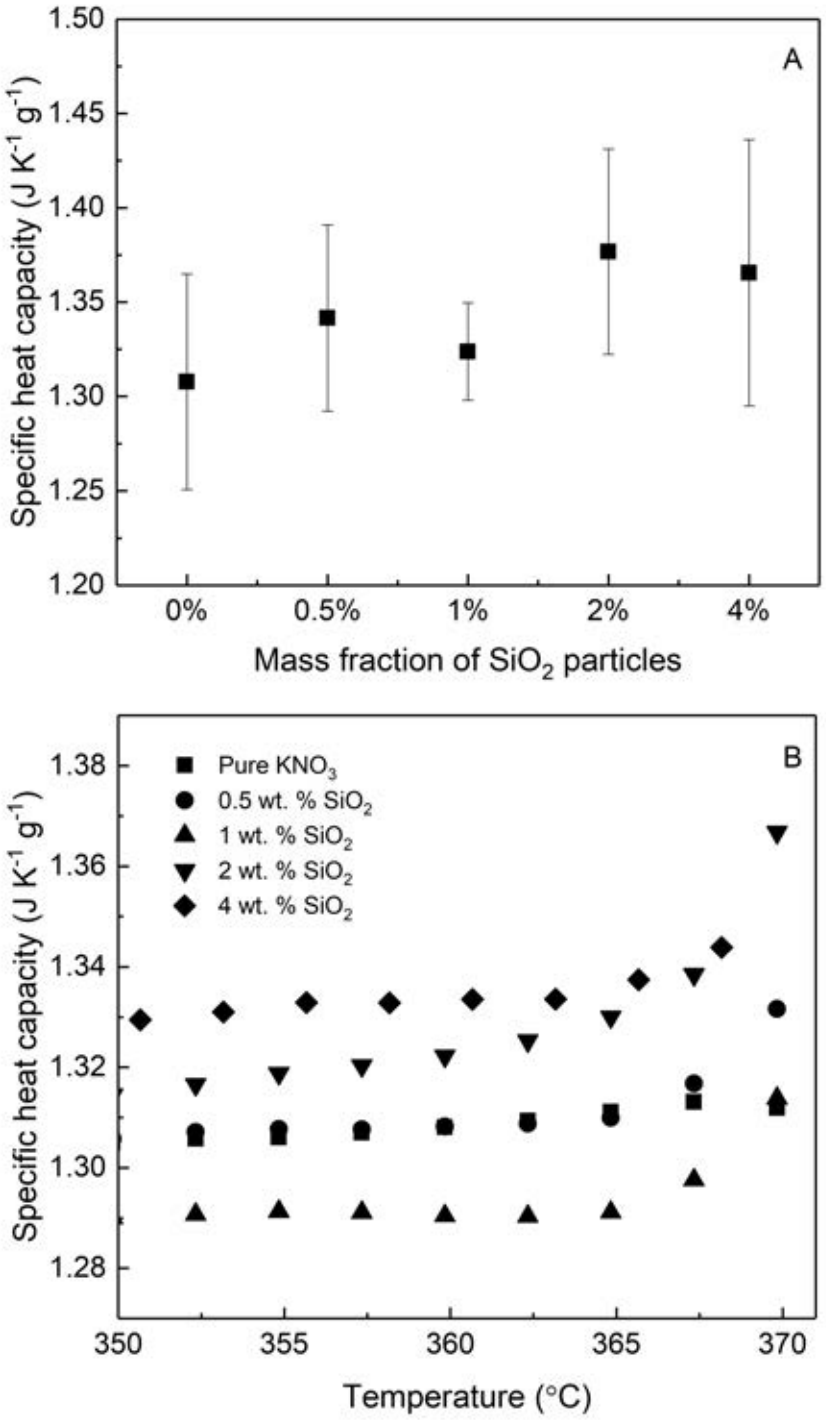

Figure 4.17: Specific heat of KNO_3 based mixtures A with 1-5μm SiO_2 particles

A: Specific heat capacity of mixtures at 360 °C; B: Specific heat capacity against temperature of mixtures with different fraction of particles

The specific heat capacity data for 60-70nm nanofluids are shown in Figure 4.16. At 360 °C, the introduction of nanoparticles give an increase in the specific heat of all tested samples. The specific heat capacity of KNO_3 pure salt was measured to be 1.31 J K^{-1} g^{-1} at 360 °C; an addition of 0.5% 60-70nm SiO_2 nanoparticles gives a specific heat capacity of about 1.45 J K^{-1} g^{-1}; with 1% SiO_2, the specific heat capacity increases to 1.54 J K^{-1} g^{-1}; a further increase in the particle concentration leads to a decrease in the specific heat capacity. Figure 4.16 B illustrates the temperature effect on the specific heat capacity of the KNO_3 based nanofluids for a temperature range from 350 to 360 °C. Little temperature effect is seen for all the samples as evidenced by the parallel curves with a very small slope with respect to the horizontal axis.

The data for the KNO_3 salt containing 1-5μm SiO_2 particles are shown in Figure 4.17. Little enhancement in the specific heat capacity is apparent at 360 °C considering the error bars. The temperature dependence of the KNO_3 salt containing 1-5μm SiO_2 is shown in 4.17 B. One can see a slight increasing trend of the specific heat capacity with temperature. However, little enhancement in the specific heat capacity is apparent given the error bars.

4.3 Phase Change Temperature and Latent Heat of Salt based Suspensions

4.3.1 Phase Change Temperature

The melting point of $NaNO_3$ based suspensions are shown in Figure 4.18. The melting point of the pure salt was observed to be 305.4 °C, which agrees with Takahashi, Sakamoto, and Kamimoto [55]. The addition of particles appears to give a decrease in the melting point. This is particularly so for the 15-20 nm and 20-30 nm nanoparticles, which leads to up to ~2.5 °C degrees in the melting point with 4% particle loading.

The lattice of the salt is held together by various intermolecular forces. These forces

are disrupted when a substance melts, which requires an input of energy. By introducing nanoparticles which disrupt the pattern of forces that holds the salt together, which eventually decrease the melting point.

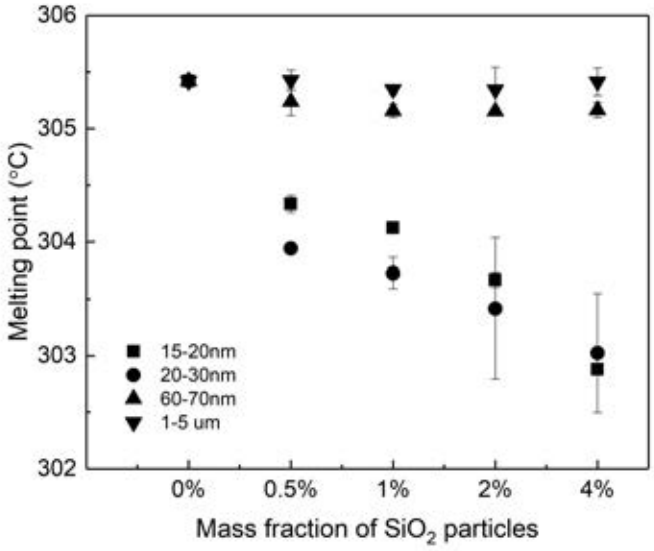

Figure 4.18: Melting point of $NaNO_3$ based nanosuspensions

As known, the melting point of a solution falls along with the weight fraction of the solute[219, 220]. The quantitative dependency is related to the variation of the system free energy after adding the solute. The nanoparticles are small in size, which is analogous to the solute in the molten salt[221]. The nanoparticles have considerable specific surface area and superfluours free energy. The free energy is reduced by absorbing molecules or ions in the adjacent area of a nanoparticle[222] so the melting point of nanosuspensions with 15-20nm and 20-30nm nanoparticles are following a decreasing tendency. As is shown in the diagram, particles with larger diameters do not cause a significant impact on the melting point due to the particle size.

The measured melting point data for $LiNO_3$ suspensions are shown in Figure 4.19. The addtion of all sizes of SiO_2 particles gives a change of the melting point within $\sim 1\,^{\circ}C$ and particle concentration does not seem to have much effect.

The impact of the introduction of SiO_2 particles on the melting point of KNO_3 is

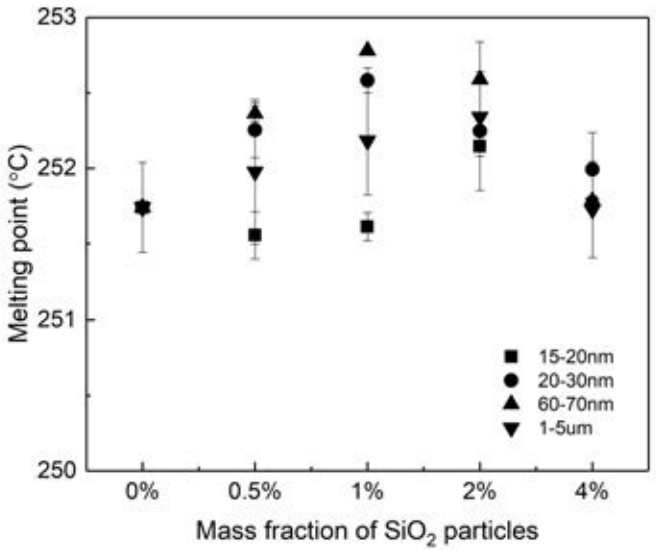

Figure 4.19: Melting point of $LiNO_3$ based nanosuspensions

shown in Figure 4.20. Overall, the addition of particles to the salt decreases the melting point, and the extent of decrease appears to increase with particle concentration. This is similar to the results shown in Figure 4.18 for $NaNO_3$ salt. However, the decrease in the melting point is small, within $\sim$1 °C, and hence is insignificant.

As is discussed, adding nanoparticles decreases the melting point of molten salt by reducing the free energy. In all KNO_3 nanosuspensions the melting point decreases as the fraction increases. This is in agreement with the theory that particles disrupt the crystal pattern and lower the melting point.

4.3.2 Latent Heat of Nanosuspensions

The latent heat of $NaNO_3$ based suspensions is shown in Figure 4.21. One can see that the pure salt has a melting enthalpy of $\sim$178 J g^{-1}, which is consistent with the literature data[55]. By adding 15-20nm and 20-30nm nanoparticles, the latent heat shows a decreasing trend with the rise increasing mass concentration of SiO_2 nanoparticles, and all suspensions exhibit a lower latent heat than the pure salt. With 4% SiO_2 nanoparticles, the latent heat for the 15-20nm and 20-30nm suspensions is 167.2J g^{-1} and 162.1J g^{-1},

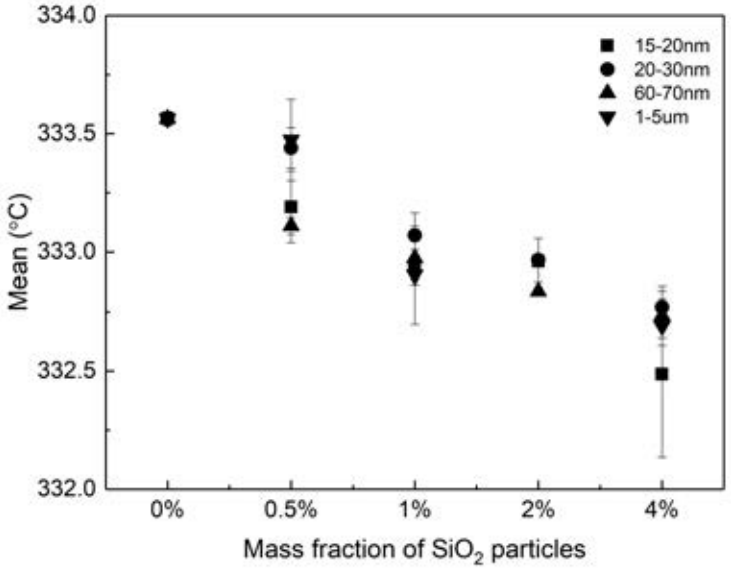

Figure 4.20: Melting point of KNO_3 based nanosuspensions

respectively. Little changes are seen on the latent heat due to the introduction of 0.5%, 1% and 2% SiO_2 60-70 nm nanoparticles. However, the latent heat decreases to 166.7J g^{-1} by introducing 4% 60-70nm nanoparticles. The addition of 1-5μm SiO_2 particles does not show any significant impact on the latent heat of the suspension.

The latent heat of $LiNO_3$ based suspensions is shown in Figure 4.22. The pure $LiNO_3$ salt has a latent heat of ~371 J g^{-1}, which agrees with the literature[55]. An addition of 15-20 nm nanoparticles decreases the latent heat, and the extent of the decrease depends on concentration. With 0.5% 15-20nm nanoparticles, the latent heat decreases to 368.8J g^{-1}, whereas the latent heat decreases to 351.6 J g^{-1} with 4% of the nanoparticles. For the 20-30nm suspensions, the addition of 0.5% and 1% nanoparticles increases the latent heat slightly, whereas further increase the nanoparticles to 2% and 4% shows a decrease in the latent heat, compared with the pure salt. Similar observations are seen for the 60-70nm suspensions that the data for the 0.5% and 1% samples have a higher latent heat than the pure salt whereas lower latent heat values are observed for the 2% and 4% suspensions. The addition of 0.5%, 1%, and 2% 1-5μm SiO_2 to the salt gives a small increase in the latent heat, whereas the 4% SiO_2 suspension has a slightly lower latent heat than the pure

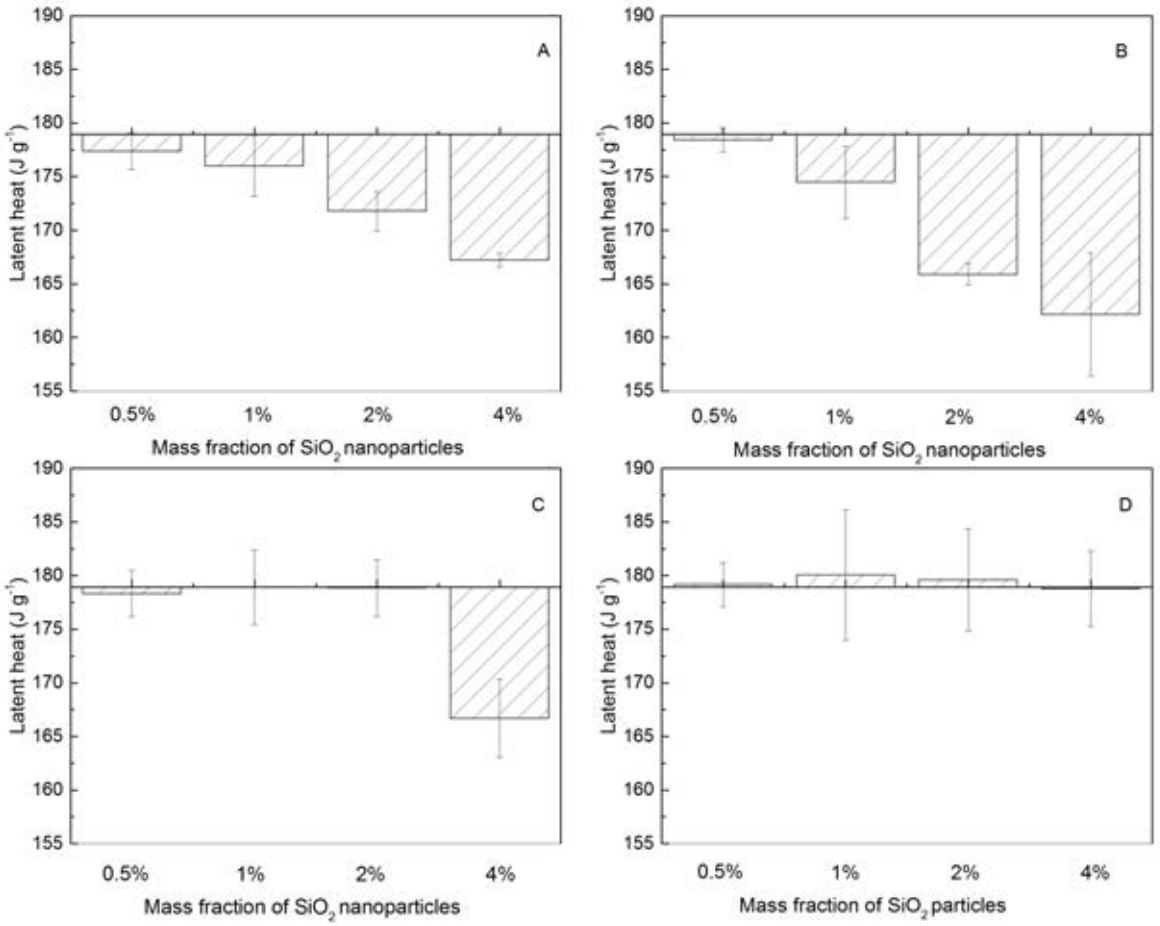

Figure 4.21: Latent heat of $NaNO_3$ based suspensions

A: With 15-20nm nanoparticles; B: With 20-30nm nanoparticles; C: With 60-70nm nanoparticles; D: With 1-5 μm particles

salt.

The latent heat of KNO_3 based suspensions is shown in Figure 4.23. One can see the pure salt has a melting enthalpy of $\sim$99 J g^{-1}, in agreement with the literature data[55].

The addition of particles leads to changes to the latent heat and the extent of the changes depends on particle size and concentration. Nano-sized particles give a more significant effect than the micron sized particles. The particle concentration effect appears to be a bit random, but the effect of adding 4% particles is consistent, giving a lower latent heat than the pure salt.

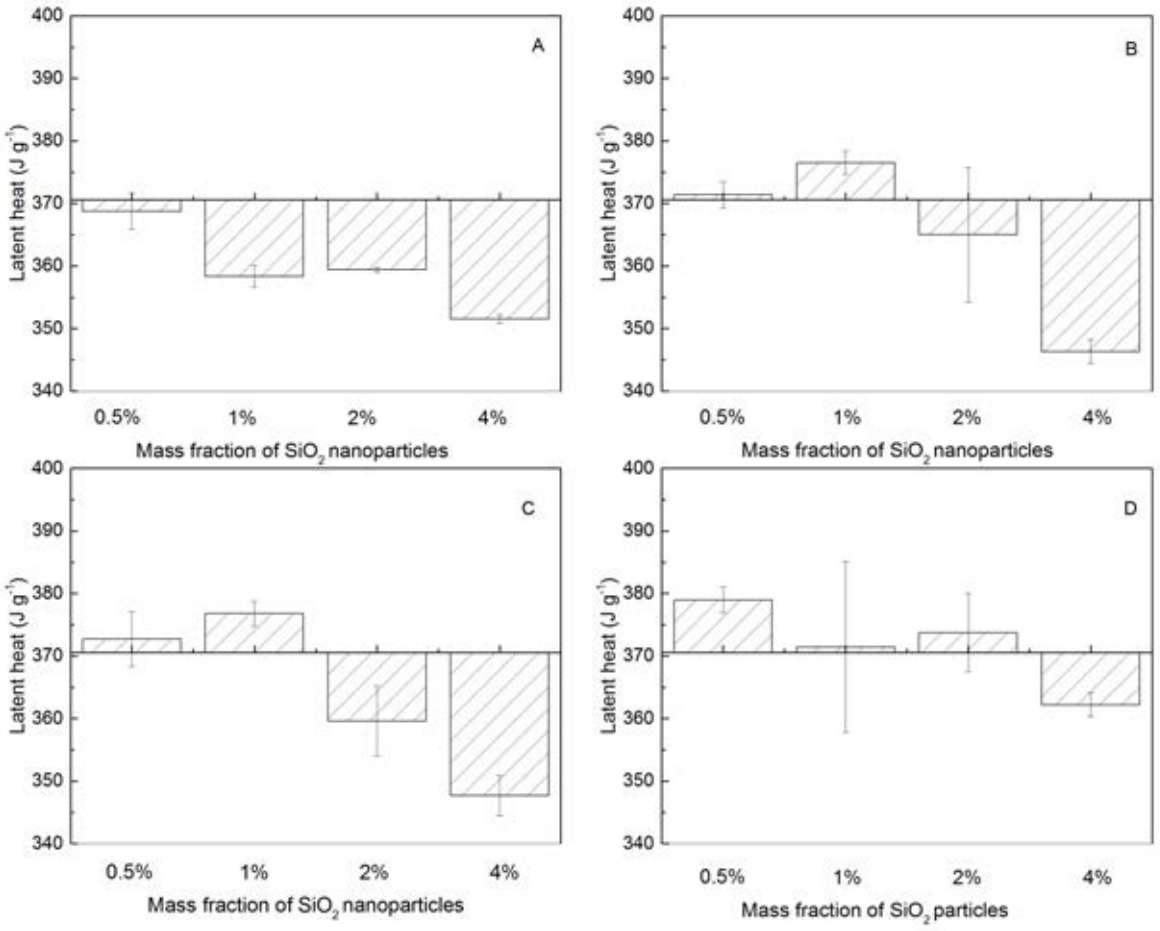

Figure 4.22: Latent heat of $LiNO_3$ based nanosuspensions

A: With 15-20nm nanoparticles; B: With 20-30nm nanoparticles; C: With 60-70nm nanoparticles; D: With 1-5 μm particles

4.4 Thermal Conductivity of Salt Suspensions

4.4.1 MD Simulation Results

The thermal conductivities of the nitrate salt based suspensions were simulated using the RNEMD method. Figure 4.24 A shows a sample plot of the thermal conductivity and Figure 4.24 B illustrates that the linear temperature gradients have been yielded with the kinetic energy swap rate of 20 timesteps, which is favourable for computing the thermal conductivities. The calculated thermal conductivities are listed in Table 4.3, together with the measured data (to be presented in section4.4.2). One can see that a reasonably good agreement has been achieved for the pure salt.

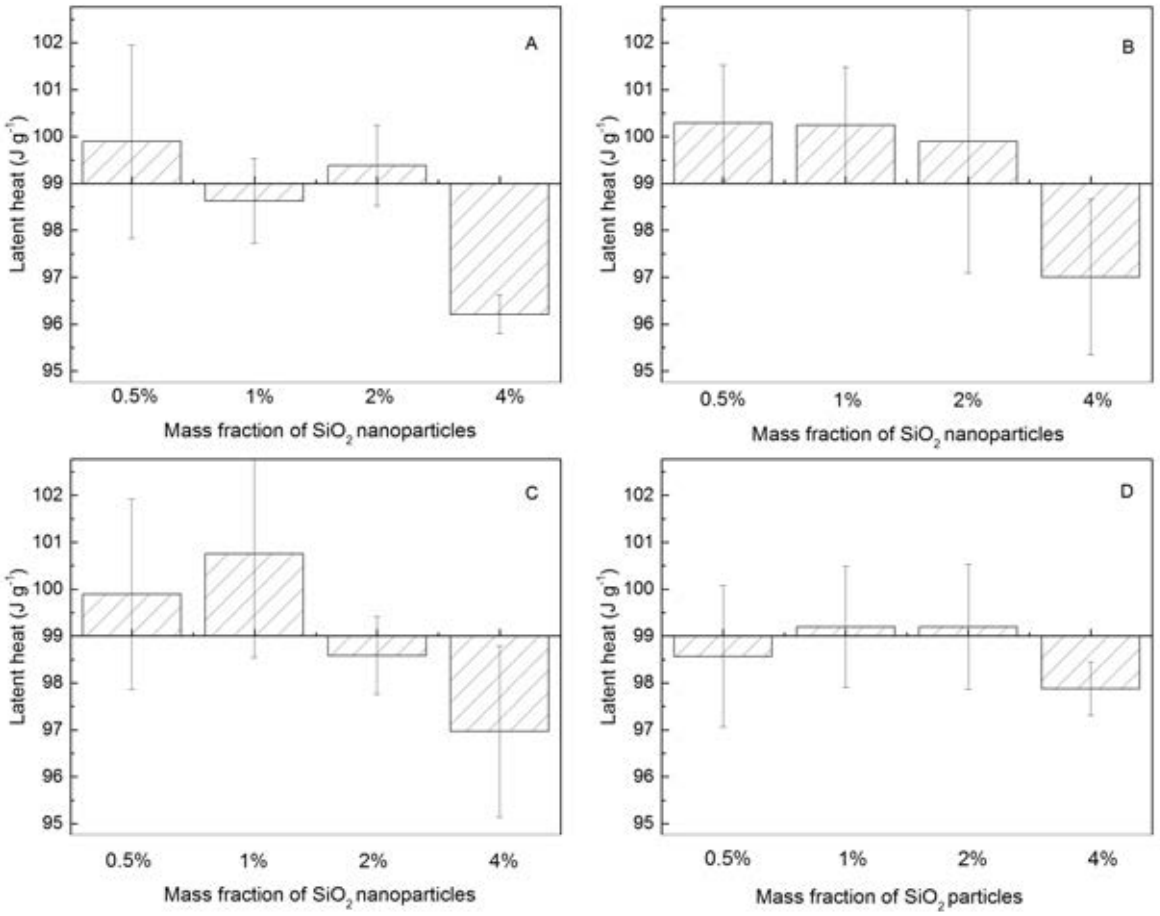

Figure 4.23: Latent heat of KNO_3 based nanosuspensions

A: With 15-20nm nanoparticles; B: With 20-30nm nanoparticles; C: With 60-70nm nanoparticles; D: With 1-5μm particles

The calculated thermal conductivities of nitrate salt based nanofluids at 700K are shown in Figure 4.25. The thermal conductivities of the pure $NaNO_3$ is 0.658W m^{-1} K^{-1}. The addition 1% of SiO_2 gives a decrease in the thermal conductivity by 0.003W m^{-1} K^{-1}, and further addition of the particles to 5.8% leads to further decrease by 0.022W m^{-1} K^{-1}. The addition of 14% nanoparticles shows however an increase in the thermal conductivity to 0.675W m^{-1} K^{-1}. This is equivalent to an enhancement of 2.5% compared with the pure salt. Similar observations were obained for the KNO_3 based suspensions. The thermal conductivity decreases with particles concentration first, reaches a trough, and then increases with a further increasing in the particle concentration. The thermal conductivity of the 5.6% nanofluids is 0.415W m^{-1} K^{-1}, which is 0.013W m^{-1} K^{-1} lower

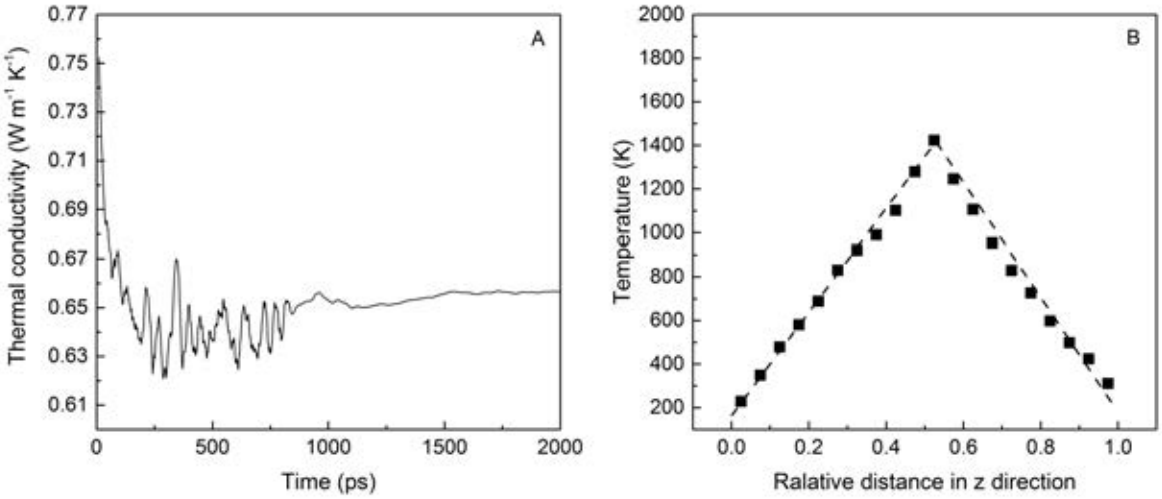

Figure 4.24: The sample plot of the thermal conductivity of $NaNO_3$

A: The convergency of the thermal conductivity as a function of time for $NaNO_3$; B: The converged temperature gradient at 20 time step swap rate

Table 4.3: Calculated thermal conductivity (W m^{-1} K^{-1}) of pure materials and comparison with experiments[223–226]

	Experimental	Simulation
$LiNO_3$ at 700K	0.61	0.622
$NaNO_3$ at 700K	0.49	0.658
KNO_3 at 700K	0.39	0.428
SiO_2 at 700K	1.34	1.346

than that of the pure KNO_3. By introducing 14% nanoparticles, the thermal conductivity increases to 0.434W m^{-1} K^{-1}, which is 0.005 higher than that of the pure KNO_3. Similar SiO_2 concentration dependence on the thermal conductivity holds for both KNO_3 and $LiNO_3$ salts as shown in Figure 4.25.

SiO_2 has a higher thermal conductivity than the salts, which should have enhanced the thermal conductivity. The simulation results show a clear contradiction, which will be discussed in section 4.5.

4.4.2 Experiment Results

The thermal conductivities of $NaNO_3$ based suspensions are shown in Figure 4.26. One can see that the thermal conductivity of the pure $NaNO_3$ is $\sim$ 0.54W m^{-1} K^{-1} over the

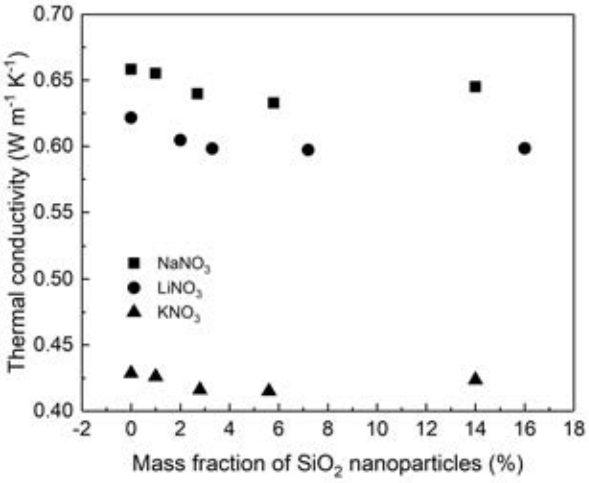

Figure 4.25: Calculated thermal conductivity of nitrate salt based nanofluids from MD simulations at 700K

temperature range from 320 °C to 370 °C. This is in good agreement with the literature[223]. With the introduction of 0.5% nanoparticles, the average thermal conductivity of the suspension decreases to 0.49W m^{-1} K^{-1}. A further increase in the nanoparticle concentration to 1% decreases the thermal conductivity further to 0.42W m^{-1} K^{-1}. At a particle concentration of 2%, the decreasing trend of thermal conductivity stops, and a further increase to 4% gives an increase to the thermal conductivity to 0.46W m^{-1} K^{-1}. Figure 4.26 also shows a small effect of temperature on the thermal conductivity over the temperature range between 320 and 370 °C.

The thermal conductivities of the $LiNO_3$ based suspensions are shown in Figure 4.27. One can see that the introduction of SiO_2 particles all decreases the thermal conductivity compared with the pure $LiNO_3$. The effects of particle concentration and temperature on the thermal conductivity are similar to the observation of $NaNO_3$ suspensions.

The thermal conductivity of KNO_3 based suspensions is shown in Figure 4.28. The pure KNO_3 has a measured thermal conductivity of ∼0.46W m^{-1} K^{-1}. The addition of SiO_2 gives a decrease in the thermal conductivity. Over the concentration and temperature ranges studied in this work. Figure 4.28 shows a similar temperature and particle concentration dependence to that of $NaNO_3$ and $LiNO_3$ suspensions.

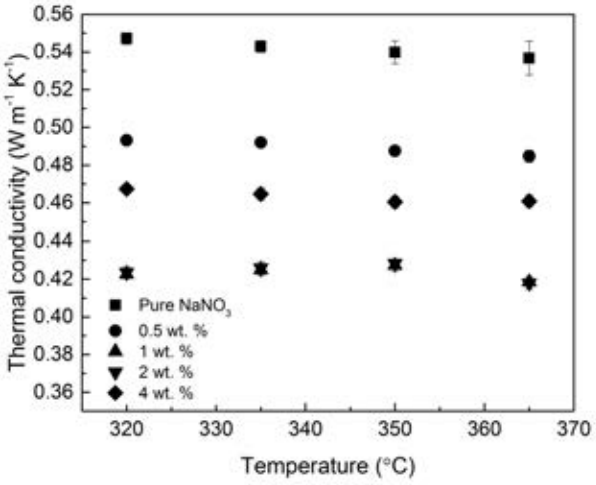

Figure 4.26: Thermal conductivity of $NaNO_3$ based suspensions with 15-20nm SiO_2 nanoparticles

4.5 Summary

Table 4.4: Highest specific heat capacities in the salt based nanofluids

Salt	Particle size	Highest specific heat capacity J K^{-1} g^{-1}	Particle fraction	Enhancement
$NaNO_3$	15-20nm	1.71	1%	5.0%
	20-30nm	1.73	0.5%	6.1%
	60-70nm	2.08	0.5%	27.6%
	1-5μm	1.67	1%	2.4%
$LiNO_3$	15-20nm	2.10	0.5%	8.2%
	20-30nm	2.14	0.5%	10.3%
	60-70nm	2.08	0.5%	7.2%
	1-5μm	1.98	0.5%	2.1%
KNO_3	15-20nm	1.31	2%	0.0%
	20-30nm	1.40	2%	6.8%
	60-70nm	1.54	1%	17.6%
	1-5μm	1.38	0.5%	5.3%

The introduction of SiO_2 nanoparticles enhanced the specific heat capacity of salt based nanosuspensions in both the experiment and simulation. The highest specific heat capacities in each set of sample are listed in Table 4.4. The main factors that affected the enhancement are as follows:

The specific heat capacity was enhanced by different extent in different salts. In both $NaNO_3$ and KNO_3 based nanosuspensions, the highest enhancement was observed in the 60-70nm nanosuspensions with the value of 27.6% and 17.6%, respectively. With the

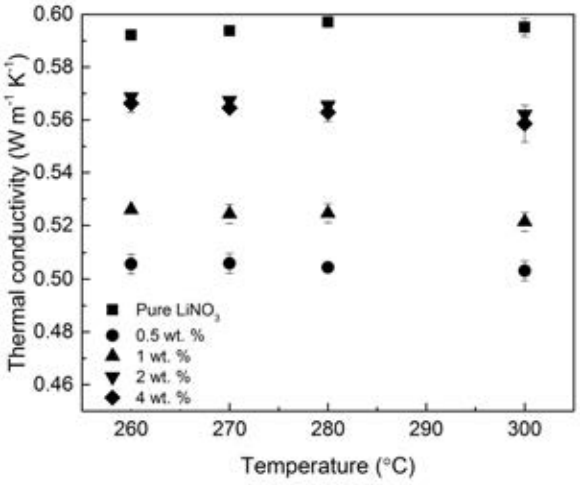

Figure 4.27: Thermal conductivity of $LiNO_3$ based suspensions with 15-20nm SiO_2 nanoparticles

introduction of other sizes of particles, the specific heat capacity enhancement was found to be less than 7% in these salts, hence it is concluded that the 60-70nm nanoparticles were capable of enhancing the specific heat capacity of $NaNO_3$ and KNO_3. With 0.5% 20-30nm nanoparticles introduced in molten $LiNO_3$, the specific heat capacity was enhanced by 10.3% which was the highest compared with other $LiNO_3$ based nanosuspensions. In the three nitrate salts, the impact of nanoparticles on the specific heat capacity was observed differently and $NaNO_3$ received the highest enhancement whereas the $LiNO_3$ had the least.

The highest enhancements all happened with the particle of 0.5% to 2% and no highest specific heat capacity was found in the 4% sample. It indicated that increasing the fraction of nanoparticles could only enhance the specific heat capacity to a certain extent. Further adding nanoparticles would hinder the enhancement of specific heat capacity. This was attributed to the aggregation which will be discussed in Section 5.1.

From 15nm to 5μm, different sizes of nanoparticles caused varying degrees of specific heat capacity enhancement. The specific heat capacity of $NaNO_3$ and KNO_3 based nanosuspensions was enhanced mostly by the 60-70nm nanoparticles whereas the 20-30nm $LiNO_3$ based nanosuspensions gained the highest enhancement. Limited enhancement was observed in the mixture of salt and 1-5μm particles and the highest enhancement which

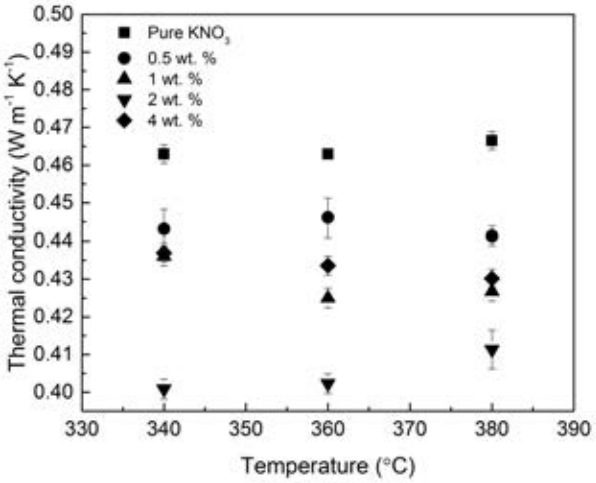

Figure 4.28: Thermal conductivity of KNO_3 based suspensions with 15-20nm SiO_2 nanoparticles

was by 5.3% was found in KNO_3 based mixture. Also the 15-20nm nanoparticles which are the smallest in the study exhibited the lower specific heat capacity enhancing capability than other sizes of nanoparticles. The aforementioned assumption that the smaller nanoparticles possess better capability of enhancing the specific heat capacity was not represented in the results. The aggregation might also caused this phenomenon that the smaller nanoparticles were reported having faster aggregation rates than larger ones[227].

This anomalous enhancement confirmed that the specific heat capacity of molten nitrate salt based nanosuspensions could not be simply calculated with the classical model (equation 2.5) hence alternative theoretical precepts need to be explored.

The melting points of the molten salts were slightly affected by the introduction of nanoparticles in that the greatest difference observed was 2 °C. It is found that in the 4% nanosuspensions the latent heat decreased significantly compared with the pure salt whereas nanosuspensions with other fractions of nanoparticles was not distinctly affected. In the mixture with 1-5μm nanoparticles, the impact of particles on the latent heat was much lower than that on nanosuspensions. Particularly the influence on the mixture based on $NaNO_3$ was insignificant.

SiO_2 is commonly added in nanofluids as the conductivity enhancer attributing to its high conductivity. Based on the computed results that SiO_2 was more conductive than

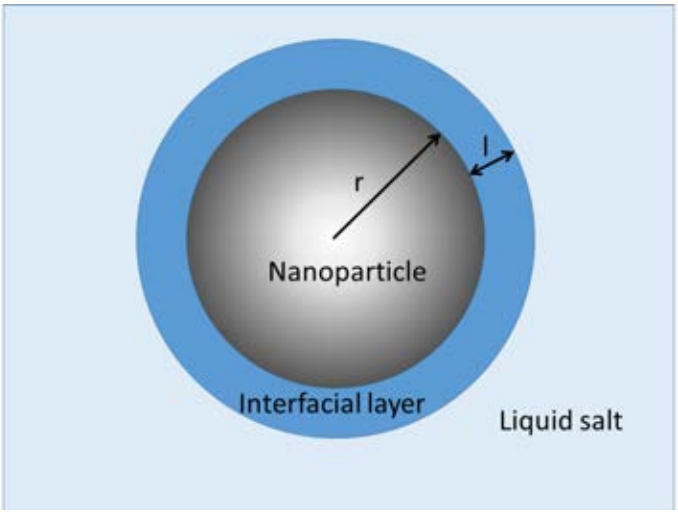

Figure 4.29: A nanoparticle with interfacial layer in a molten salt fluid

that of all nitrate based nanosuspensions, all salt based nanosuspension were expected to exhibit an enhanced thermal conductivity. However in both simulations and experiments, the results were against our expectations. A model shown in Figure 4.29 is proposed to explain this phenomenon. Though the thermal conductivity of the SiO_2 was higher than that of the molten salt, an interfacial layer existed between the solid nanoparticle and the liquid molten salt provides a much higher thermal resistance which significantly hindered the heat transfer between the nanoparticle and salt. The thermal conductivity was then determined by the thermal conductivity and size of nanoparticles, thermal conductivity of molten salt and the thickness and the thermal conductivity of the interfacial layer.

CHAPTER 5

RESULTS AND DISCUSSION: MECHANISMS OF THE ENHANCEMENT OF SPECIFIC HEAT CAPACITY OF SALTS DUE TO THE ADDITION OF NANOPARTICLES

This chapter discusses the mechanisms of the specific heat capacity enhancement based on experimental and simulation observations.

Section 5.1 analyses the composition and surface character of molten salt with nanoparticles. Section 5.2,5.3 discuss the salt atom arrangement at the adjacent area of a nanoparticle using MD simulations. Section 5.4 studies the intermolecular forces between nanoparticle and salt with MD simulations, and further discuss the mechanism of the enhancement of specific heat capacity.

5.1 Structural, Morphological and Compositional Analysis

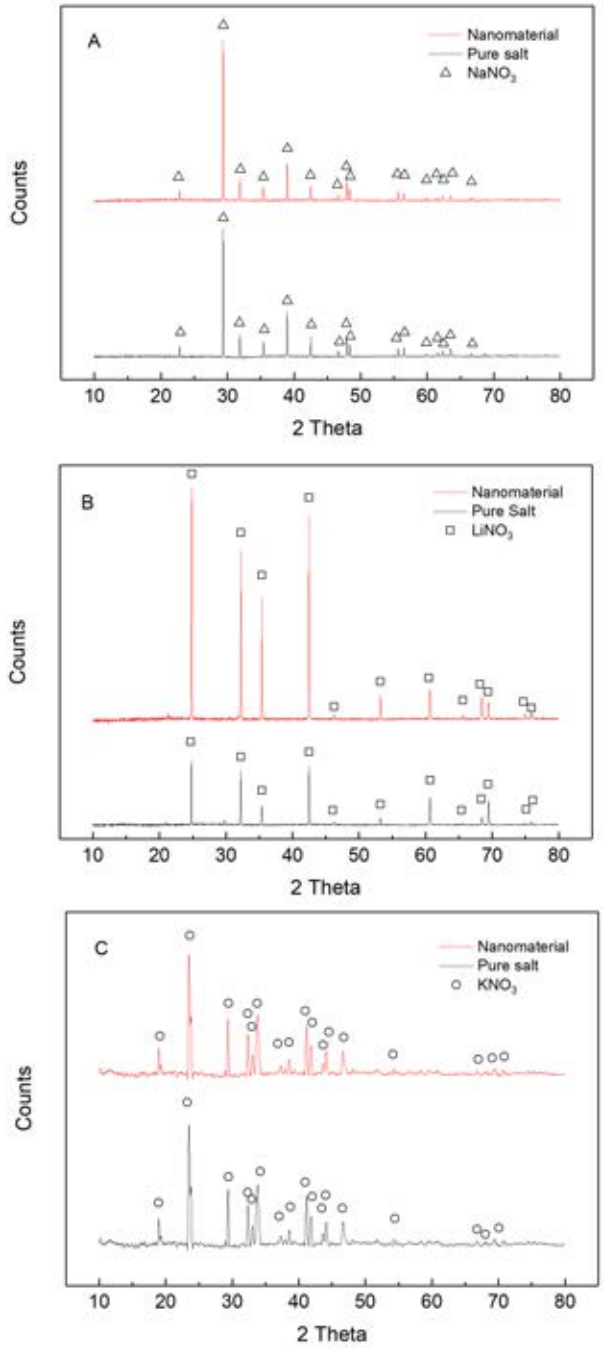

Figure 5.1: XRD analysis of salts and nanosuspensions with 0.5% 15-20nm SiO_2 nanoparticles

A: $NaNO_3$ and its salt-nanoparticle mixture; B: $LiNO_3$ and its salt-nanoparticle mixture; C: KNO_3 and its salt-nanoparticle mixture based

The structural analysis were performed on the pure salts and their nanoparticle mixtures using a X-Ray Diffractometer. Before the analysis, the salts and salt-silica nanoparticles mixtures were cycled 50 times (200 - 350 °C for $NaNO_3$, 200 - 310°C for $LiNO_3$ and 270 - 380°C for KNO_3) at a heating/cooling rate of 10 °C/min. Figure 5.1 shows the XRD pattern of the salts and their mixtures with 0.5% 15-20nm SiO_2. One can see that the addition of the nanoparticles did not change crystallinity of the nitrate salts and there were no new phase created. The SiO_2 particles used are amorphous, and hence are reflected in the XRD graphs. Silica is also detected by EDS in the salt-SiO_2 mixture as no silica is found in the pure KNO_3.

The morphological analysis were done by using a Scanning Electron Microscope (SEM) with EDS. Figure 5.2 shows that nanoparticles are found in the sample. Figure 5.3 shows SEM images and associated EDS spectra of pure KNO_3 salt (A) and SiO_2-KNO_3 mixture (B) with 0.5% SiO_2 15-20nm. One can see silica nanoparticles are concentrated in between the salt crystals.

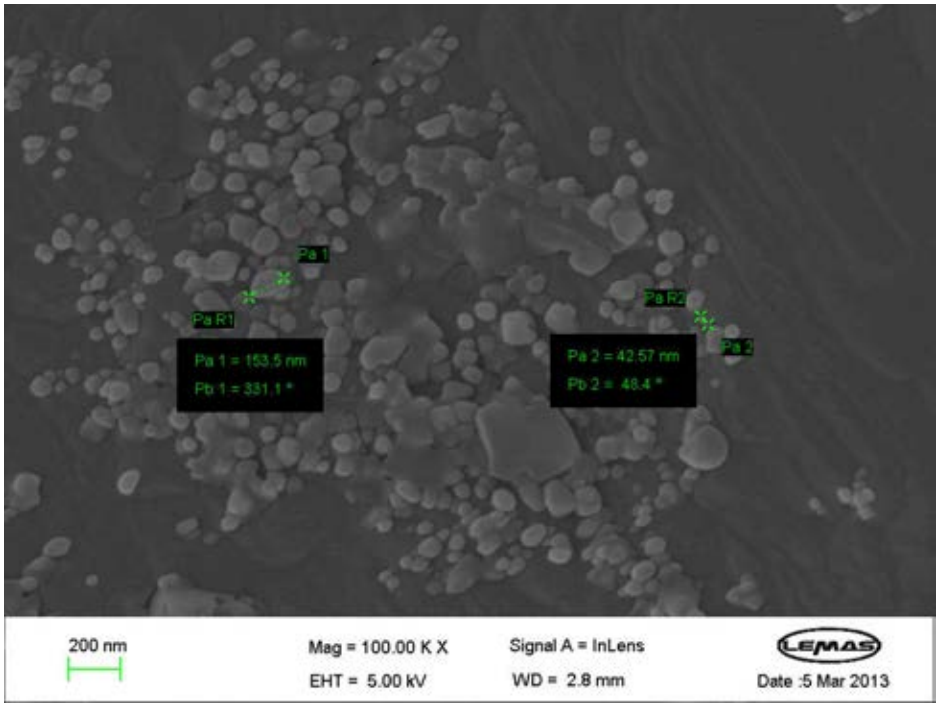

Figure 5.2: Nanoparticles in KNO_3 salt observed using SEM

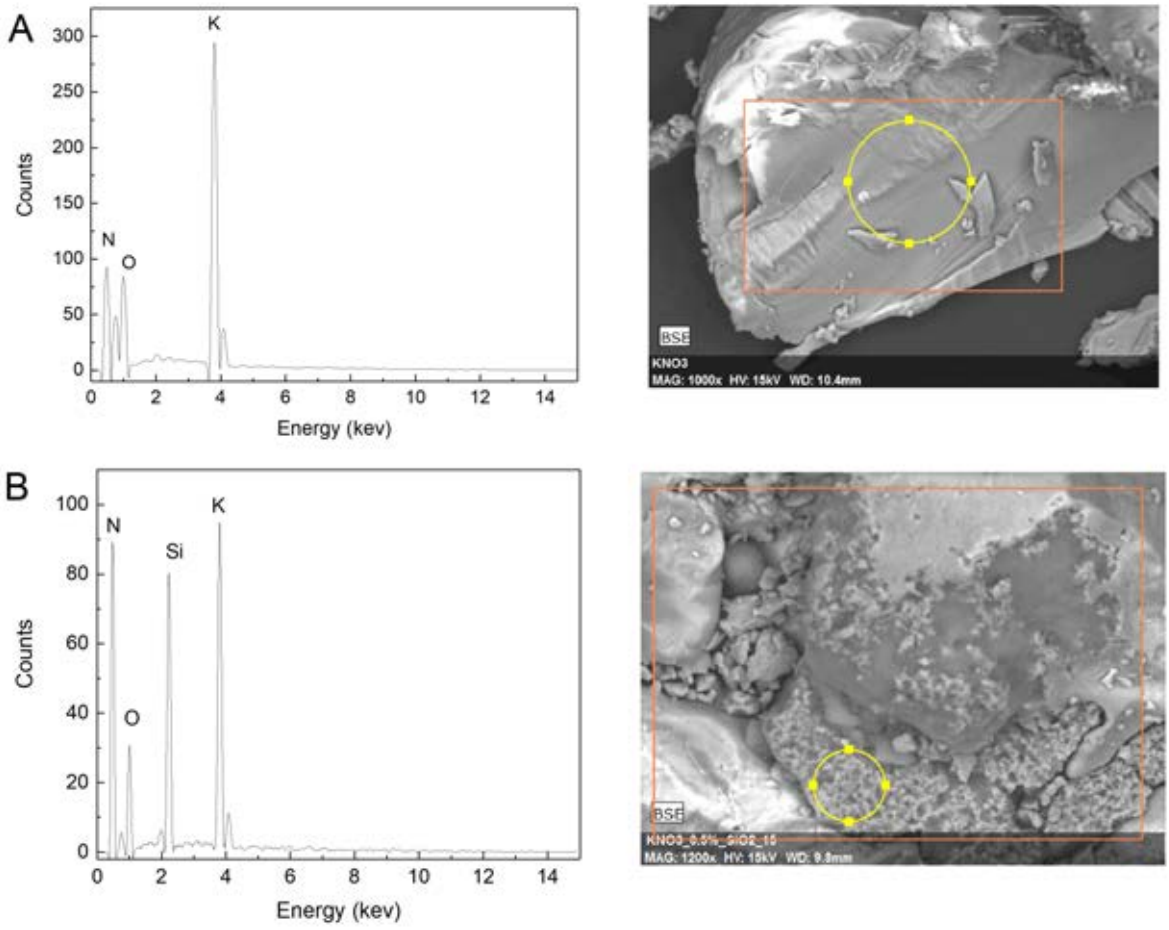

Figure 5.3: SEM images and EDS spectra

A: Pure KNO_3 salt B: KNO_3-SiO_2 mixture with 0.5% 15-20 SiO_2 nanoparticles

SiO_2 in KNO_3 is exhibited in Figure 5.3 enlargement of the nanoparticle rich region in the SEM image gives Figure 5.4A and 5.4B (at different magnifications). One can see clearly that aggregation of SiO_2 nanoparticles has occurred (Figure 5.4B), and the SiO_2 nanoparticles form a stripe-like pattern (Figure 5.4A). These aggregations and stripe-like pattern occur in between the salt crystals after solidification and those nanoparticles are not seen in a close contact with the salt crystals. Agglomeration of nanoparticles has also been observed in [3, 7, 152], which has also been considered to be related to the enhanced specific heat capacity [7, 152, 154].

SiO_2 particles do not seem to have a very high surface energy on the KNO_3 salt as particles are segregated from large salt crystals after solidification forming porous silica

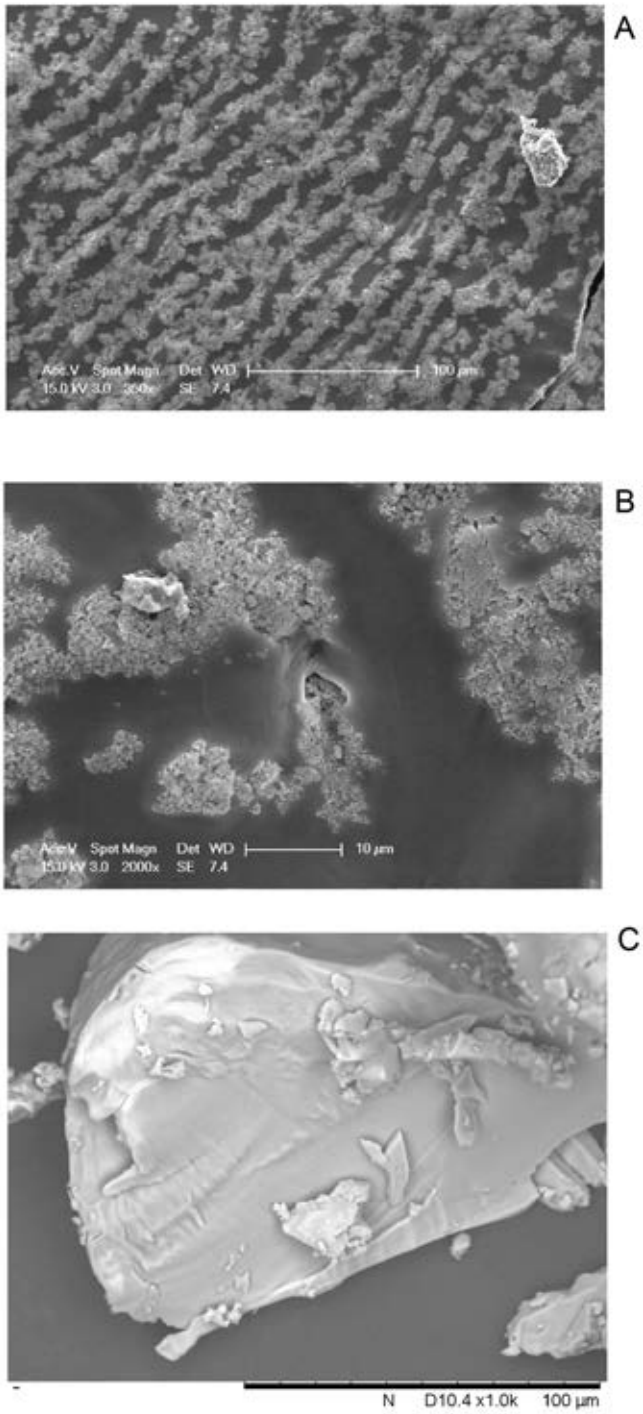

Figure 5.4: SEM image of KNO_3 based nanomixtures with 4% 15-20nm SiO_2 nanoparticles

particle rich regions between salt crystals, and the particles in the silica rich region organise themselves into the strip pattern. The strip-like ordered structure has also been observed

by Dudda and Shin [154]. The segregation is also supported by little silica presence in the salt crystal surface as shown in Figure 5.3A. However, the presence of salt in the particle rich region is apparent from Figure 5.3 where Si is detected. Interestingly, there are regions as shown in Figure 5.5A where aggregation of small salt particles exist with no SiO_2 presence (Figure 5.5B).

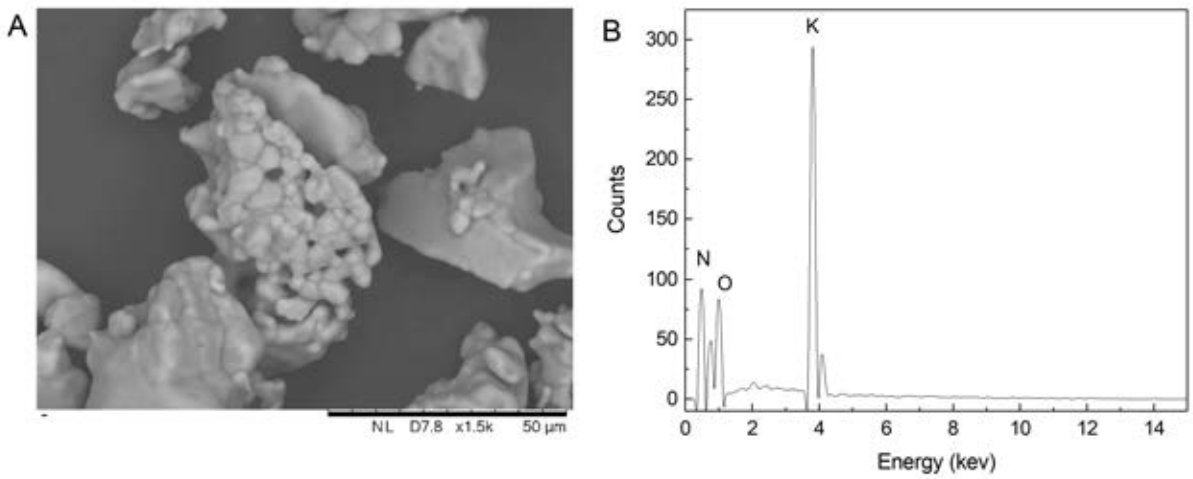

Figure 5.5: SEM image and EDS spectra from a region of KNO_3 based mixture with 0.5% 15-20nm SiO_2 A: SEM image B: EDS spectra

5.2 Nitrate Salt Atom Arrangement at the Adjacent to A Nanoparticle

The experimental observations of the enhanced specific heat capacity appear to pinpoint the enhancement to the interactions between salt and nanoparticles at the interfacial area at the atomic scale. As a result, it is hypothesized that the mechanism of the enhancement is due to the interactions at the atomic scale. MD simulations are therefore used to study the arrangement of salt atoms around a nanoparticle.

Figure 5.6 shows the RDF of Na-N in $NaNO_3$ salt without nanoparticles. The distance between a pair of nitrogen and sodium atom is greater than 2.43Å because g(r) is zero

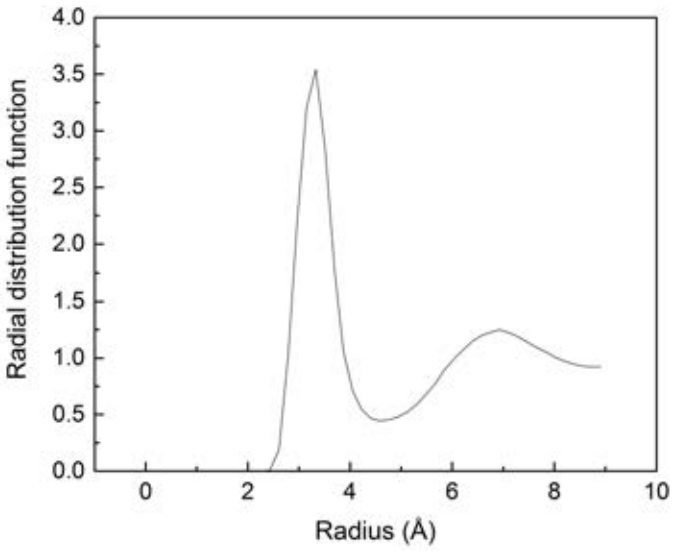

Figure 5.6: Radial distribution function of Na-N in a $NaNO_3$ salt system

while $r < 2.43$Å. The first shell occurs at a distance of 3.33Å where nitrogen atoms are most likely to appear around a sodium atom. This information will be used later to explain the so-called "compression" effect due to the presence of nanoparticles. Figure 5.7 shows the normalised number density of atoms in the $NaNO_3$ salt with and without nanoparticles. Without nano particles, salt atoms distribute evenly as shown in Figure 5.7A. In the presence of a nanoparticle, separation between the anions and cations close to the surface of the nanoparticle is apparent as shown in 5.7B. The first Na atom locates at a radius of 5.1Å and a peak value of 1.39 is found at 7.65Å. The number of Na starts to decrease, reaching the lowest value of 0.899 at a radius of 9.35Å before recovering to 1 at 12Å. The number of nitrogen atoms keeps increasing reaching a peak of 1.37 at 9.35Å corresponding the lowest number of Na atoms. The data for O atoms are similar to that of N, except for the peak value is slightly lower, at 1.22.

Between 7.65Å and 9.35Å, the cations and anions formed an approximately 2Å layer with the ordering of the ions different from the pure molten salt as shown in 5.7. Atoms in this layer form a structure which is more ordered and denser than that in liquid $NaNO_3$. Na ions are mainly concentrated at the inner side and nitrate ions are at the outer side of

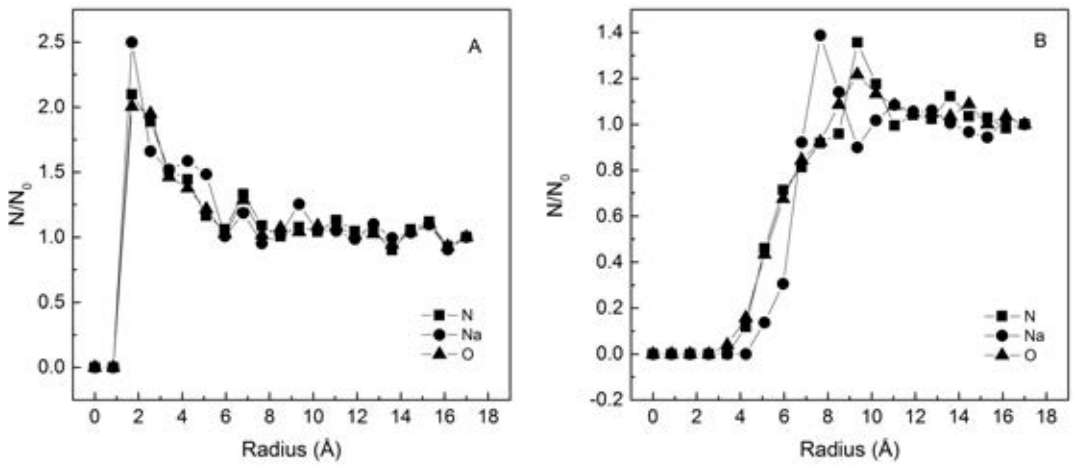

Figure 5.7: Normalized number density of atoms in sodium nitrate salt

A. Distribution of atoms in molten $NaNO_3$ salt. Horizontal axis denotes the distance from a random point in the system; N/N_0 is the relative number density of an atom over the number density of that atom far away from that point; B. Distribution of atoms in $NaNO_3$-SiO_2 system. Horizontal axis is the distance from the geometric centre of the nanoparticle; n/n_0 is the relative number density of an atom over the number density of that atom far away from the centre

the layer. The existence of the ordered layer has also been observed by Li et al. [156] and supported by transmission electron microscopy (TEM) images. Oh et al. [157] reported that crystals can induce ordering in liquids.

5.3 Energy Analysis of the Nanoparticle-salt Mixtures

To understand the reason of the enhancement of specific heat capacity, the different components of the potential energy as shown in Figure 5.8 are analysed. The specific heat capacity measures the amount of energy stored in a certain amount of substance at a given temperature and it is the summation of the energy of the atoms in a system. The energy per atom consists of kinetic and potential parts and can be expressed as:

$$E = E_{kin} + E_{cdw} + E_{coul} + E_{bond} + E_{angle} + E_{improper} \tag{5.1}$$

where E_{kin} is kinetic energy; the potential energy includes several terms of, E_{vdW}, the van der Waals potential energy; E_{coul}, the coulombic potential consisting of short range

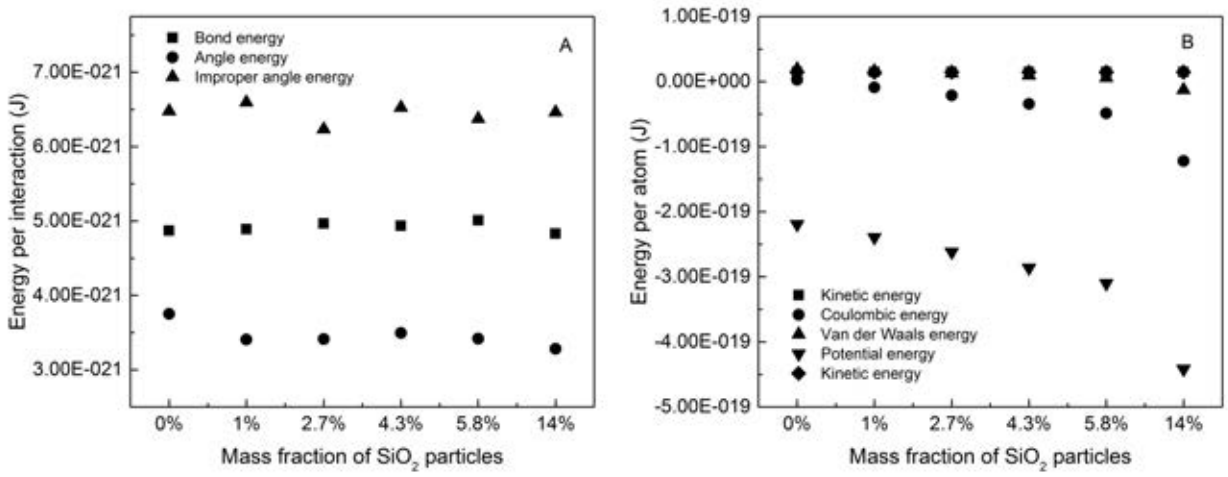

Figure 5.8: Potential energy analysis in nanoparticle-salt Mixtures at 700K

A: Energy of three different intramolecular interactions in NO_3 anion: bonds between nitrogen and oxygen, angles between O-N-O, and improper dihedral angles in NO_3; B: Energy of intermolecular interactions in a system

and long range ones; E_{bond}, E_{angle} and $E_{improper}$, intramolecular bond, angle, and improper angle potentials, respectively. The terms are calculated based on force fields described in section 3.2.2.

Figure 5.8 shows the results that kinetic energy does not change with the change of the concentration of nanoparticles at a given temperature. There is a significant decline in the potential energy per atom as the mass fraction of nanoparticles increases, implying that the introduction of nanoparticles leads to the attractive force in the system being greatly strengthened.

Figure 5.8 also clearly shows that the main changes due to the introduction of nanoparticles occur in the coulombic energy which decreases drastically. At the mass fraction of SiO_2 nanoparticles of 14%, the coulombic energy per atom turns into attractive and is 46 times stronger than that in pure $NaNO_3$ system while is repulsive. No significant impact is seen on other kinds of energy due to the addition of nanoparticles. While the potential energy of the whole system decreases with the addition of nanoparticles, the potential energy between salt atoms was increasing proportionately with the concentration of nanoparticles (Figure 5.9). This could be attributed to the fact that the average

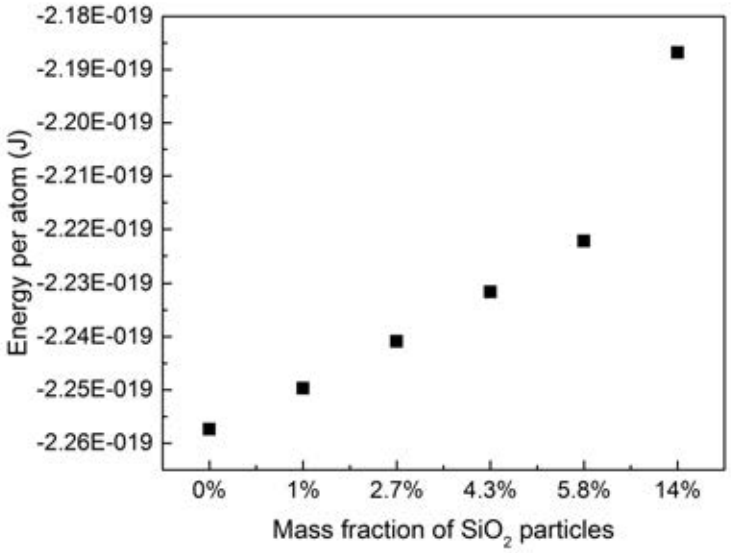

Figure 5.9: Potential energy per atom between salt atoms at 700K

distance between salt atoms is affected by the introduction of nanoparticles as indicated in Figure 5.6 and Figure 5.7B.

The introduction of SiO_2 nanoparticles gives rise to a significant decrease in the coulombic energy, and, as a result, creates a strong attractive force around the adjacent area of the nanoparticles. The attractive force greatly affects the distribution of nitrate salt ions by attracting them to the nanoparticles, and forming an ordered layer. Such an ordered layer of cations and anions is solid-like with the distance between the ions diminishing because of the electrostatic forces, making the layer look "compressed". In this "compressed" layer, the cations and anions are separated because of the van der Waals (vdW) potential. This agrees with the number density analysis (Section 5.2) where a compressed layer is shown adjacent to the nanoparticle with the salt atoms having a shorter average distance than that in pure salt. Because the average distance of salt atoms diminishes, the van der Waals force generates a stronger repulsive force, leading to the enhancement of the potential energy between salt atoms as shown in Figure 5.9.

The kinetic energy increases proportionately with increasing temperature as expected. The simulation results also show another phenomenon in the presence of nanoparticles

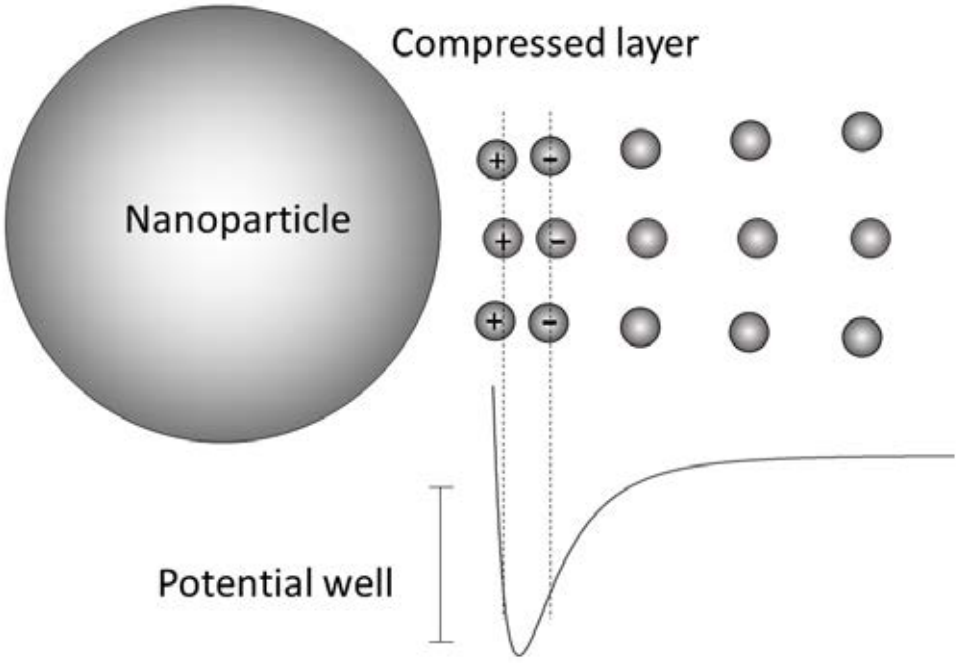

Figure 5.10: The compressed layer created by the nanoparticle

due to the introduction of a strong attractive force, leading to a deep potential well. As a result, the movement of salt atoms is greatly confined at the adjacent area of the nanoparticle surface, see Figure 5.10. The atoms in the layer are more stable with the cations and anions separated and more energy input is needed to deform this structure. Due to the attractive force of a nanoparticle, the kinetic energy of these atoms can only increase in a limited extent until the atoms overcome the energy barrier. This is similar to the case of a solid-liquid phase change process, but only happens in the layer around the nanoparticle in the nanoparticle-salt. One can conclude that it is the coulombic force introduced by nanoparticles that causes the formation of the compressed ion layer, leading to the enhancement of specific heat capacity.

The layer and the separation of cations and anions can only exist in ionic liquids whereas in non-ionic liquids the molecules are affected by coulombic force equally and thus the layer and the separation will not be formed. This may be the reason that the specific heat capacity enhancement have only been observed in ionic liquid based nanosuspensions.

5.4 MD Simulations using modified force fields for KCl based Nanoparticle-salt mixtures

As is discussed in Section 5.3, salt atoms at the adjacent area of the surface of a nanoparticle are trapped in a compressed layer due to the intermolecular interactions and the cations and anions are separated in this layer. In order to further verify this and to investigate the relationship between the force fields and the enhancement of specific heat capacity, KCl based nanoparticle-salt mixtures are simulated. The main reason for choosing KCl is that there are two ions in a molecule, K^+ and Cl^-, and the molar mass of K and Cl are similar. This means that the only difference between the ions is the electrical charge, thus eliminating the interference factors. By changing the potential profiles between KCl and nanoparticles, the effect of the potential profiles on the specific heat capacity of nano-salt mixture could be studied in detail.

5.4.1 Properties of KCl Based Nano Mixtures

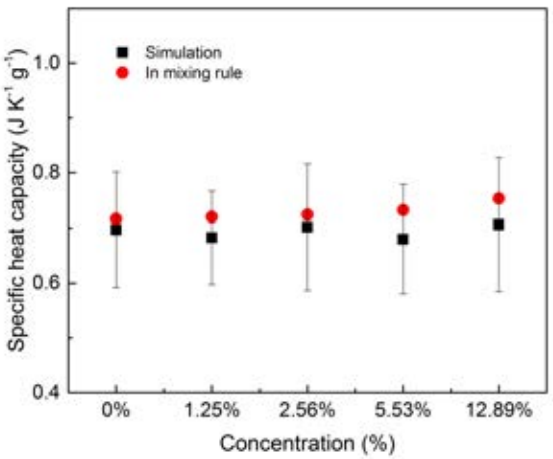

Figure 5.11: Specific heat capacity of the KCl based nanosuspensions in the simulation

Table 5.1 shows the MD simulation results of the KCl salt, whereas the calculated specific heat capacity of the KCl salt containing nanoparticles is given in Figure 5.11. As can be seen, the specific heat capacity of the ionic KCl liquid has not been significantly

Table 5.1: Comparison of experimental and simulated properties of KCl at 1100K

	Experimental	Simulation
Density (g cm^{-3})	1.98 (Solid)	1.67
Specific heat capacity (J K^{-1} g^{-1})	0.69	0.72

enhanced due to the introduction of nanoparticles.

However, results shown in Figure 5.11 are close to the results calculated with the classic mixing rule (in equation 2.5). The number density of the KCl atoms around a nanoparticle is analysed, one obtains Figure 5.12. Clearly, the salt ions are absent within 5 Å because the diameter of the nanoparticle is 1 nm. The normalized number density (ND) increases to around 1.0 at a radial distance greater than 5 Å from the nanoparticle centre. One notices that the number density of Cl atoms changes with the radial distance in a rather smooth pattern while some slight variations can be seen in K atom curve. There is no compression layer with cations and anions separeted as seen in the previous chapter. This leads to the proposal that the existence of the ions in the liquid is not the only factor that causes the enhancement of specific heat capacity.

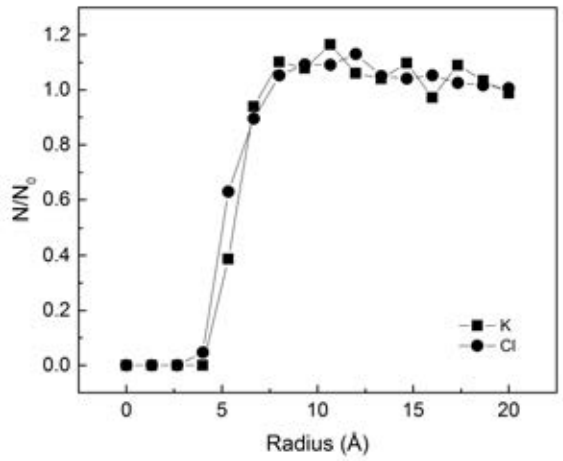

Figure 5.12: Number density of the KCl with 1nm SiO_2 at 1000K in MD simulations

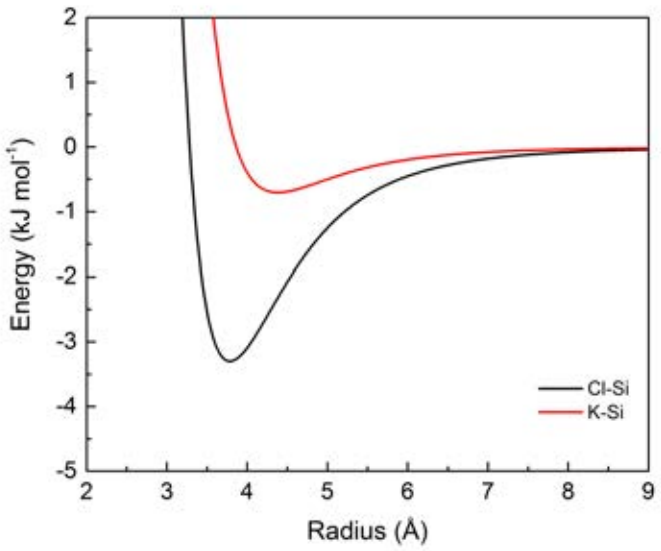

Figure 5.13: Potential energies between a silicon atom and an atom of potassium chloride in the simulation

5.4.2 Simulation Details

Potential profile modification

As mentioned in the previous section, KCl is an ionic liquid when it is melted, with only two different atoms and the atomic mass of the potassium and chloride are similar (39.01 and 35.5). The use of this model system could reveal mechanistic information that could not be easily achieved in other system like nitrate salts. Figure 5.13 shows the vdW potential between salt atoms and silicon atoms in a KCl based nano system. By modifying such potential profiles, one could create "artificial" nano-mixtures to understand how the salt atom arrangement at the adjacent area of the nanoparticle surface affects the specific heat capacity of the nanosalt mixtures. This represents a new approach to study the mechanism potential specific heat capacity enhancement of the salt due to the introduction of nanoparticles.

The force fields were modified in three different ways. First, the depths of the K-Si and K-O potential wells as defined as $E_{K\text{-}Si,well0}$ and $E_{K\text{-}O,well0}$ were changed by multiplying with a vertical shift parameters, S_v with a value from 1 to 4.683, see Figure 5.14). This was to

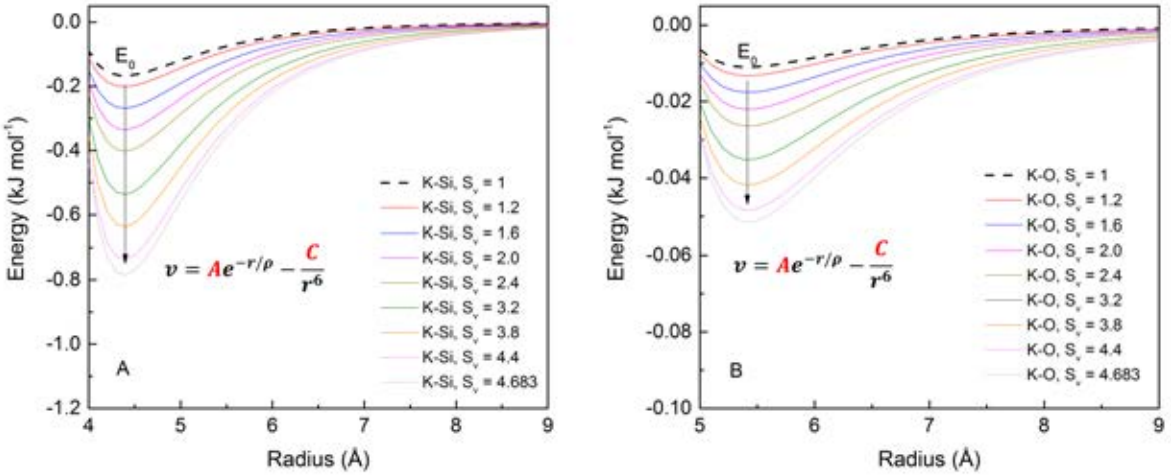

Figure 5.14: Modification of the potential well depth of the KCl based nano system

A: Potential energy profile between potassium and silicon atoms; B: Potential energy profile between potassium and oxygen atoms

study the difference of the depth of the potential well would effect the local arrangement of salt atoms and the specific heat capacity of nano-salt mixture. The dotted line has a $S_v = 1$, which is the potential energy profile based on the original force field shown in Table 3.5. Clearly, the modification of the potential well depth contributes for the K-S interaction. This might cause a stronger attraction force for the potassium atoms near the surface of the nanoparticles. As was shown in 5.13, the potential well of the anion-Si is much deeper than that of the cation-Si. The changes to the potential profile lead to the downward shift to the depth of the potential wells of K-Si and K-O interactions, but diminish the potential well difference for the Cl-Si and Cl-O interactions. At the maximum shift parameter of 4.683, the K-Si potential well has the same well depth as that of Cl-Si potential well, leading to an eliminated potential well difference.

Second, the depth of all potential wells of all salt-nano pairs were modified, see Figure 5.15. The purpose of this was to investigate how such modifications would affect the nature of the "layer", which was hypothetical to be a main factor for the enhancement of specific heat capacity. This manipulation was done by multiplying the potential well depths of all pairs of salt and nanoparticle atoms by the same shift parameter (S_v) over a range from 0.4 to 3.1, to mimic the change of the local polarity and solvent condition[228].

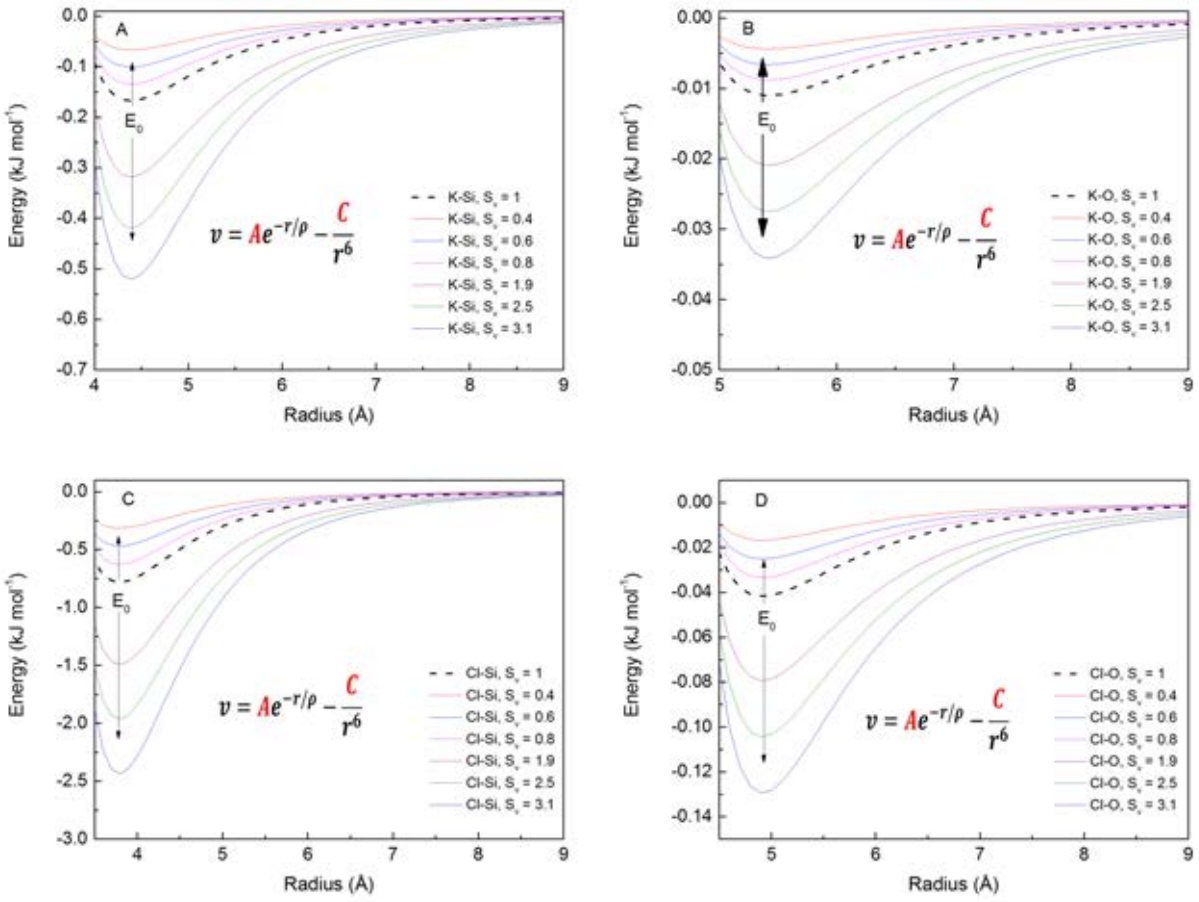

Figure 5.15: Simultaneous wall depth modification to the potential energy in the KCl based nano system

A: Potential energy profile between potassium and silicon atoms; B: Potential energy profile between potassium and oxygen atoms; C: Potential energy profile between chloride and silicon atoms; D: Potential energy profile between chloride and oxygen atoms

The dotted line in Figure 5.15 is for $S_v = 1$, the base case was given in Table 3.5. The potential well moves upwards with a $S_v < 1$, implying that the attractive force decreases between each pair of salt and nanoparticle atoms. The attractive force between the atom pairs increases with a simultaneous increase in the S_v.

Third, the effect of the radius of the potential well of K-Si were examined on the separation of the atoms at the adjacent area of the nanoparticle surface. This was realised in the following manner:

(a) the potential well of cation-Si and anion-Si as shown in Figure 5.13 represents

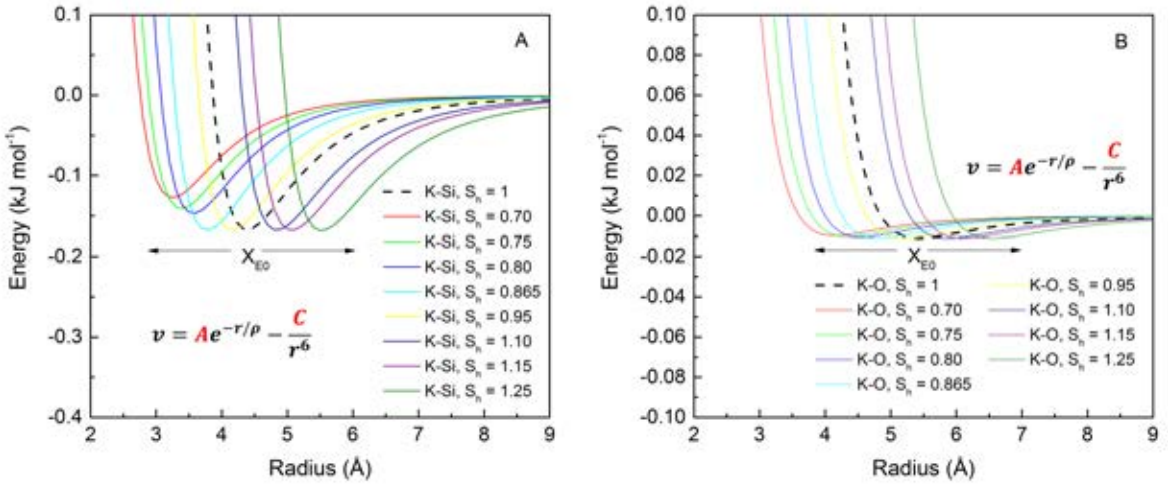

Figure 5.16: Horizontal modification of the potential energy in the KCl based nanosuspension system

A: Potential energy profile between potassium and silicon atoms; B: Potential energy profile between potassium and oxygen atoms

different radius;

(b) multiplying R_0 (Table 3.5) by the horizontal shift parameters (S_h) from 0.65 to 1.25;

(c) the potential profile of the K-Si interaction shift seen horizontally as shown in Figure 5.16.

One can see that, with the S_h of 0.865, the potential wells of K-Si and Cl-Si are at the same radius, implying the elimination of the difference.

Cross Correlation Covariance

In order to describe the phenomenon mathematically, the cross correlation of the normalized ND of K and Cl atoms was analysed. Cross correlation covariance is a standard method for estimating the extent of the correlation of two series, and is given as:

$$\gamma_{XY} = E(X_t - \mu_X)(Y_t - \mu_Y), \tag{5.2}$$

where X_t, Y_t are a pair of stochastic processes. μ_X and μ_Y are the mean of the processes X_t and Y_t, respectively.

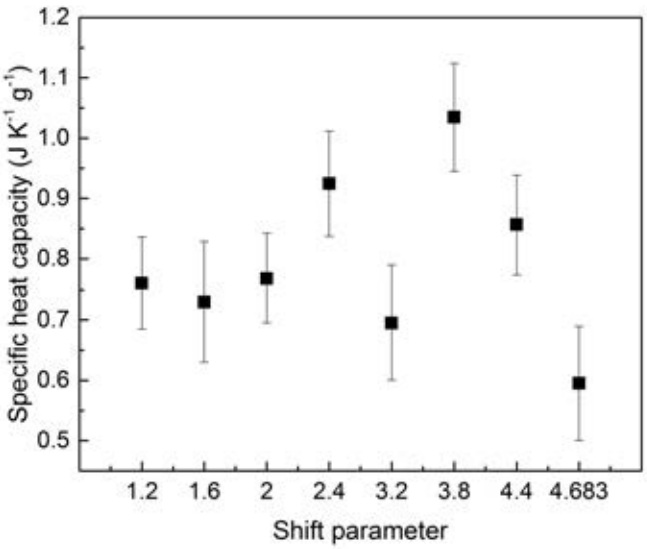

Figure 5.17: Specific heat capacity of the K-silica potential vertically modified KCl based nano mixture against the shift parameters at 1100 °C

γ_{XY} measures the similarity of two series of data and provides information on the extent of the separation of layers. A positive result indicates similar number density of two atoms and hence no separation could be found, whereas a negative result implies the dissimilarity of the atom layers. A cross correlation covariance value of around 0 suggests that the number density of two atoms be unrelated. Since the layering and separation appear at the adjacent area of the surface of a nanoparticle, the cross correlation covariance was calculated in a radius between 7.65 and 12.75Å.

5.4.3 MD Results of the KCl based nano-salt mixture with modified potential profiles

Vertical Modification of the K-silica Potential Energy

Figure 5.17 shows the specific heat capacity of the KCl based nanoparticle-salt mixtures with modified potential profiles as depicted in Figure 5.14.

While the shift parameter (S_v) is 1.2 and 2.0 the specific heat capacity was enhanced by ∼0.8J K^{-1} g^{-1}. 0.4J K^{-1} g^{-1} enhancement was found while S_v was 1.6. The specific heat

capacity increases to its peak of 1.03J K^{-1} g^{-1} with the S_v of 3.8. Then, the specific heat capacity decreases with the increase of S_v. However, on the increasing trend between the S_v of 2 and 3.8, no enhancement of specific heat capacity is observed with the S_v of 3.2.

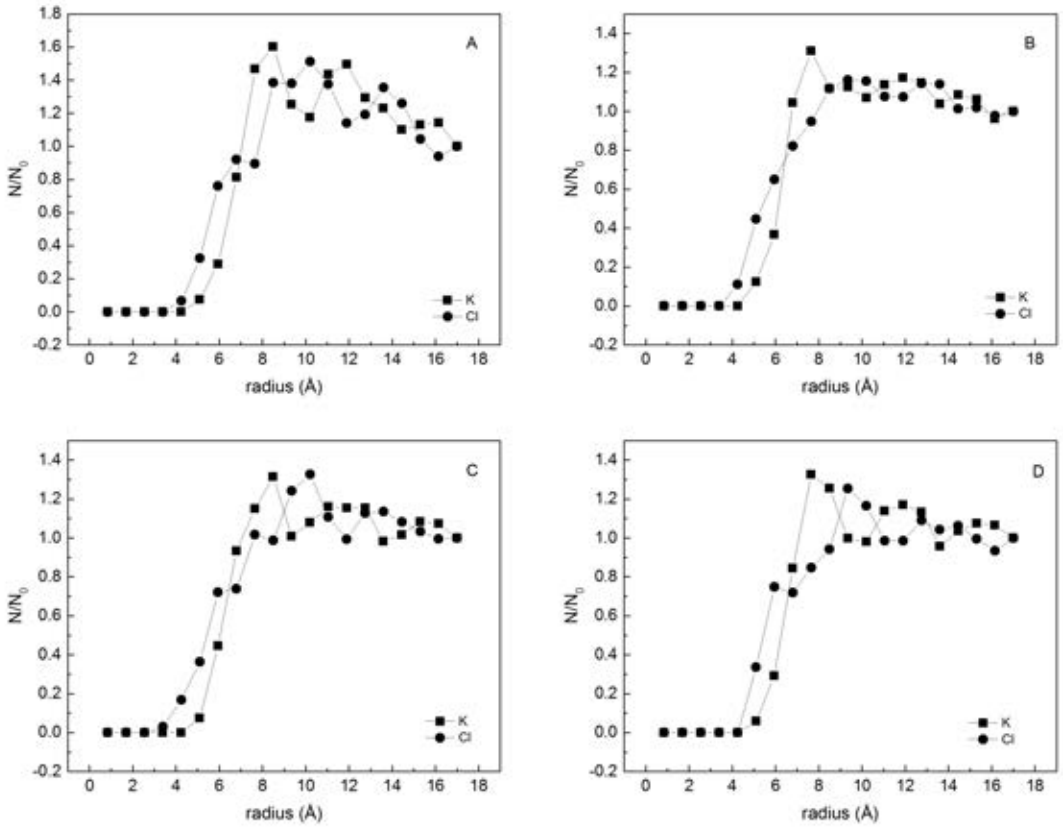

Figure 5.18: Normalized ND of the vertically potential modified nanosuspension systems with the shift parameters from 1.2 to 2.4

A: shift parameters = 1.2; B: shift parameters = 1.6; C: shift parameters = 2.0; D: shift parameters = 2.4

To study the relationship between the specific heat capacity and the arrangement of salt atoms around the nanoparticle, the normalized ND was analysed and the results are shown in Figure 5.18 for S_v = 1.2, 1.6, 2.0 and 2.4. The normalized ND with the S_v of 1.2 is shown in Figure 5.18 A, where layering of K and Cl atoms can be identified. The normalized ND of K increases with increasing radius and the first peak occurs at the radius of 8.5Å with a peak value of 1.60. Followed by a decrease to 1.18 at 10.2Å. At the same radius of 10.2Å, the number density of Cl atoms reaches the first peak of 1.51. This

is followed by a decrease in number density of the Cl, but on increase of the K that reaches its second peak at the radius of 11.9. Beyond the radius of 11.9Å, the number densities of Cl and K are seen to fluctuate and have a decreasing tendency to 1.0. At the shift parameter of 1.6, the number density of K was found at the radius of 7.65. This is followed by a decrease in the peak value to ∼1.05 with a further increase in the radius from 7.65 to 17. No significant peak of Cl atoms could be observed in this case. On the other hand, the normalized ND of the Cl atoms is seen to increase to 1.05 with increasing radius to ∼10Å and fluctuate around 1.05 with a further increase in the radius. The layering and separation phenomenon can be seen in Figure 5.18 C for the shift parameter of 2.0. The normalized ND of K reaches 1.31 at 8.5Å radius whereas that of Cl has a peak of 1.33 at a radius of 10.2Å. The number densities of both atoms then gradually decrease to 1.0 with further increase in the radius to 17Å. Figure 5.18 D represents the normalized ND of the system with a shift parameter of 2.4. As is shown, the K atom is detected at a radius beyond 5Å and the normalized ND increases to 1.32 at a radius of 7.65Å. The normalized ND then decreases with increasing radius, reaching 0.98 at a radius of 10.2Å. The second peak occurs at 11.9Å radius with the normalized ND of 1.17 before approaching 1 with little fluctuation. The Cl number density is seen to reach a peak value of 1.25 at 9.38Å radius and decreases to 1.0 with a further increase in the radius. Small fluctuations are seen with a further increase in the radius to 17Å. The peaks were found at different radius for two atoms, indicating that at the adjacent area of the nanoparticle, a layer is formed with the cation and anion having a higher concentration than the average value in the molten salt. The occurrence of the peak normalized number densities of the K and Cl atoms at different radii implies the separation of the atoms in the layer.

The normalized number densities with the S_v of 3.2, 3.8, 4.4, and 4.68 are shown in Figure 5.19. The specific heat capacity is seen to be enhanced when the S_v is 3.8 and 4.4, whereas no specific heat capacity enhancement for S_v = 3.2 and 4.68 observed. The normalized ND of the system with S_v 3.2 is shown in Figure 5.19A. The first peak of K atoms occurs at 7.65Å radius with a normalized ND of 1.30. The normalized ND

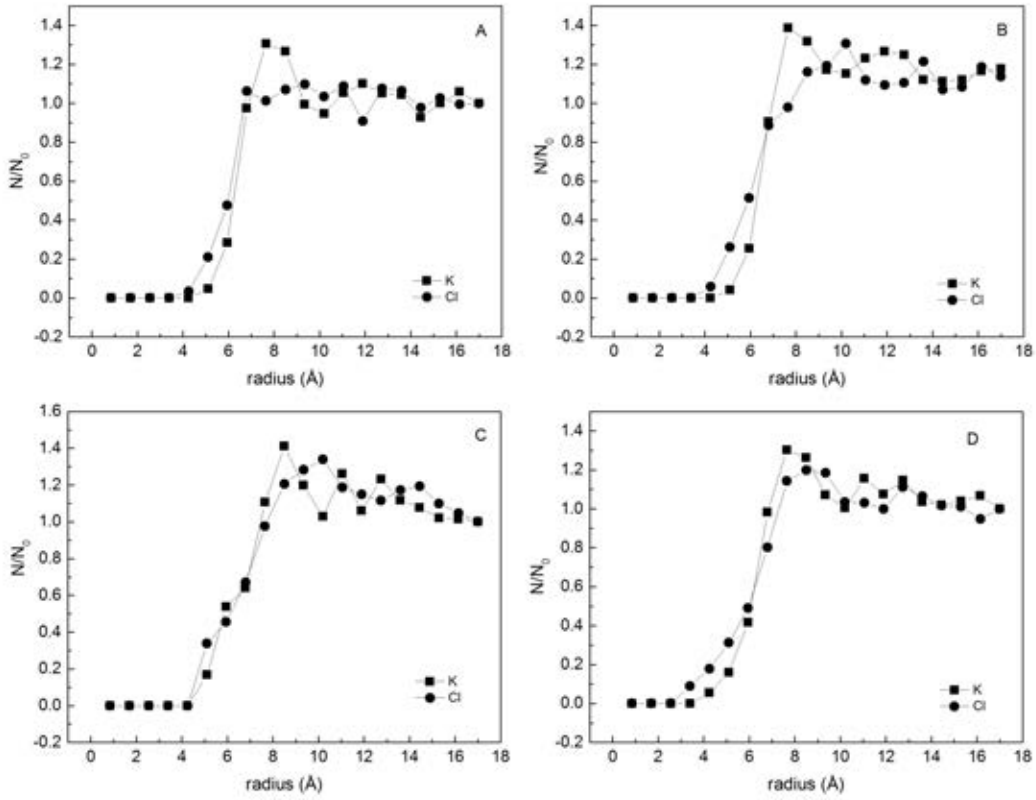

Figure 5.19: Normalized ND with the vertically modified potential function with the S_v from 3.2 to 4.68

A: $S_v = 3.2$; B: $S_v = 3.8$; C: $S_v = 4.4$; D: $S_v = 4.683$

decreases to 0.94 with an increase in the radius to 10.2Å where the normalized ND of the Cl atom is 1.03. With a further increase in the radius, the number densities of both atoms fluctuates around 1.0. A condensed K layer occurs from 7.65 to 8.5Å but no condensed Cl is seen. The results for S_v = 3.8 is shown in Figure 5.19B. One can see an initial increase in the number density of K to 1.39 at a radius of 7.65Å, followed by a decrease to 1.15 at 10.2Å where the normalized ND of the Cl atoms reaches the peak value of 1.31. Then the normalized ND of K atoms reaches the second peak at 11.9Å whereas that of the Cl atoms decreases to 1.09. In Figure 5.19C, the first peak of the normalized ND of K atoms is observed at 8.5Å with a normalized ND of 1.41. At the radius of 10.2, the normalized ND of Cl reaches 1.34 and then decreases with the increase of the radius. With the increase of radius, a decreasing tendency of the normalized ND of both atoms is observed and the normalized ND for both atoms reaches 1.0 at the radius of 17Å. No enhancement was observed in the system with the S_h of 4.68. The normalized ND of this system is shown in Figure 5.19D. The first peak of K atoms is found at the radius of 7.65Å whereas that of the Cl is observed at 8.5Å. The normalized ND of the K and Cl atoms fluctuates around 1.0 with the increase of the radius. No significant separation of K and Cl atoms is observed in the first shell of the system.

It is shown that, unlike the number density graph shown in Figure 5.12 where no significant layering or separation is found, most data in Figure 5.19 exhibit the layering and separation effect in various extents. The exceptions are shown in the systems with $S_v$of 1.6, 3.2 and 4.68. In the system with S_v of 1.6, a thin layer of K is observed whereas no distinct layer of Cl atoms is detected. In the system with S_v of 3.2, only a condensed K layer is found whereas the layer of Cl was not observed. With the S_v of 4.68 a layer containing both K and Cl atoms is observed. However in this layer the peak of the K and Cl atoms appeared at the same radius, which results in the absence of the separation. The specific heat capacity enhancement is not observed in these systems whereas it is found in all systems where the layering and separation phenomenon both occur. This is in good agreement with the phenomenon observed in nitrate salt based nanosuspensions

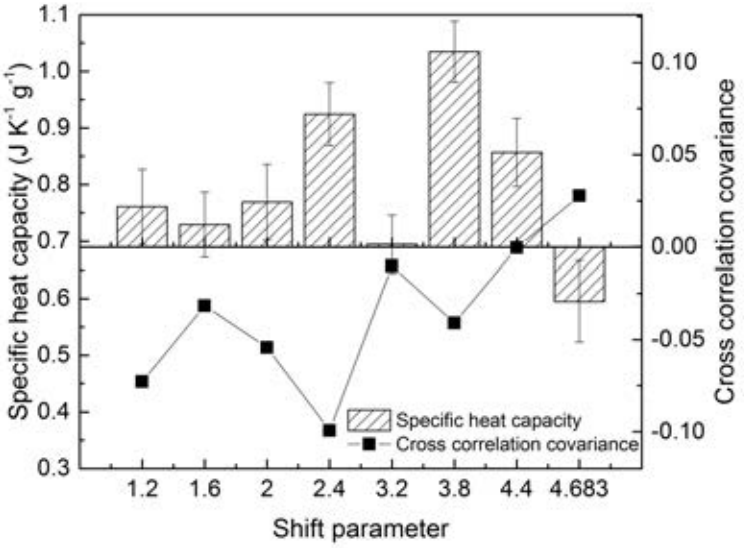

Figure 5.20: Cross correlation covariance and specific heat capacity of the K-silica potential vertically modified KCl based nanosuspensions against the shift parameters at 1100 °C

(In section 5.2) that the specific heat capacity enhancement occurs only if the atom layer and separation exist at the adjacent area of the surface of a nanoparticle.

Figure 5.20 shows the cross correlation covariance and specific heat capacity in the potential vertically modified nanosuspension systems. The cross correlation covariance described the similarity of two groups of number density data. The minus value represented the negative correlation of the number densities. It indicated the separation of K and Cl layers around a nanoparticle. Significant enhancement of specific heat capacity of all systems with the cross correlation covariance lower than -0.04 is observed whereas the enhancement does no occur in the systems where the corresponding cross correlation covariance is found all above -0.04. In the system with the shift parameter of 4.683, the corresponding cross correlation covariance is 0.028 and the specific heat capacity is found to be lower than in the pure salt system.

It can be deduced that the existence of the separated atom layers is related to the specific heat capacity enhancement in the salt based nanosuspension and the enhancement only occurs while the separation of cation and anion is distinct to a certain degree. However the value of the specific heat capacity is not found negatively correlated to the

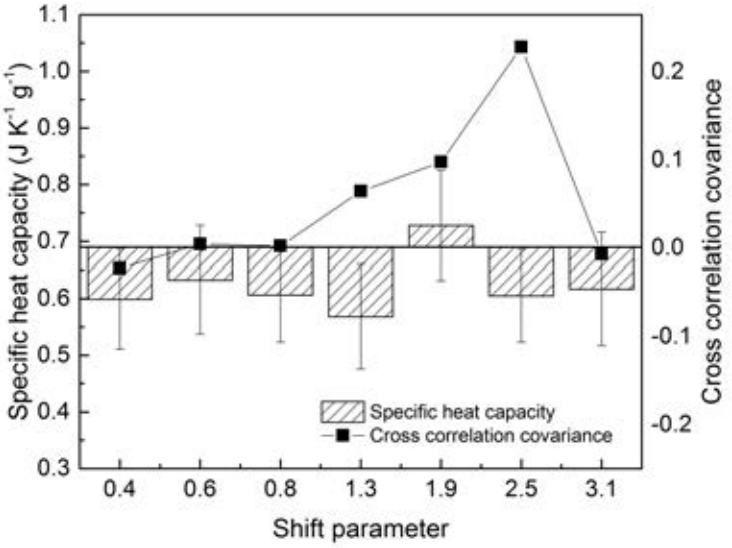

Figure 5.21: Cross correlation covariance and specific heat capacity of the salt-silica potential vertically modified KCl based nanosuspensions against the shift parameters at 1100 °C

cross correlation covariance. The only exception in this graph is found in the system with the shift parameter of 4.4. The specific heat capacity is enhanced considerably while the cross correlation covariance was around 0.

Vertical Modification of the salt-silica Potential Energy

The specific heat capacity of the KCl based nanosuspensions with modified salt-silica potential profiles (Figure 5.15) is shown in Figure 5.21. As is shown, no specific heat capacity enhancement is observed. The lowest specific heat capacity appeared in the system with the shift parameter of 1.3 and it is decreased by 0.13J K^{-1} g^{-1} compared with the original salt system. No enhancement of specific heat capacity of the nanosuspension is observed in the systems with modified salt-silica potential profiles. Most cross correlation covariance data fluctuated around 0 in Figure 5.21. The cross correlation covariance is found to be -0.02 in the system with the shift parameter of 0.4. An increasing tendency of cross correlation covariance is observed with the increase of shift parameter from 0.4 to 2.5 before it decreased to -0.007 with the shift parameter of 3.1. However, the specific heat capacity of the systems is fluctuating near 0.65J K^{-1} g^{-1} and no significant tendency

is found.

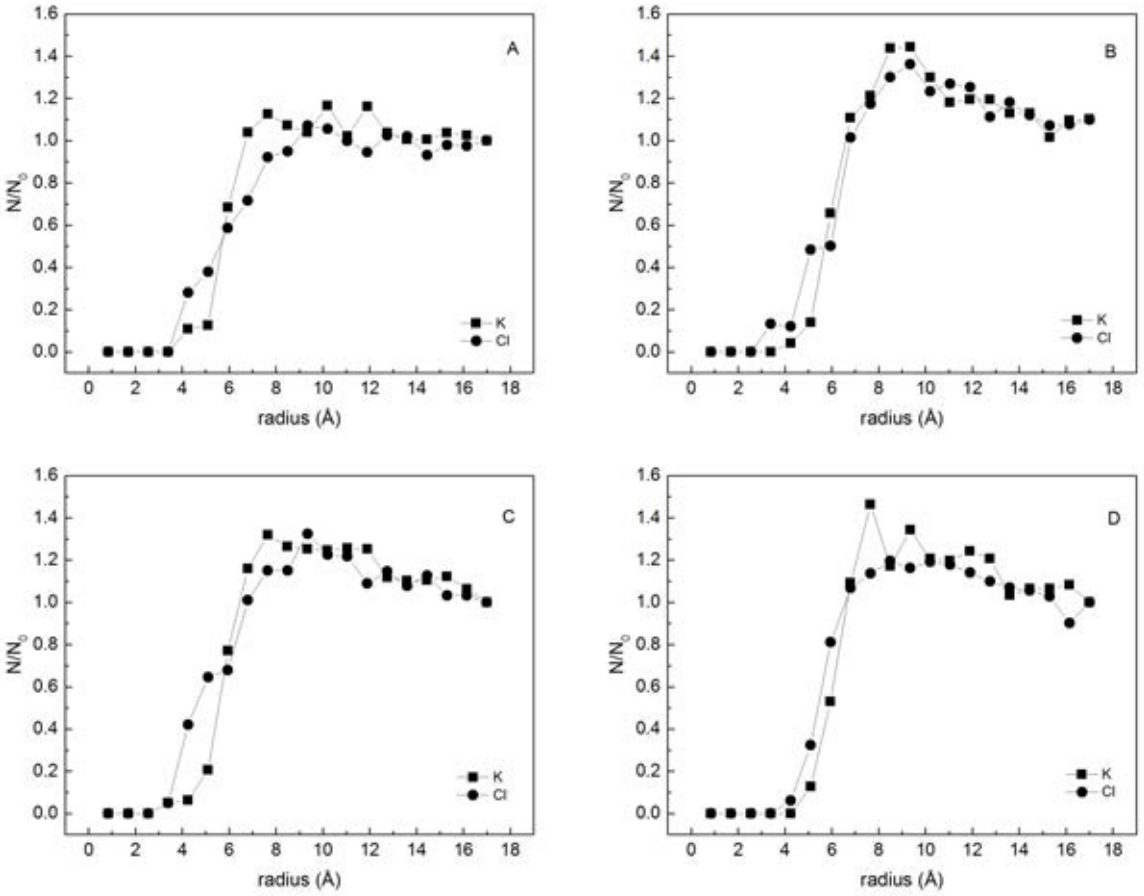

Figure 5.22: Normalized ND of the vertically potential modified nanosuspension systems with the S_v of 0.4, 0.6, 0.8 and 3.1

A: $S_v = 0.4$; B: $S_v = 0.6$; C: $S_v = 0.8$; D: $S_v = 3.1$

Figure 5.22 shows the systems with non-correlated number densities. With the S_v of 0.4, the normalized ND of K and Cl fluctuates around 1.0 with the variation less than 0.2 in the system. No obvious atom layer or separation phenomenon is observed. The first shell of K and Cl is found at the radius of 9.35Å where the overlapping layers are found. In the system with the S_v of 0.8, the normalized ND of K atoms is around 1.25 within the radius of 7.65 and 11.9Å. After an initial ascent to 1.32 at the radius 9.35Å, the normalized ND of K decreases gradually to 1 with slight fluctuations. In the first shell of the Cl, the K atoms is still found ample, which does not form the separation.

The system with the S_v of 3.1 represents a rather different arrangement of atoms around the nanoparticle. There are two peaks of K atoms found at the radius of 7.65 and 9.35Å, respectively. The values of the peaks are 1.46 and 1.34, respectively, and are significantly higher than that of the Cl atoms at the same radius. This implies the existence of the K layers whereas no Cl layer is found at the same region. The normalized ND of the Cl atoms increases with the increase of the radius and reaches 1.2 at the radius of 8.5Å. It stayed at 1.2 with slight fluctuation before it decreases to 1.03 at the radius of 1.36Å.

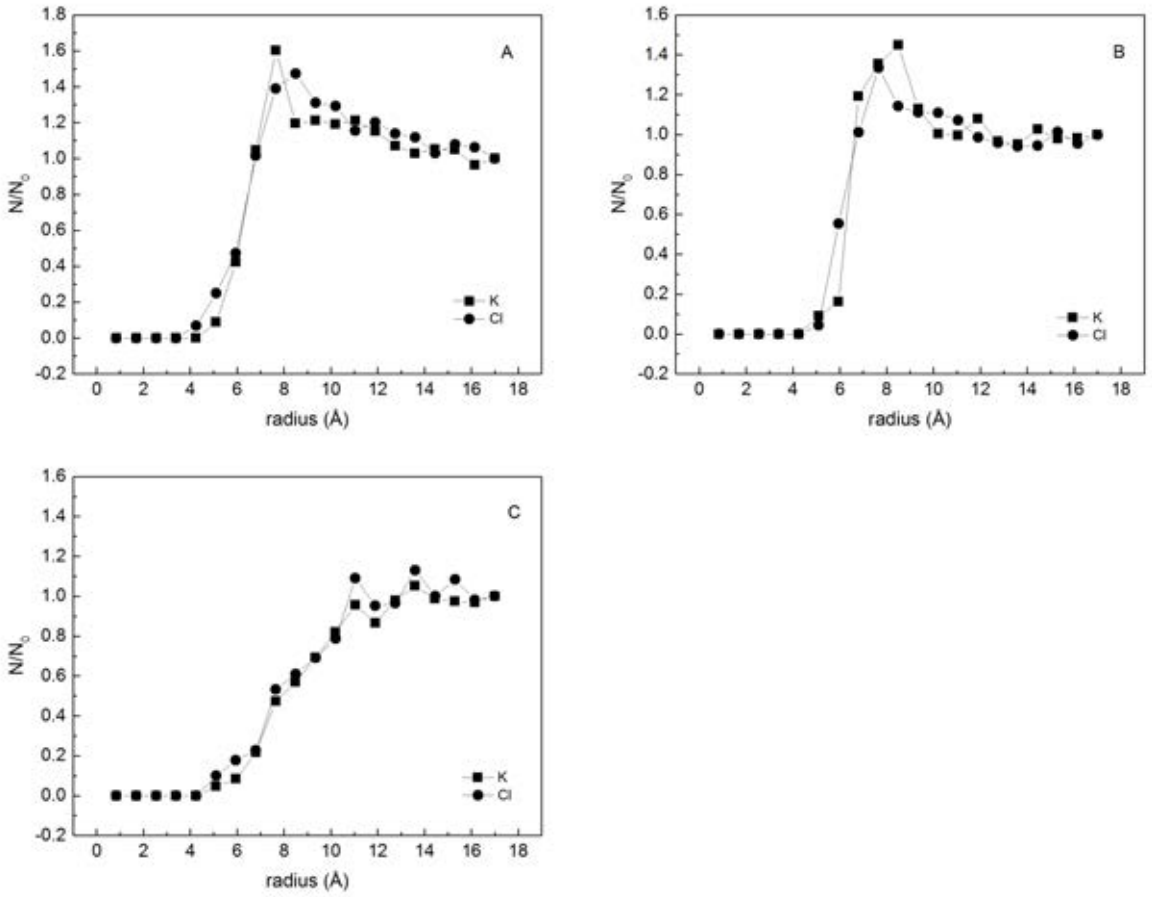

Figure 5.23: Normalized ND of the vertically potential modified nanosuspension systems with the S_v of 1.3, 1.9 and 2.5

A: S_v = 1.3; B: S_v = 1.9; C: S_v = 2.5

The systems with positive cross correlation covariance are shown in Figure 5.23. With the S_v of 1.3, the K and Cl atom peaks are both shown at the radius of 7.65 and 8.5Å,

respectively. The peak of normalized ND of K is 1.60 and that of Cl is 1.47. However, the number density of Cl at the radius of 7.65Å is 1.39 which indicates the presence of concentrated Cl atoms. However, no significant separation is observed because the K layer and Cl layer overlaps at 7.65 and 8.5Å. Similar phenomenon is observed in the system with S_v of 1.9. The peaks of K and Cl are observed at the same radius, and no separation is found. The system with the S_v of 2.5 have the cross correlation covariance of 0.23 which indicated that the number density data of the two atoms are similar to each other. In Figure 5.23 C the peaks of the normalized ND are lower than 1.09 which indicated that the concentration of the atoms in the peak area was only 9% higher than the average value and it is not significant to form a layer.

In the potential profile vertically modified systems, the cross correlation covariance shows that the K and Cl atoms are arranged either positive correspondingly or unrelated. No negative correlation of the number densities is observed and no enhancement of specific heat capacity is found in any of the systems. It indicates that by modifying the salt-silica potential profile vertically, the specific heat capacity is not enhanced.

Horizontal Modification of the K-silica Potential Energy

The specific heat capacity and cross correlation covariance of the systems with horizontally modified K-silica potential (5.16) are shown in Figure 5.24. A decreasing tendency is observed in the specific heat capacity with the increase of the shift parameter. The specific heat capacity in the system with the S_h of 0.7 is 1.15 J K^{-1} g^{-1} which equates to an enhancement of 66.7% compared with the pure KCl salt system. The specific heat capacity slightly decreases to 0.84 J K^{-1} g^{-1} with the S_h of 0.8. With the S_h of 0.865, the potential well of K-Si and Cl-Si is aligned at the same radius. The specific heat capacity is slightly higher than 0.69 J K^{-1} g^{-1} but because of the error bar the enhancement is not significant. By increasing the shift parameter, the potential well of the K-silica interactions moves to the far-side of the nanoparticle (Figure 5.16). The specific heat capacity of the systems with the shift parameter of 0.95, 1.13 and 1.25 are around 0.65 J K^{-1} g^{-1} which is

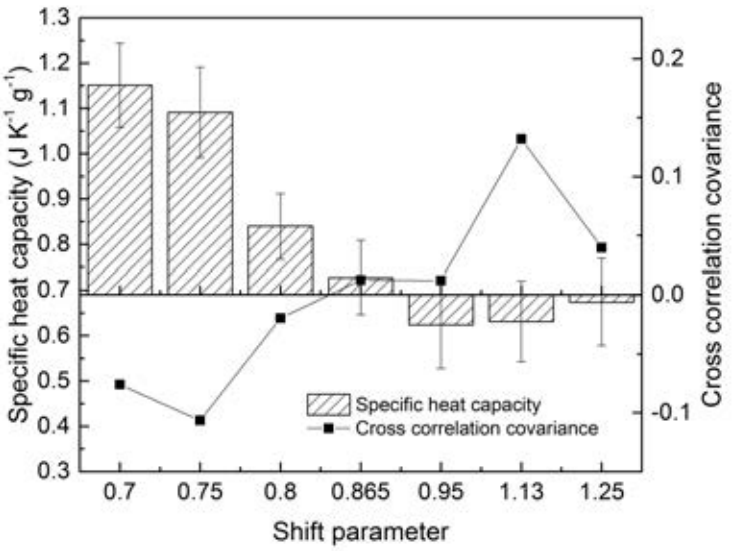

Figure 5.24: Cross correlation covariance and specific heat capacity of the K-silica potential horizontally modified KCl based nanosuspensions against the shift parameters at 1100 °C

slightly lower than that of the pure KCl system. In the systems with the shift parameter of 0.7, 0.75 and 0.8, the specific heat capacities are enhanced. The cross correlation covariance of the system with the S_h of 0.7, 0.75 and 0.8 are -0.076, -0.107 and -0.020, respectively. It indicates the negative correlation between the arrangement of the K and Cl atoms at the adjacent area of a nanoparticle.

The normalized number density of the specific heat capacity enhanced systems is shown in Figure 5.25. With the S_h of 0.7, the first Cl peak appears at the radius of 4.25Å. It indicates that there is a concentrated Cl atom layer at that radius and also the volume of the nanoparticle is compressed because the diameter of the nanoparticle is 10Å. After the first peak, the normalized ND of Cl decreases to 0.57 at the radius of 5.95Å where a K atom layer is formed. The normalized ND of K is 1.63 at the radius of 6.8Å where the that of Cl is 0.70. It created a huge gap between K and Cl atoms in that region and a condensed K layer is formed. Then the normalized number densities oscillates with variation of 0.2 with the increase of radius. The system with the S_h of 0.75 exhibits the peak of Cl normalized ND at the radius of 5.95Å. The normalized ND of K is 0.73 at the radius of 5.95 and increases to 1.28 at 7.65Å where the first peak occurs. Then at

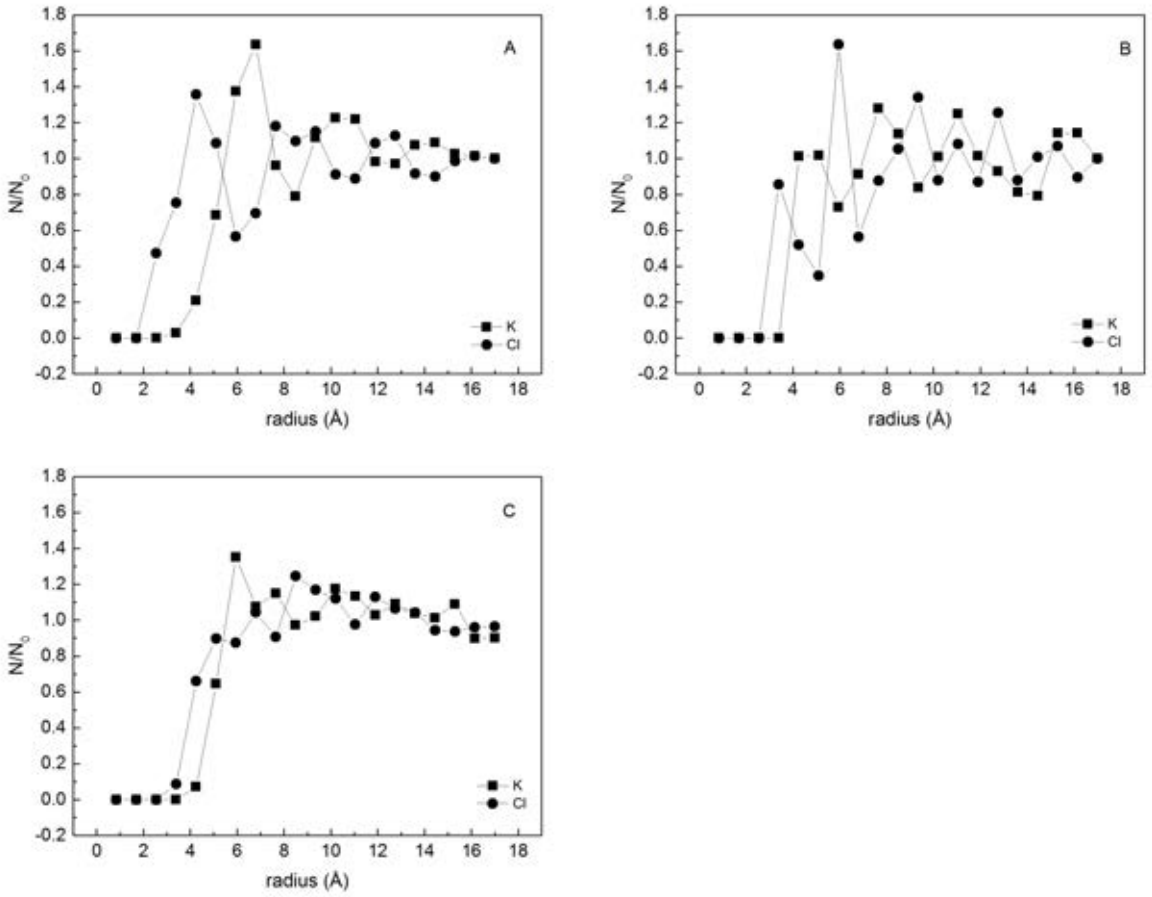

Figure 5.25: Normalized ND of the horizontally potential modified nanosuspension systems with the S_h of 0.7, 0.75 and 0.8

A: $S_h = 0.7$; B: $S_h = 0.75$; C: $S_h = 0.8$

the radius of 9.35Å, the Cl normalized ND is found 1.34 whereas that of the K is 0.84. Obvious formation of atom layers and the separation of them are observed in this system. In the system with the S_h of 0.8, the normalized ND of K is observed 1.35 at the radius of 5.95Å where the first peak is found. It decreased to 0.97 at the radius of 8.5Å where the normalized ND of Cl is at its peak value of 1.24.

The normalized ND data of those systems in which the specific heat capacity are not found enhanced is shown in Figure 5.26. With the S_h of 0.865, the potential well of the K-Si and Cl-Si are vertically aligned. In this system, the normalized ND of both atoms increases with the increase of the radius from 0 to 7.65Å. The peak of K is found 1.23 at

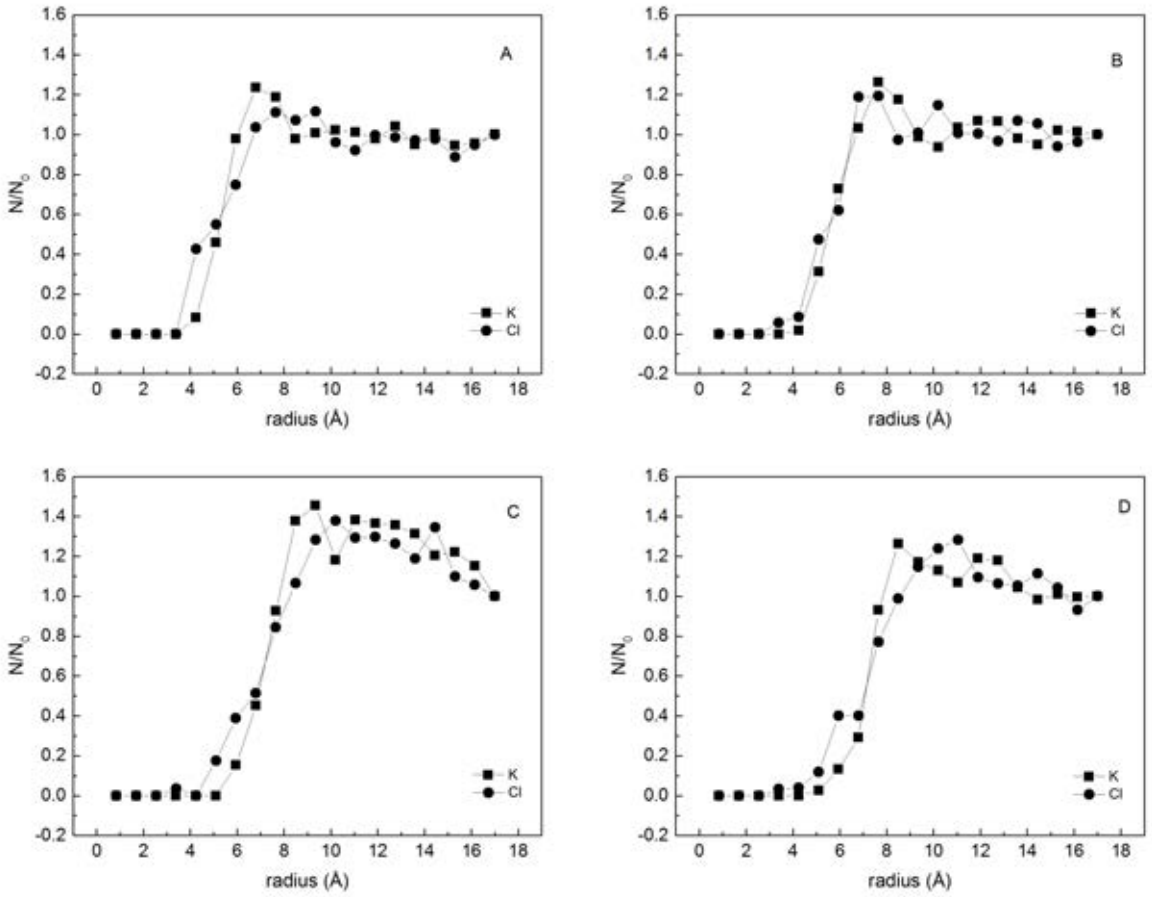

Figure 5.26: Normalized ND of the horizontally potential modified nanosuspension systems with the S_h of 0.865, 0.95, 1.13 and 1.25

A: S_h = 0.865; B: S_h = 0.95; C: S_h = 1.13; D: S_h = 1.25

the radius of 6.8Å whereas that of Cl is 1.12 at 7.65Å. No obvious separation is observed in this system, which implies that aligning the potential well vertically did not change the atom arrangement significantly. The peaks of both atoms appears at the radius of 7.65Å in the system with the S_h of 0.95. The normalized ND of Cl is higher than that of K by 0.21 at the radius of 9.35Å. In the system with the S_h of 1.13, the normalized number densities of K and Cl have very similar tendency through the whole radius except that at the radius of 10.2 and 14.45Å two slight variations are observed in the figure. No significant layer or separation are observed in this system. In the system with the S_h of 1.25, layers of K and Cl are found at the radius of 8.65 and 11.05Å, respectively. However the number density

difference in those layers are found insignificant. Also the cross correlation covariance of this system shown in Figure 5.24 exhibits that the two groups of number densities are irrelevant. The specific heat capacity is only found enhanced in the systems where cross correlation covariance is negative. While the cross correlation covariance is around 0 or positive, the specific heat capacity is not enhanced.

5.5 Discussion and Summary

In the MD simulation, a compressed layer containing Na^+ and NO_3^- is found at the adjacent area of a nanoparticle in the $NaNO_3$ based nanosuspensions. The coulombic force introduced by nanoparticles caused the formation of the compressed ion layer which caused the enhancement of specific heat capacity.

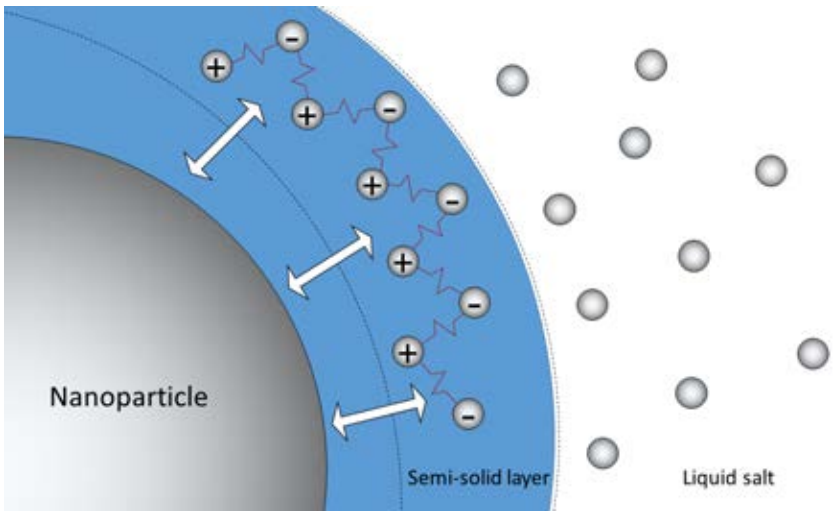

Figure 5.27: The semi-solid layer in the salt based nanosuspensions

By modifying the potential profiles between certain atoms with three different methods in the KCl based nanosuspension systems, the relationship between the specific heat capacity enhancement and the atom arrangement at the adjacent area of a nanoparticle are discussed. All data are summarized in Table 5.2. In most of the systems, specific heat capacities are significantly enhanced in all systems with the cross correlation covariance smaller than -0.041. Only two exceptions are found in the simulation. Also with the cross

correlation covariance around 0 or above, the specific heat capacity is not enhanced. It further proves that the separation of the compressed layers happens along with the specific heat capacity enhancement. In all specific heat capacity enhanced systems, a "compressed" layer is formed by cations and anions in a certain arrangement at the adjacent area of the surface of a nanoparticle. The separation of the cations and anions creates a stable semi-solid structure. The cations and anions in this layer causes an anomalous increase in the thermal resistance which could store additional potential energy because of the vibration energies[155, 163]. This also explains the thermal conductivity change in Figure 4.25. The decreasing tendency is caused by the resistant layer and while the volume of nanoparticles is great enough, the high conductive nanoparticle become the dominant factor of enhancing the system thermal conductivity. Hence the increase of thermal conductivity at higher fraction of particles is explained.

Table 5.2: The Specific Heat Capacity Enhancement and Cross Correlation Covariance in Various Systems

Type	Shift Parameter	Specific Heat Capacity Enhancement (%)	Cross Correlation Covariance
$V_{K\text{-}Silica}$[a]	1.2	10.29	-0.073
	1.6	5.73	-0.032
	2	11.44	-0.054
	2.4	33.98	-0.099
	3.2	0.736	-0.010
	3.8	49.93	-0.041
	4.4	24.18	-0.000
	4.683	-13.78	0.028
$V_{Salt\text{-}Silica}$[b]	0.4	-13.21	-0.023
	0.6	-8.33	0.004
	0.8	-12.16	0.002
	1.3	-17.68	0.064
	1.9	5.52	0.098
	2.5	-12.33	0.228
	3.1	-10.64	-0.007
$H_{K\text{-}Silica}$[c]	0.7	66.83	-0.076
	0.75	58.13	-0.107
	0.8	21.74	-0.020
	0.865	5.42	0.013
	0.95	-9.61	0.012
	1.13	-8.51	0.132
	1.25	-2.32	0.040

a: The potential profile of K-Si and K-O were vertically modified; b: The potential profile of K-Si, K-O, Cl-Si and Cl-O were vertically modified; c: The potential profile of K-Si and K-O were horizontally modified.

CHAPTER 6

CONCLUSION AND FUTURE WORK

6.1 Summary

The main aim of the research conducted in this thesis was to understand the thermal behaviour of nitrate molten salt based nanosuspensions and the mechanism of how nanoparticles altered it. Varying mass fraction of SiO_2 nanoparticles in different sizes were added to three nitrate salts, respectively, and the thermal properties of them measured with DSC, LFA and other techniques. An method using a ultrasonic probe for the preparation of the salt based nanosuspensions was used. The impact of different factors of the nanoparticles on the thermal properties of molten salts was studied in the experiments. The structure of the nanosuspensions after cycling was analysed and observed with XRD and SEM to characterise the dispersion of nanoparticles. MD simulations were employed to study the thermal properties of nanosuspensions with different salts and nanoparticles and understand the interaction between nanoparticles and salt atoms. In the nitrate salt systems, the alternation of the potential energies caused by the introduction of nanoparticles was observed and the mechanism of how nanoparticle affect the thermal properties was studied. In the simulation, an unreported atom arrangement of molten salt atoms is observed at the adjacent area of the surface of a nanoparticle, which is capable of explaining the mechanism of the thermal properties alternation.

It was observed in the experiments that the specific heat capacity of salt based nanosuspensions can not be simply calculated with the classic thermal equilibrium model. 1-5μm SiO_2 particles were mixed with salts to compare the results with the nanosuspensions and it was found that in all salts the enhancement of specific heat capacity is less than 5.3% which implies that the enhancement is caused by variation considering the intertwined error bars. After screening the specific heat capacity of the nanosuspensions, the best parameter sets are determined. For $NaNO_3$ based nanosuspensions with 0.5% of 60-70nm SiO_2 nanoparticles, the highest specific heat capacity was enhanced by 27.6% compared with the pure salt. With 1% of 60-70nm nanoparticles, the specific heat capacity of KNO_3 was enhanced by 17.6%. The $LiNO_3$ salt containing 0.5% 20-30nm nanoparticles exhibits the highest specific heat capacity which was 2.14J K^{-1} g^{-1}. The enhancement was

weakened while the nanoparticle fraction is over 2% and I propose that it is because the aggregation of nanoparticles which significantly diminishes the surface area of nanoparticles. The smaller nanoparticles do not represent higher specific heat capacity enhancing capability in the experiments and 60-70nm nanoparticles are generally considered the best candidate because smaller nanoparticles aggregate faster than the bigger ones[227] and ended up compromising more surface area.

The melting point of most nanosuspensions has a negative correlation with the fraction of nanoparticles in the experiment. No change of melting point was observed while 60-70nm nanoparticles or 1-5μ particles are added into $NaNO_3$ whereas the smaller particles tend to decrease the melting point. A decreasing tendency of melting point was found with the fraction of all particles in KNO_3. The melting point of $LiNO_3$ had a decrease after the initial increment with the increase of the particle fraction. Overall, the melting points of molten salts were not significantly changed as the most distinct change is less than 3 °C.

Latent heat of the salts was changed with the introduction of nanoparticles. It was shown that while the fraction of the nanoparticles are not greater than 2%, no significant change of the latent heat is observed. With 4% of nanoparticles, the latent heat of $NaNO_3$ decreased by 7% whereas that of KNO_3 and $LiNO_3$ are 2% and 10%, respectively.

Through XRD analysis, I found that the addition of nanoparticles does not change the crystal structure of the salts during the cycles. Agglomeration of nanoparticles is found in nanosuspensions and a strip-like pattern of aggregation was observed. It proves the assumption of the aggregation of nanoparticles that causes the decrease of specific heat capacity when more than 2% nanoparticles are introduced.

The experiment results indicate that by adding SiO_2, the thermal conductivity of salts is not enhanced, on the contrary, all sample receive a decrease of thermal conductivity with the introduction of the particles regardless of the higher conductivity that SiO_2 possesses. I propose that a high thermal resistance layer existed between the nanoparticle and molten salts and hence the thermal conductivity of the system decreases.

In the MD simulation, by introducing SiO_2 nanoparticles, significant enhancement of the specific heat capacity is observed in nitrate salt based nanosuspensions whereas it is not found in water based nanosuspensions. The enhancement is positively correlated to the mass fraction of particles and that cannot be explained with the classic thermal equilibrium model.

Through RDF and number density analysis, a solid-like "compressed" layer was found in the molten salt at the adjacent area of the surface of a nanoparticle. The separation of cations and anions is found in the layer based on the observation of number densities of different ions. This phenomenon is not reported before or found in the pure salt. It is formed because of the coulombic force introduced by nanoparticles and causes the atoms within trapped in a potential well which limits the kinetic energy of them during a heating process. It eventually causes a enhancement of specific heat capacity in the layer.

By modifying the potential profiles between certain atoms with three different methods in the KCl based nanosuspension systems, the relation between the specific heat capacity enhancement and the atom arrangement at the adjacent area of a nanoparticle is discussed. I first report the connection between the specific heat capacity and the "compressed" layer. The specific heat capacity enhancement is observed only in the systems where the "compressed" layer and the segregation of cation and anions both appear.

The MD simulation for the first time supports two of the existing theories[3]. That theory proposes there is a layer of semi-solid molecules adhering to the surface of a nanoparticle and the enhancement is due to the reduced inter-molecular spacing and semi-solid behaviour of this layer. I agree with the existence of the atom layer near the nanoparticle and observe a separation of cations and anions in the layer. Moreover, I propose the reason of the formation of the layer and the results in the study indicate that it is the coulombic force causes this enhancement, which explains why it only happens in salt based nanosuspensions but not water or other non-ionic liquids. The thermal resistance in the layer also increases because of the special arrangement of atoms and stored extra energy to cause the enhancement of specific heat capacity.

6.2 Future Work

Based on the experimental results, the aggregation hinders the capability of nanoparticles of enhancing the specific heat capacity. A more effective method of dispersing nanoparticles in salt should be investigated. Based on the enhancement of the specific heat capacity that nanoparticles causes, economical analysis should be taken to balance the output and profit of the technology in an industrial scale.

We have observed the relation between the enhancement of specific heat capacity and salt atom arrangement around a nanoparticle but have found the quantified relation between them. Future work should be taken to investigate how the interaction between salt and nanoparticles would affect the specific heat capacity and to establish a more detailed relation between them.

BIBLIOGRAPHY

[1] Murat M Kenisarin. "High-temperature phase change materials for thermal energy storage". In: *Renewable and Sustainable Energy Reviews* 14.3 (2010), pp. 955–970.

[2] George J Janz. *Molten salts handbook*. Elsevier, 2013.

[3] Donghyun Shin and Debjyoti Banerjee. "Enhancement of specific heat capacity of high-temperature silica-nanofluids synthesized in alkali chloride salt eutectics for solar thermal-energy storage applications". In: *International journal of heat and mass transfer* 54.5 (2011), pp. 1064–1070.

[4] Jacopo Buongiorno. "Convective transport in nanofluids". In: *Journal of Heat Transfer* 128.3 (2006), pp. 240–250.

[5] S Zhou and Rui Ni. "Measurement of the specific heat capacity of water-based Al_2O_3 nanofluid". In: *Applied Physics Letters* 92.9 (2008), p. 093123.

[6] Le-Ping Zhou et al. "On the specific heat capacity of CuO nanofluid". In: *Advances in mechanical engineering* 2 (2010), p. 172085.

[7] Donghyun Shin and Debjyoti Banerjee. "Enhanced specific heat of silica nanofluid". In: *Journal of heat transfer* 133.2 (2011), p. 024501.

[8] Dennis C Rapaport. *The art of molecular dynamics simulation*. Cambridge university press, 2004.

[9] Florian Müller-Plathe. "A simple nonequilibrium molecular dynamics method for calculating the thermal conductivity". In: *The Journal of chemical physics* 106.14 (1997), pp. 6082–6085.

[10] Simone Melchionna, Giovanni Ciccotti, and Brad Lee Holian. "Hoover NPT dynamics for systems varying in shape and size". In: *Molecular Physics* 78.3 (1993), pp. 533–544.

[11] William G Hoover. "Canonical dynamics: equilibrium phase-space distributions". In: *Physical Review A* 31.3 (1985), p. 1695.

[12] SM Hasnain. "Review on sustainable thermal energy storage technologies, Part I: heat storage materials and techniques". In: *Energy Conversion and Management* 39.11 (1998), pp. 1127–1138.

[13] Antoni Gil et al. "State of the art on high temperature thermal energy storage for power generation. Part 1-Concepts, materials and modellization". In: *Renewable and Sustainable Energy Reviews* 14.1 (2010), pp. 31–55.

[14] Tarik Kousksou et al. "Energy storage: Applications and challenges". In: *Solar Energy Materials and Solar Cells* 120 (2014), pp. 59–80.

[15] Keith Lovegrove, Andreas Luzzi, and Holger Kreetz. "A solar-driven ammonia-based thermochemical energy storage system". In: *Solar Energy* 67.4 (1999), pp. 309–316.

[16] Rainer Tamme. "Concrete storage: update on the German concrete TES program". In: *Workshop on Thermal Storage for Trough Power Systems, February.* 2003, pp. 20–21.

[17] Rainer Tamme, Wolf-Dieter Steinmann, and Doerte Laing. "Thermal energy storage technology for industrial process heat applications". In: *ASME 2005 International Solar Energy Conference.* American Society of Mechanical Engineers. 2005, pp. 417–422.

[18] Fredrik Stahl. *Influence of thermal mass on the heating and cooling demands of a building unit.* Chalmers University of Technology, 2009.

[19] SM Hasnain et al. "Energy Research Institute-Internal Report". In: *KACST, Riyadh, Saudi Arabia* (1996).

[20] Randy J Petri, ET Ong, and LG Marianowski. *High-temperature composite thermal energy storage for industrial applications*. Tech. rep. Institute of Gas Technology, Chicago, IL (USA), 1985.

[21] Maria E Navarro et al. "Selection and characterization of recycled materials for sensible thermal energy storage". In: *Solar Energy Materials and Solar Cells* 107 (2012), pp. 131–135.

[22] T Kousksou et al. "Numerical simulation of fluid flow and heat transfer in a phase change thermal energy storage". In: *International journal of energy technology and policy* 6.1-2 (2008), pp. 143–158.

[23] T Kousksou et al. "Dynamic modelling of the storage of an encapsulated ice tank". In: *Applied Thermal Engineering* 25.10 (2005), pp. 1534–1548.

[24] MAK Lodhi. "Solar ponds in alkaline lake and oil well regions". In: *Energy conversion and management* 37.12 (1996), pp. 1677–1694.

[25] Daniel M Blake et al. "New heat transfer and storage fluids for parabolic trough solar thermal electric plants". In: *Conference new heat transfer and storage fluids for parabolic trough solar thermal electric plants*. 2002.

[26] Rebecca I Dunn, Patrick J Hearps, and Matthew N Wright. "Molten-salt power towers: newly commercial concentrating solar storage". In: *Proceedings of the IEEE* 100.2 (2012), pp. 504–515.

[27] T El Rhafiki et al. "Crystallization of PCMs inside an emulsion: supercooling phenomenon". In: *Solar Energy Materials and Solar Cells* 95.9 (2011), pp. 2588–2597.

[28] T Kousksou et al. "Second law analysis of latent thermal storage for solar system". In: *Solar energy materials and solar cells* 91.14 (2007), pp. 1275–1281.

[29] Tarik Kousksou et al. "Power, efficiency and irreversibility of latent energy systems". In: *Journal of Thermophysics and Heat Transfer* 22.2 (2008), pp. 234–239.

[30] Ibrahim Dincer and Marc Rosen. *Thermal energy storage: systems and applications*. John Wiley & Sons, 2002.

[31] Atul Sharma et al. "Review on thermal energy storage with phase change materials and applications". In: *Renewable and Sustainable energy reviews* 13.2 (2009), pp. 318–345.

[32] Qi Cao and Pengsheng Liu. "Hyperbranched polyurethane as novel solid–solid phase change material for thermal energy storage". In: *European Polymer Journal* 42.11 (2006), pp. 2931–2939.

[33] A Abhat. "Low temperature latent heat thermal energy storage: heat storage materials". In: *Solar energy* 30.4 (1983), pp. 313–332.

[34] J Schröder and K Gawron. "Latent heat storage". In: *International Journal of Energy Research* 5.2 (1981), pp. 103–109.

[35] Neven Ukrainczyk, Stanislav Kurajica, and Juraj Šipušić. "Thermophysical comparison of five commercial paraffin waxes as latent heat storage materials". In: *Chemical and Biochemical Engineering Quarterly* 24.2 (2010), pp. 129–137.

[36] DV Hale, MJ Hoover, and MJ ONeill. "Phase change materials handbook". In: (1971).

[37] Syukri Himran, Aryadi Suwono, and G Ali Mansoori. "Characterization of alkanes and paraffin waxes for application as phase change energy storage medium". In: *Energy Sources* 16.1 (1994), pp. 117–128.

[38] Eugene S Domalski, William H Evans, and Elizabeth D Hearing. *Heat Capacities and Entropies of Organic Compounds in the Condensed Phase*. American Chemical Society, 1984. ISBN: 0883184478.

[39] HP Garg, SC Mullick, and Vijay K Bhargava. *Solar thermal energy storage*. Springer Science & Business Media, 2012.

[40] George Ashel Lane. "Solar heat storage: latent heat materials". In: (1983).

[41] TRC Thermodynamic Tables. "Hydrocarbons". In: *Thermodynamic Research Center, The Texas A & M University System: College Station, TX* (1987).

[42] Jean Timmermans et al. "Physico-chemical constants of pure organic compounds". In: (1950).

[43] Ahmet Sarı. "Thermal reliability test of some fatty acids as PCMs used for solar thermal latent heat storage applications". In: *Energy Conversion and Management* 44.14 (2003), pp. 2277–2287.

[44] George A Lane et al. "Heat of fusion systems for solar energy storage". In: *Proc. Workshop on Solar Energy Storage Subsystems for the Heating and Cooling of Buildings*. 1975, pp. 43–55.

[45] CS Herrick and DC Golibersuch. *Qualitative behavior of a new latent heat storage device for solar heating/cooling systems*. General Electric Company Corporate Research and Development, 1977.

[46] D Feldman, MM Shapiro, and D Banu. "Organic phase change materials for thermal energy storage". In: *Solar energy materials* 13.1 (1986), pp. 1–10.

[47] George A Lane. "Low temperature heat storage with phase change materials". In: *International Journal of Ambient Energy* 1.3 (1980), pp. 155–168.

[48] Ahmet Sarı and Kamil Kaygusuz. "Thermal performance of myristic acid as a phase change material for energy storage application". In: *Renewable Energy* 24.2 (2001), pp. 303–317.

[49] Hiroyuki Kumano et al. "Study on latent heat of fusion of ice in aqueous solutions". In: *International Journal of Refrigeration* 30.2 (2007), pp. 267–273.

[50] CE Birchenall and M Telkes. "Thermal storage in metals". In: *Sharing the Sun: Solar Technology in the Seventies, Volume 8*. Vol. 8. 1976, pp. 138–154.

[51] C Ernest Birchenall and Alan F Riechman. "Heat storage in eutectic alloys". In: *Metallurgical and Materials Transactions A* 11.8 (1980), pp. 1415–1420.

[52] AS Trunin. "Designing and investigations of salt systems for solar energy utilization". In: *Utilization of sun and other radiation sources in materials research. Kiev: Naukova Dumka* (1983), pp. 228–38.

[53] George J Janz et al. *Physical properties data compilations relevant to energy storage. II. Molten salts: data on single and multi-component salt systems.* Tech. rep. Rensselaer Polytechnic Inst., Troy, NY (USA). Cogswell Lab., 1979.

[54] N Araki et al. "Measurement of thermophysical properties of molten salts: mixtures of alkaline carbonate salts". In: *International journal of thermophysics* 9.6 (1988), pp. 1071–1080.

[55] Y Takahashi, R Sakamoto, and M Kamimoto. "Heat capacities and latent heats of LiNO3, NaNO3, and KNO3". In: *International Journal of Thermophysics* 9.6 (1988), pp. 1081–1090.

[56] LG Marianowski and HC Maru. "Latent heat thermal energy storage systems above 450 C". In: *12th Intersociety Energy Conversion Engineering Conference.* Vol. 1. 1977, pp. 555–566.

[57] HC Maru et al. "Molten salts energy storage systems". In: *Final Report of the Institute of Gas Technology, Chicago* (1978).

[58] Thomas Bauer et al. "Sodium nitrate for high temperature latent heat storage". In: (2009).

[59] L Ye et al. "The thermal physical properties and stability of the eutectic composition in a Na_2CO_3NaCl binary system". In: *Thermochimica Acta* 596 (2014), pp. 14–20.

[60] TV Gubanova, IM Kondratyuk, and IK Garkushin. "Phase equilibria in the LiF-LiCl-LiVO3-Li2CrO4 quaternary system". In: *Russian journal of inorganic chemistry* 49.7 (2004), pp. 1087–1090.

[61] TV Gubanova and IK Garkushin. "LiF-LiCl-$LiVO_3$-Li_2SO_4-Li_2MoO_4 system". In: *Russian Journal of Inorganic Chemistry* 52.10 (2007), pp. 1624–1628.

[62] TV Gubanova, IM Kondratyuk, and IK Garkushin. "The LiF-LiCl-Li2SO4-Li2MoO4 quaternary system". In: *Russian journal of inorganic chemistry* 51.3 (2006), pp. 474–477.

[63] Wayne M Phillips and Jonn W Stearns. "Advanced latent heat of fusion thermal energy storage for solar power systems". In: *20th Intersociety Energy Conversion Engineering Conference, Volume 2*. Vol. 2. 1985, p. 2.

[64] Kenneth E Mayo et al. "Heat source systems". US 3605720. Sept. 1971.

[65] NA Vasina et al. "Heat storage composition". In: USSR 1102800 (1984).

[66] JL Eichelberger and HD Gillman. "Investigation of metal fluoride thermal energy storage materials". In: *12th Intersociety Energy Conversion Engineering Conference*. Vol. 1. 1977, pp. 567–574.

[67] GR Heidenreich and MB Parekh. "Thermal energy storage for organic Rankine cycle solar dynamic space power systems". In: *IECEC'86; Proceedings of the Twenty-first Intersociety Energy Conversion Engineering Conference*. Vol. 1. 1986, pp. 791–797.

[68] TV Gubanova and IK Garkushin. "Three-component systems LiF-LiVO3-Li2MoO4and LiVO3-Li2SO4-Li2MoO4". In: *Russian journal of inorganic chemistry* 50.11 (2005), pp. 1772–1775.

[69] BD Babaev and AM Gasanaliev. "Phase Diagram of the System LiF–NaF–CaF2–BaF2–BaMoO4". In: *Inorganic materials* 39.11 (2003), pp. 1203–1207.

[70] NN Verdiev, PA Arbukhanova, and EG Iskenderov. "NaF-NaBr-Na2MoO4 and KF-KCl-KBr ternary systems". In: *Russian Journal of Inorganic Chemistry* 54.1 (2009), pp. 128–133.

[71] IK Garkushin et al. "Heat storage fluoride composition". USSR 1018957. 1983.

[72] Ajay K Misra and J Daniel Whittenberger. "Fluoride salts and container materials for thermal energy storage applications in the temperature range 973 to 1400 K". In: (1987).

[73] JD Whittenberger and AK Misra. "Identification of salt-Alloy combinations for thermal energy storage applications in advanced solar dynamic power systems". In: *Journal of Materials Engineering* 9.3 (1987), pp. 293–302.

[74] IK Garkushin et al. "Salt heat storage composition". US 1036734. 1983.

[75] IK Garkushin et al. "Heat storage composition". USSR 2272823. 2006.

[76] Abdulla Magomedovich Gasanaliev and Bariyat Yunusovna Gamataeva. "Heat-accumulating properties of melts". In: *Russian Chemical Reviews* 69.2 (2000), pp. 179–186.

[77] HV Venkatesetty and RT LeFrois. "Thermal energy storage for solar power plants". In: *11th Intersociety Energy Conversion Engineering Conference*. Vol. 1. 1976, pp. 606–612.

[78] Randy J Petri, Estela T Ong, and J Martin. *High temperature composite thermal energy storage (TES) systems for industrial applications*. Tech. rep. Institute of Gas Technology, Chicago, IL (USA); Oak Ridge National Lab., TN (USA), 1986.

[79] MM Kenisarin. "Short-term storage of solar energy. 1. Low temperature phase-change materials". In: *Geliotekhnika* 29.2 (1993), pp. 46–64.

[80] Belen Zalba et al. "Review on thermal energy storage with phase change: materials, heat transfer analysis and applications". In: *Applied thermal engineering* 23.3 (2003), pp. 251–283.

[81] A Abhat, S Aboul-Enein, and NA Malatidis. "Heat-of-fusion storage systems for solar heating applications". In: *Thermal Storage of Solar Energy*. Springer, 1981, pp. 157–171.

[82] Vineet Veer Tyagi and D Buddhi. “PCM thermal storage in buildings: a state of art”. In: *Renewable and Sustainable Energy Reviews* 11.6 (2007), pp. 1146–1166.

[83] J Van Berkel. “Storage of solar energy in chemical reactions”. In: *Thermal energy storage for solar and low energy buildings", IEA Solar heating and cooling Task* 32 (2005).

[84] Mary Jane Hale et al. “Survey of thermal storage for parabolic trough power plants”. In: *NREL Report, No. NREL/SR-550-27925* (2000), pp. 1–28.

[85] Jaume Cot-Gores, Albert Castell, and Luisa F Cabeza. “Thermochemical energy storage and conversion: A-state-of-the-art review of the experimental research under practical conditions”. In: *Renewable and Sustainable Energy Reviews* 16.7 (2012), pp. 5207–5224.

[86] Devrim Aydin, Sean P Casey, and Saffa Riffat. “The latest advancements on thermochemical heat storage systems”. In: *Renewable and Sustainable Energy Reviews* 41 (2015), pp. 356–367.

[87] Frédéric Kuznik and Kevyn Johannes. “A review on chemisorption heat storage in low-energy buildings”. In: *Energy Procedia* 57 (2014), pp. 2333–2341.

[88] P Pardo et al. “A review on high temperature thermochemical heat energy storage”. In: *Renewable and Sustainable Energy Reviews* 32 (2014), pp. 591–610.

[89] Ali H Abedin and Marc A Rosen. “A critical review of thermochemical energy storage systems”. In: *The Open Renewable Energy Journal* 4.1 (2011).

[90] Chris Bales et al. “Final report of Subtask B "Chemical and Sorption Storage", The overview”. In: *Report of IEA Solar Heating and Cooling Programme–Task* 32 (2008).

[91] V Goetz, B Spinner, and E Lepinasse. “A solid-gas thermochemical cooling system using BaCl 2 and NiCl 2”. In: *Energy* 22.1 (1997), pp. 49–58.

[92] Tingxian Li et al. "A combined double-way chemisorption refrigeration cycle based on adsorption and resorption processes". In: *international journal of refrigeration* 32.1 (2009), pp. 47–57.

[93] Tingxian Li et al. "Thermodynamic study of a combined double-way solid–gas thermochemical sorption refrigeration cycle". In: *International journal of refrigeration* 32.7 (2009), pp. 1570–1578.

[94] Tingxian Li et al. "Performance improvement of a combined double-way thermochemical sorption refrigeration cycle with reheating process". In: *AIChE journal* 56.2 (2010), pp. 477–484.

[95] Wim G Haije et al. "Solid/vapour sorption heat transformer: Design and performance". In: *Applied Thermal Engineering* 27.8 (2007), pp. 1371–1376.

[96] VM Van Essen et al. "Characterization of salt hydrates for compact seasonal thermochemical storage". In: *ASME 2009 3rd International Conference on Energy Sustainability collocated with the Heat Transfer and InterPACK09 Conferences*. American Society of Mechanical Engineers. 2009, pp. 825–830.

[97] VM Van Essen et al. "Characterization of MgSO4 hydrate for thermochemical seasonal heat storage". In: *Journal of solar energy engineering* 131.4 (2009), p. 041014.

[98] R de Boer et al. "Solid-sorption cooling with integrated thermal storage-the SWEAT prototype". In: *Proceedings of the 3rd International Heat Powered Cycles Conference (HPC 2004), Larnaca, Cyprus*. 2004.

[99] H Lahmidi, S Mauran, and V Goetz. "Definition, test and simulation of a thermochemical storage process adapted to solar thermal systems". In: *Solar Energy* 80.7 (2006), pp. 883–893.

[100] Yukitaka Kato. "Chemical energy conversion technologies for efficient energy use". In: *Thermal energy storage for sustainable energy consumption*. Springer, 2007, pp. 377–391.

[101] A Hauer. "Thermal energy storage with zeolite for heating and cooling applications". In: *Proceedings of 3rd Workshop of Annex.* Vol. 17. 2002, pp. 1–2.

[102] S-G Lee, Y-K Kim, and J-Y Lee. "Operating characteristics of metal hydride heat pump using Zr-based laves phases". In: *International journal of hydrogen energy* 20.1 (1995), pp. 77–85.

[103] E Willers, M Wanner, and M Groll. "A multi-hydride thermal wave device for simultaneous heating and cooling". In: *Journal of alloys and compounds* 293 (1999), pp. 915–918.

[104] Yukitaka Kato et al. "Kinetic study of the hydration of magnesium oxide for a chemical heat pump". In: *Applied Thermal Engineering* 16.11 (1996), pp. 853–862.

[105] Yukitaka Kato et al. "Study on medium-temperature chemical heat storage using mixed hydroxides". In: *international journal of refrigeration* 32.4 (2009), pp. 661–666.

[106] Junichi Ryu et al. "Effect of transition metal mixing on reactivities of magnesium oxide for chemical heat pump". In: *Journal of Chemical Engineering of Japan* 40.13 (2007), pp. 1281–1286.

[107] PE Halstead and AE Moore. "769. The thermal dissociation of calcium hydroxide". In: *Journal of the Chemical Society (Resumed)* (1957), pp. 3873–3875.

[108] S Fujimoto, E Bilgen, and H Ogura. "$CaO/Ca(OH)_2$ chemical heat pump system". In: *Energy conversion and management* 43.7 (2002), pp. 947–960.

[109] Hironao Ogura, Tetsuya Yamamoto, and Hiroyuki Kage. "Efficiencies of $CaO/H_2O/Ca(OH)_2$ chemical heat pump for heat storing and heating/cooling". In: *Energy* 28.14 (2003), pp. 1479–1493.

[110] Yolanda A Criado, Monica Alonso, and J Carlos Abanades. "Kinetics of the $CaO/Ca(OH)_2$ hydration/dehydration reaction for thermochemical energy storage applications". In: *Industrial & Engineering Chemistry Research* 53.32 (2014), pp. 12594–12601.

[111] Ronald Barker. "The reversibility of the reaction $CaCO_3 \leftrightarrow CaO + CO_2$". In: *Journal of applied Chemistry and biotechnology* 23.10 (1973), pp. 733–742.

[112] Y Kato et al. "Utilization of high temperature heat from nuclear reactor using inorganic chemical heat pump". In: *Progress in Nuclear Energy* 32.3 (1998), pp. 563–570.

[113] MA Fahim and JD Ford. "Energy storage using the BaO_2/ BaO reaction cycle". In: *The Chemical Engineering Journal* 27.1 (1983), pp. 21–28.

[114] RG Bowrey and J Jutsen. "Energy storage using the reversible oxidation of barium oxide". In: *Solar Energy* 21.6 (1978), pp. 523–525.

[115] SUS Chol. "Enhancing thermal conductivity of fluids with nanoparticles". In: *ASME-Publications-Fed* 231 (1995), pp. 99–106.

[116] Yimin Xuan and Qiang Li. "Heat transfer enhancement of nanofluids". In: *International Journal of heat and fluid flow* 21.1 (2000), pp. 58–64.

[117] Jeffrey A Eastman et al. "Anomalously increased effective thermal conductivities of ethylene glycol-based nanofluids containing copper nanoparticles". In: *Applied physics letters* 78.6 (2001), pp. 718–720.

[118] RL Hamilton and OK Crosser. "Thermal conductivity of heterogeneous two-component systems". In: *Industrial & Engineering chemistry fundamentals* 1.3 (1962), pp. 187–191.

[119] Tae-Keun Hong, Ho-Soon Yang, and CJ Choi. "Study of the enhanced thermal conductivity of Fe nanofluids". In: *Journal of Applied Physics* 97.6 (2005), p. 064311.

[120] KS Hong, Tae-Keun Hong, and Ho-Soon Yang. "Thermal conductivity of Fe nanofluids depending on the cluster size of nanoparticles". In: *Applied Physics Letters* 88.3 (2006), p. 031901.

[121] Hrishikesh E Patel et al. "Thermal conductivities of naked and monolayer protected metal nanoparticle based nanofluids: Manifestation of anomalous enhancement and chemical effects". In: *Applied Physics Letters* 83.14 (2003), pp. 2931–2933.

[122] JA Eastman et al. "Enhanced thermal conductivity through the development of nanofluids". In: *MRS proceedings*. Vol. 457. Cambridge Univ Press. 1996, p. 3.

[123] S Lee et al. "Measuring thermal conductivity of fluids containing oxide nanoparticles". In: *Journal of Heat transfer* 121.2 (1999), pp. 280–289.

[124] Hua-qing Xie et al. "Thermal conductivity of suspensions containing nanosized SiC particles". In: *International Journal of Thermophysics* 23.2 (2002), pp. 571–580.

[125] Sarit Kumar Das et al. "Temperature dependence of thermal conductivity enhancement for nanofluids". In: *Journal of heat transfer* 125.4 (2003), pp. 567–574.

[126] YL Ding, DS Wen, and RA Williams. "Nanofluids for heat transfer intensification, where are we and we should we go". In: *Proceeding of the 6th International Heat Transfer Symposium, Beijing, China*. 2004.

[127] SMS Murshed, KC Leong, and C Yang. "Enhanced thermal conductivity of TiO_2-water based nanofluids". In: *International Journal of Thermal Sciences* 44.4 (2005), pp. 367–373.

[128] W Yu and SUS Choi. "The role of interfacial layers in the enhanced thermal conductivity of nanofluids: a renovated Maxwell model". In: *Journal of Nanoparticle Research* 5.1-2 (2003), pp. 167–171.

[129] JC Maxwell. *Electricity and Magnetism Clarendon Press*. 1873.

[130] Qing-Zhong Xue. "Model for effective thermal conductivity of nanofluids". In: *Physics letters A* 307.5 (2003), pp. 313–317.

[131] David J Jeffrey. "Conduction through a random suspension of spheres". In: *Proceedings of the Royal Society of London A: Mathematical, Physical and Engineering Sciences*. Vol. 335. 1602. The Royal Society. 1973, pp. 355–367.

[132] RH Davis. "The effective thermal conductivity of a composite material with spherical inclusions". In: *International Journal of Thermophysics* 7.3 (1986), pp. 609–620.

[133] Shih-Yuan Lu and Hway-Chi Lin. "Effective conductivity of composites containing aligned spheroidal inclusions of finite conductivity". In: *Journal of Applied Physics* 79.9 (1996), pp. 6761–6769.

[134] RT Bonnecaze and JF Brady. "The effective conductivity of random suspensions of spherical particles". In: *Proceedings of the Royal Society of London A: Mathematical, Physical and Engineering Sciences*. Vol. 432. 1886. The Royal Society. 1991, pp. 445–465.

[135] W Yu and SUS Choi. "The role of interfacial layers in the enhanced thermal conductivity of nanofluids: a renovated Hamilton–Crosser model". In: *Journal of Nanoparticle Research* 6.4 (2004), pp. 355–361.

[136] Seok Pil Jang and Stephen US Choi. "Role of Brownian motion in the enhanced thermal conductivity of nanofluids". In: *Applied physics letters* 84.21 (2004), pp. 4316–4318.

[137] C Kittel. *Thermal Physics, 1969.*

[138] PL Kapitza. "The study of heat transfer in helium II". In: *J. Phys.(USSR)* 4.1-6 (1941), pp. 181–210.

[139] Amit Gupta and Ranganathan Kumar. "Role of Brownian motion on the thermal conductivity enhancement of nanofluids". In: *Applied Physics Letters* 91.22 (2007), p. 223102.

[140] Pawel Keblinski, Ravi Prasher, and Jacob Eapen. "Thermal conductance of nanofluids: is the controversy over?" In: *Journal of Nanoparticle research* 10.7 (2008), pp. 1089–1097.

[141] Phillbot Keblinski et al. "Mechanisms of heat flow in suspensions of nano-sized particles (nanofluids)". In: *International journal of heat and mass transfer* 45.4 (2002), pp. 855–863.

[142] Ravi Prasher, Prajesh Bhattacharya, and Patrick E Phelan. "Thermal conductivity of nanoscale colloidal solutions (nanofluids)". In: *Physical review letters* 94.2 (2005), p. 025901.

[143] Xiang-Qi Wang and Arun S Mujumdar. "Heat transfer characteristics of nanofluids: a review". In: *International journal of thermal sciences* 46.1 (2007), pp. 1–19.

[144] Jacopo Buongiorno et al. "A benchmark study on the thermal conductivity of nanofluids". In: *Journal of Applied Physics* 106.9 (2009), p. 094312.

[145] James Clerk Maxwell. *A treatise on electricity and magnetism*. Vol. 1. Clarendon press, 1881.

[146] Adi T Utomo et al. "Experimental and theoretical studies of thermal conductivity, viscosity and heat transfer coefficient of titania and alumina nanofluids". In: *International Journal of Heat and Mass Transfer* 55.25-26 (2012), pp. 7772–7781.

[147] Lan Wang et al. "Enhancement of molar heat capacity of nanostructured Al2O3". In: *Journal of Nanoparticle Research* 3.5-6 (2001), pp. 483–487.

[148] Bu-Xuan Wang, Le-Ping Zhou, and Xiao-Feng Peng. "Surface and size effects on the specific heat capacity of nanoparticles". In: *International Journal of Thermophysics* 27.1 (2006), pp. 139–151.

[149] Ravikanth S Vajjha and Debendra K Das. "Specific heat measurement of three nanofluids and development of new correlations". In: *Journal of heat transfer* 131.7 (2009), p. 071601.

[150] Benigno Barbés et al. "Thermal conductivity and specific heat capacity measurements of Al_2O_3 nanofluids". In: *Journal of thermal analysis and calorimetry* 111.2 (2013), pp. 1615–1625.

[151] Harry O'Hanley et al. "Measurement and model validation of nanofluid specific heat capacity with differential scanning calorimetry". In: *Advances in Mechanical Engineering* 4 (2012), p. 181079.

[152] Hani Tiznobaik and Donghyun Shin. "Enhanced specific heat capacity of high-temperature molten salt-based nanofluids". In: *International Journal of Heat and Mass Transfer* 57.2 (2013), pp. 542–548.

[153] Manila Chieruzzi et al. "Effect of nanoparticles on heat capacity of nanofluids based on molten salts as PCM for thermal energy storage". In: *Nanoscale research letters* 8.1 (2013), pp. 1–9.

[154] Bharath Dudda and Donghyun Shin. "Effect of nanoparticle dispersion on specific heat capacity of a binary nitrate salt eutectic for concentrated solar power applications". In: *International Journal of Thermal Sciences* 69 (2013), pp. 37–42.

[155] L Xue et al. "Effect of liquid layering at the liquid–solid interface on thermal transport". In: *International Journal of Heat and Mass Transfer* 47.19 (2004), pp. 4277–4284.

[156] Ling Li et al. "Molecular dynamics simulation of effect of liquid layering around the nanoparticle on the enhanced thermal conductivity of nanofluids". In: *Journal of nanoparticle research* 12.3 (2010), pp. 811–821.

[157] SH Oh et al. "Ordered liquid aluminum at the interface with sapphire". In: *Science* 310.5748 (2005), pp. 661–663.

[158] Ming-Chang Lu and Chien-Hsun Huang. "Specific heat capacity of molten salt-based alumina nanofluid". In: *Nanoscale research letters* 8.1 (2013), pp. 1–7.

[159] Patricia Andreu-Cabedo et al. "Increment of specific heat capacity of solar salt with SiO2 nanoparticles". In: *Nanoscale research letters* 9.1 (2014), pp. 1–11.

[160] Byeongnam Jo and Debjyoti Banerjee. "Enhanced specific heat capacity of molten salt-based nanomaterials: Effects of nanoparticle dispersion and solvent material". In: *Acta Materialia* 75 (2014), pp. 80–91.

[161] Ming Xi Ho and Chin Pan. "Optimal concentration of alumina nanoparticles in molten Hitec salt to maximize its specific heat capacity". In: *International Journal of Heat and Mass Transfer* 70 (2014), pp. 174–184.

[162] Donghyun Shin and Debjyoti Banerjee. "Enhanced specific heat capacity of nanomaterials synthesized by dispersing silica nanoparticles in eutectic mixtures". In: *Journal of Heat Transfer* 135.3 (2013), p. 032801.

[163] Ravi Prasher, Prajesh Bhattacharya, and Patrick E Phelan. "Brownian-motion-based convective-conductive model for the effective thermal conductivity of nanofluids". In: *Journal of heat transfer* 128.6 (2006), pp. 588–595.

[164] D Poulikakos and Shigeo Maruyama. "Molecular dynamics simulation in nanoscale heat transfer: A review". In: *Microscale Thermophysical Engineering* 7.3 (2003), pp. 181–206.

[165] Eric Pop, Vikas Varshney, and Ajit K Roy. "Thermal properties of graphene: Fundamentals and applications". In: *MRS bulletin* 37.12 (2012), pp. 1273–1281.

[166] Jin-Wu Jiang, Harold S Park, and Timon Rabczuk. "Molecular dynamics simulations of single-layer molybdenum disulphide (MoS2): Stillinger-Weber parametrization, mechanical properties, and thermal conductivity". In: *Journal of Applied Physics* 114.6 (2013), p. 064307.

[167] Xiangfan Xu et al. "Length-dependent thermal conductivity in suspended single-layer graphene". In: *Nature communications* 5 (2014).

[168] Shanshan Chen et al. "Thermal conductivity of isotopically modified graphene". In: *Nature materials* 11.3 (2012), pp. 203–207.

[169] F Gr Fumi and MP Tosi. "Ionic sizes and born repulsive parameters in the NaCl-type alkali halides-I: The Huggins-Mayer and Pauling forms". In: *Journal of Physics and Chemistry of Solids* 25.1 (1964), pp. 31–43.

[170] MP Tosi and FG Fumi. "Ionic sizes and born repulsive parameters in the NaCl-type alkali halides-II: The generalized Huggins-Mayer form". In: *Journal of Physics and Chemistry of Solids* 25.1 (1964), pp. 45–52.

[171] Jamshed Anwar, Daan Frenkel, and Massimo G Noro. "Calculation of the melting point of NaCl by molecular simulation". In: *The Journal of chemical physics* 118.2 (2003), pp. 728–735.

[172] David M Eike, Joan F Brennecke, and Edward J Maginn. "Toward a robust and general molecular simulation method for computing solid-liquid coexistence". In: *The Journal of chemical physics* 122.1 (2005), p. 014115.

[173] N Galamba, CA Nieto de Castro, and JF Ely. "Thermal conductivity of molten alkali halides from equilibrium molecular dynamics simulations". In: *The Journal of chemical physics* 120.18 (2004), pp. 8676–8682.

[174] N Galamba, CA Nieto de Castro, and James F Ely. "Shear viscosity of molten alkali halides from equilibrium and nonequilibrium molecular-dynamics simulations". In: *Journal of Chemical Physics* 122.22 (2005), pp. 224501–224501.

[175] Toshio Yamaguchi et al. "X-ray and neutron diffraction and molecular dynamics simulation of molten lithium and rubidium nitrates". In: *Molecular Physics* 58.2 (1986), pp. 349–364.

[176] Ashok K Adya et al. "Structural determination of molten NaNO3, NaNO2 and their eutectic mixture by molecular dynamics simulation and X-ray diffraction". In: *Molecular Physics* 62.1 (1987), pp. 227–238.

[177] Ashok K Adya and George W Neilson. "Neutron diffraction results from some nitrate melts". In: *Journal of non-crystalline solids* 205 (1996), pp. 168–171.

[178] Toshiko Katō et al. "Cation dependence of the ionic dynamics in computer simulated molten nitrates". In: *The Journal of chemical physics* 99.5 (1993), pp. 3966–3975.

[179] G Vöhringer and J Richter. "Molecular dynamics simulation of molten alkali nitrates". In: *Zeitschrift für Naturforschung A* 56.5 (2001), pp. 337–341.

[180] Mauro CC Ribeiro. "On the Chemla effect in molten alkali nitrates". In: *The Journal of chemical physics* 117.1 (2002), pp. 266–276.

[181] Sérgio M Urahata and Mauro CC Ribeiro. "Molecular dynamics simulation of molten LiNO 3 with flexible and polarizable anions". In: *Physical Chemistry Chemical Physics* 5.12 (2003), pp. 2619–2624.

[182] Saivenkataraman Jayaraman et al. "Molecular simulation of the thermal and transport properties of three alkali nitrate salts". In: *Industrial & Engineering Chemistry Research* 49.2 (2009), pp. 559–571.

[183] R Vogelsang, C Hoheisel, and G Ciccotti. "Thermal conductivity of the Lennard-Jones liquid by molecular dynamics calculations". In: *The Journal of chemical physics* 86.11 (1987), pp. 6371–6375.

[184] Suranjan Sarkar and R Panneer Selvam. "Molecular dynamics simulation of effective thermal conductivity and study of enhanced thermal transport mechanism in nanofluids". In: *Journal of applied physics* 102.7 (2007), p. 074302.

[185] Wenzheng Cui et al. "On the influencing factors and strengthening mechanism for thermal conductivity of nanofluids by molecular dynamics simulation". In: *Industrial & Engineering Chemistry Research* 50.23 (2011), pp. 13568–13575.

[186] ASTM Standard. *E1269-05, 2003. Standard Test Method for Determining Specific Heat Capacity by Differential Scanning Calorimetry. ASTM International, West Conshohocken, PA. doi: 10.1520/E1269-05.*

[187] WJ Parker et al. "Flash method of determining thermal diffusivity, heat capacity, and thermal conductivity". In: *Journal of applied physics* 32.9 (1961), pp. 1679–1684.

[188] Alena Mudroch, José M Azcue, and Paul Mudroch. *Manual of physico-chemical analysis of aquatic sediments*. CRC Press, 1996.

[189] IN McCave et al. "Evaluation of a Laser-Diffraction-Size Analyzer for Use with Natural Sediments: RESEARCH METHOD PAPER". In: *Journal of Sedimentary Research* 56.4 (1986).

[190] MA González. "Force fields and molecular dynamics simulations". In: *École thématique de la Société Française de la Neutronique* 12 (2011), pp. 169–200.

[191] Kurt Binder and Giovanni Ciccotti. *Monte Carlo and molecular dynamics of condensed matter systems*. Vol. 49. Compositori, 1996.

[192] BWH Van Beest, Gert Jan Kramer, and RA Van Santen. "Force fields for silicas and aluminophosphates based on ab initio calculations". In: *Physical Review Letters* 64.16 (1990), p. 1955.

[193] Antoine Carre et al. "New fitting scheme to obtain effective potential from Car-Parrinello molecular-dynamics simulations: Application to silica". In: *EPL (Europhysics Letters)* 82.1 (2008), p. 17001.

[194] Kasper P Jensen and William L Jorgensen. "Halide, ammonium, and alkali metal ion parameters for modeling aqueous solutions". In: *Journal of Chemical Theory and Computation* 2.6 (2006), pp. 1499–1509.

[195] Keith E Gutowski, Burcu Gurkan, and Edward J Maginn. "Force field for the atomistic simulation of the properties of hydrazine, organic hydrazine derivatives, and energetic hydrazinium ionic liquids". In: *Pure and Applied Chemistry* 81.10 (2009), pp. 1799–1828.

[196] HA Lorentz. "Ueber die Anwendung des Satzes vom Virial in der kinetischen Theorie der Gase". In: *Annalen der Physik* 248.1 (1881), pp. 127–136.

[197] Daniel Berthelot. "Sur le mélange des gaz". In: *Compt. Rendus* 126 (1898), pp. 1703–1706.

[198] M Born and A Lande. "Über die Berchnung der Kompressibilität regulärer Kristalle aus der Gittertheorie". In: *Selected Scientific Papers of Alfred Landé*. Springer, 1988, pp. 58–64.

[199] Joseph E Mayer. "Dispersion and polarizability and the van der waals potential in the alkali halides". In: *The Journal of Chemical Physics* 1.4 (1933), pp. 270–279.

[200] Maurice L Huggins and Joseph E Mayer. "Interatomic distances in crystals of the alkali halides". In: *The Journal of Chemical Physics* 1.9 (1933), pp. 643–646.

[201] HJC Berendsen. "J, PM Postma, WF van Gunsteren and J, Hermans". In: *B. pullman (Ed.), Intermolecular Forces, Reidel, Dordrecht* 331 (1981).

[202] Mike P Allen and Dominic J Tildesley. *Computer simulation of liquids*. Oxford university press, 1989.

[203] An Truong Pham, Murat Barisik, and Bohung Kim. "Molecular dynamics simulations of Kapitza length for argon-silicon and water-silicon interfaces". In: *International journal of precision engineering and manufacturing* 15.2 (2014), pp. 323–329.

[204] Murat Barisik and Ali Beskok. "Wetting characterisation of silicon (1, 0, 0) surface". In: *Molecular Simulation* 39.9 (2013), pp. 700–709.

[205] Roger W Hockney and James W Eastwood. *Computer simulation using particles*. CRC Press, 1988.

[206] William C Swope et al. "A computer simulation method for the calculation of equilibrium constants for the formation of physical clusters of molecules: Application to small water clusters". In: *The Journal of Chemical Physics* 76.1 (1982), pp. 637–649.

[207] David Chandler. "Introduction to modern statistical mechanics". In: *Introduction to Modern Statistical Mechanics, by David Chandler, pp. 288. Foreword by David Chandler. Oxford University Press, Sep 1987. ISBN-10: 0195042778. ISBN-13: 9780195042771* 1 (1987).

[208] Gianluca Puliti. *Properties of Au-H2O nanofluids using molecular dynamics*. 2012.

[209] Melville S Green. "Markoff Random Processes and the Statistical Mechanics of Time-Dependent Phenomena". In: *The Journal of Chemical Physics* 20.8 (1952), pp. 1281–1295.

[210] Melville S Green. "Markoff Random Processes and the Statistical Mechanics of Time-Dependent Phenomena. II. Irreversible Processes in Fluids". In: *The Journal of Chemical Physics* 22.3 (1954), pp. 398–413.

[211] Ryogo Kubo. "Statistical-mechanical theory of irreversible processes. I. General theory and simple applications to magnetic and conduction problems". In: *Journal of the Physical Society of Japan* 12.6 (1957), pp. 570–586.

[212] AW Lees and SF Edwards. "The computer study of transport processes under extreme conditions". In: *Journal of Physics C: Solid State Physics* 5.15 (1972), p. 1921.

[213] Eveline M Gosling, IR McDonald, and K Singer. "On the calculation by molecular dynamics of the shear viscosity of a simple fluid". In: *Molecular Physics* 26.6 (1973), pp. 1475–1484.

[214] WT Ashurst and WG Hoover. "Argon shear viscosity via a Lennard-Jones potential with equilibrium and nonequilibrium molecular dynamics". In: *Physical Review Letters* 31.4 (1973), p. 206.

[215] Florian Müller-Plathe. "Reversing the perturbation in nonequilibrium molecular dynamics: An easy way to calculate the shear viscosity of fluids". In: *Physical Review E* 59.5 (1999), p. 4894.

[216] Robert W Carling. "Heat capacities of NaNO 3 and KNO 3 from 350 to 800 K". In: *Thermochimica Acta* 60.3 (1983), pp. 265–275.

[217] RC Wheast and MJ Astle. *CRC Handbook of Chemistry and Physics*. 1982.

[218] Z Hongmin et al. "ULTRASONIC VELOCITY AND ABSORPTION-COEFFICIENT IN MOLTEN ALKALI-METAL NITRATES AND CARBONATES". In: *JOURNAL OF THE JAPAN INSTITUTE OF METALS* 55.9 (1991), pp. 937–944.

[219] Frank Rioux. "Colligative properties". In: *J. Chem. Educ* 50.7 (1973), p. 490.

[220] Peter W Atkins and Julio De Paula. "Atkins' physical chemistry". In: (2010).

[221] George H Duffey. "Equilibria in Condensed Phases". In: *Modern Physical Chemistry*. Springer, 2000, pp. 171–205.

[222] Huaqing Xie, Jifen Wan, and Lifei Chen. "Effects on the phase transformation temperature of nanofluids by the nanoparticles". In: *Journal of materials science & technology* 24.5 (2008), p. 742.

[223] Yuji Nagasaka and A Nagashima. "The thermal conductivity of molten NaNO3 and KNO3". In: *International Journal of Thermophysics* 12.5 (1991), pp. 769–781.

[224] T Omotani and A Nagashima. "Thermal conductivity of molten salts, HTS and the lithium nitrate-sodium nitrate system, using a modified transient hot-wire method". In: *Journal of Chemical and Engineering Data* 29.1 (1984), pp. 1–3.

[225] R Tufeu et al. "Experimental determination of the thermal conductivity of molten pure salts and salt mixtures". In: *International journal of thermophysics* 6.4 (1985), pp. 315–330.

[226] David G Cahill and Robert O Pohl. "Thermal conductivity of amorphous solids above the plateau". In: *Physical review B* 35.8 (1987), p. 4067.

[227] Y Thomas He, Jiamin Wan, and Tetsu Tokunaga. "Kinetic stability of hematite nanoparticles: the effect of particle sizes". In: *Journal of nanoparticle research* 10.2 (2008), pp. 321–332.

[228] Gerhard Hummer, Jayendran C Rasaiah, and Jerzy P Noworyta. "Water conduction through the hydrophobic channel of a carbon nanotube". In: *Nature* 414.6860 (2001), pp. 188–190.

APPENDIX A

SPECIFIC HEAT CAPACITY OF SYNTHETIC SAPPHIRE

Table A.1: Sapphire specific heat capacity literature values

Temperature °C	Temperature K	Specific heat capacity J g^{-1} K^{-1}	Temperature °C	Temperature K	Specific heat capacity J g^{-1} K^{-1}
-183.15	90	0.0949	126.85	400	0.9423
-173.15	100	0.1261	136.85	410	0.9545
-163.15	110	0.1603	146.85	420	0.966
-153.15	120	0.1968	156.85	430	0.977
-143.15	130	0.2349	166.85	440	0.9875
-133.15	140	0.2739	176.85	450	0.9975
-123.15	150	0.3134	186.85	460	1.007
-113.15	170	0.3526	196.85	470	1.0161
-103.15	170	0.3913	206.85	480	1.0247
-93.15	180	0.4291	216.85	490	1.033
-83.15	190	0.4659	226.85	500	1.0409
-73.15	200	0.5014	236.85	510	1.0484
-63.15	210	0.5356	246.85	520	1.0557
-53.15	220	0.5684	256.85	530	1.0627
-43.15	230	0.5996	266.85	540	1.0692
-33.15	240	0.6294	276.85	550	1.0756
-23.15	250	0.6579	286.85	560	1.0817
-13.15	260	0.6848	296.85	570	1.0876
-3.15	270	0.7103	306.85	580	1.0932
0	273.15	0.718	316.85	590	1.0987
6.85	280	0.7343	326.85	600	1.1038
16.85	290	0.7572	336.85	610	1.1089
26.85	300	0.7788	346.85	620	1.1137
36.85	310	0.7994	356.85	630	1.1183
46.85	320	0.8188	366.85	640	1.1228
56.85	330	0.8373	376.85	650	1.1271
66.85	340	0.8548	386.85	660	1.1313
76.85	350	0.8713	396.85	670	1.1353
86.85	360	0.8871	406.85	680	1.1393
96.85	370	0.902	416.85	690	1.1431
106.85	380	0.9161	426.85	700	1.1467
116.85	390	0.9296	446.85	720	1.1538
466.85	740	1.1604	806.85	1080	1.2383
486.85	760	1.1667	826.85	1100	1.2417
506.85	780	1.1726	846.85	1120	1.2451
526.85	800	1.1783	866.85	1140	1.2484
546.85	820	1.1837	886.85	1160	1.2516
566.85	840	1.1888	906.85	1180	1.2548
586.85	860	1.1937	926.85	1200	1.2578
606.85	880	1.1985	976.85	1250	1.2653
626.85	900	1.203	1026.85	1300	1.2724
646.85	920	1.2074	1076.85	1350	1.2792
666.85	940	1.2117	1126.85	1400	1.2856
686.85	960	1.2159	1176.85	1450	1.2917
706.85	980	1.2198	1226.85	1500	1.2975
726.85	1000	1.2237	1276.85	1550	1.3028
746.85	1020	1.2275	1326.85	1600	1.3079
766.85	1040	1.2312	1376.85	1650	1.3128
786.85	1060	1.2348			